INVESTIGATING THE CHEMICAL PROPERTIES OF GRAPHENE USING ELECTROCHEMICAL METHODS

A Dissertation

Presented to the Faculty of the Graduate School

of Cornell University

In Partial Fulfillment of the Requirements for the Degree of

Doctor of Philosophy

by

Cen Tan

August 2013

INVESTIGATING THE CHEMICAL PROPERTIES OF GRAPHENE USING ELECTROCHEMICAL METHODS

Cen Tan, Ph.D.

Cornell University 2013

Graphene, a single layer of carbon atoms, has been in the center stage of materials research since its discovery in 2004. Its chemical properties are yet to be understood. In this dissertation, I will discuss the investigation of graphene's chemical properties using various electrochemical techniques. First, we found that the heterogeneous electron transfer rate of ferrocene at graphene is one order of magnitude higher than that of highly oriented pyrolytic graphite. The enhanced electrochemical reactivity is ascribed to the presence of corrugations and imperfections that disrupt the sp^2 conjugation of graphene which can alter its electrical, chemical, and mechanical properties. We have further examined the rate of heterogeneous electron transfer of various redox mediators at graphene using scanning electrochemical microscopy (SECM). SECM offers a versatile set of tools to characterize the reactivity of surfaces with temporal and spatial resolution. It was found that the sites with a large concentration of defects are approximately one order of magnitude more reactive compared to more pristine graphene surfaces. Furthermore, the reactivity of graphene defects can be selectively passivated by carefully controlling the electropolymerization conditions of *o*-phenylenediamine. The use of spatially resolved scanning electrochemical microscopy for detecting the presence and the "healing" of defects on graphene provides a strategy for *in situ* characterization and control of this attractive surface, enabling optimization of its properties for application in electronics, sensing, and electrocatalysis.

BIOGRAPHICAL SKETCH

Cen Tan was born in Tianjin, China. She moved to the San Francisco Bay Area with her family in 1998 during the boom of the high tech industry where her father worked as an electrical engineer. She attended Walters Junior High School and Mission San Jose High School in Fremont, California. Cen pursued chemistry and economics at the University of California, Berkeley. She worked for Professor Ting Xu in the Department of Materials Science and Engineering and had the opportunity to conduct research at the Molecular Foundry of the Lawrence Berkeley National Laboratory. She was exposed to the frontier of materials research and state of the art instruments. While at UC Berkeley, she was inspired by many amazing scientists. In 2008, Cen decided to continue her education at Cornell University to study the chemical properties of graphene in the laboratory of Professor Héctor D. Abruña.

To my parents and grandparents

ACKNOWLEDGMENTS

I am thankful for all the inspiration, guidance, encouragement and understanding of my professors, mentors, colleagues, family and friends.

I would like to thank Professor Héctor D. Abruña for giving me the opportunity to work in his lab as well as the guidance and encouragement during my graduate studies. Thanks for letting me explore my interests in molecular electronics and nano-fabrication which led to my first job as a process engineer. I would like to thank Professors Daniel C. Ralph and Paul L. McEuen for serving on my thesis committee and their valuable suggestions. I appreciate Professor Melissa Hines' advices on public speaking. I became a much better presenter after the IGERT training. I am also grateful for the guidance of my undergraduate research adviser, Professor Ting Xu. I also appreciate the inspiration and encouragement of my 7^{th} and 8^{th} grade math teacher, Mr. Leon.

I thank Sean Conte, Jimmy John, Minh Nguyen, Wan Li, Jessica Shu, Tammy Chu and Hoang Le for their friendship. I could not have survived Ithaca without you. I am also thankful for the guidance of Dr. Joaquin Rodriguez-Lopez, Dr. David Finkelstein, Dr. Eric Rus, Dr. Yu-Wu Zhong, Dr. Joshua Parks and Dr. Michael Lowe. I thank all past and present members of the Abruña Lab. I am grateful for the generous assistance of Dr. Sufei Shi, Joshua Kevek, Samantha Roberts, Pinshane Huang, Dr. Zhenghui Wang, Dr. Fernando Uribe-Romo and Dr. Jimmy O'Dea.

Most importantly, I would like to thank my parents for their endless love, encouragement and understanding.

TABLE OF CONTENTS

LIST OF FIGURES

LIST OF TABLES

Chapter 1

Introduction to Graphene

1.1 Introduction to Graphene

Atomically thin, two-dimensional materials have been of immense interest since the mid-twentieth century.[1,2] Many scientists have attempted to mechanically exfoliate layered materials such as highly oriented pyrolytic graphite.[3] Single-layer graphite crystals and their electronic properties were first reported by Geim and co-workers in 2004. The term graphene is generally used to describe graphite sheets in the honeycomb arrangement that are less than 10 layers thick. Graphene exhibits many unique properties. It is a zero band gap semi-metal, it has remarkable charge carrier mobility, it is 98% transparent, and it has extraordinary mechanical strength and thermal conductivity.[4–9] This material has stimulated an enormous amount of research across many scientific disciplines from physics to biology to engineering. There is increased interest in understanding the chemistry of graphene, controlling its properties through chemical modifications, and using it in applications such as energy storage, sensors, catalysis, and electronics, just to name a few. Despite this excitement, many challenges remain in using graphene for practical technologies. For instance, while mechanically exfoliated graphene possesses superb electronic properties, its usefulness in applications is limited because generally only small samples (flakes that are typically tens of microns wide) can be made. Chemical-vapor deposited (CVD) graphene is more suitable for large-scale processing of graphene, but the fabrication

process generally introduces grain boundaries, impurities, and physical damage. These defects can strongly influence the electrical, chemical, and mechanical characteristics of graphene. In order to take full advantage of the properties of graphene in applications, it is necessary understand its chemical properties.

1.2 Graphene Fabrication

The research on the properties and applications of graphene has led the development of various methods for producing graphene. Graphene prepared using mechanical exfoliation remains to be the highest quality for scientific research. Alternative methods such as chemical vapor deposition, organic total synthesis and chemical oxidation and reduction have been developed. The area of graphene samples has increased by approximately 2 trillion times in less than a decade.

In the late 1990's, graphite crystals of a few layers had been achieved by mechanical exfoliation using modified AFM cantilevers.[3,10] The repetitive up and down motion of the cantilever removes layers of graphite from a highly oriented pyrolytic graphite (HOPG) stack. A few years later, Geim and co-workers, at Manchester University, reported the first single-layer graphite nano-crystal and its electrical properties.[11] The exfoliation method simply involves Kish graphite and Scotch tape. Graphite covered Scotch tape is pressed onto a 300 nm SiO_2/Si wafer. The graphite crystals are fixed to the substrate by Van der Waals forces.[4,12–14] One to two pieces of single-layer graphene can be found on a 2×2 cm^2 wafer. The size of these graphene crystals was approximately 100 μm^2. The charge carrier mobility was

reported to be 200,000 $cm^2V^{-1}s^{-1}$.[4,5] Although mechanically exfoliated graphene demonstrate extraordinary physical and electrical properties, the small size limits its practical applications. The development of an alternative graphene preparation method was clearly necessary.

Chemical vapor deposition (CVD) is the most promising approach to prepare large-area graphene samples.[9,15] The method was developed soon after the first report on single-layer graphene. This method is widely employed because the size of the graphene sample is determined by the size of the substrate. The quality of graphene is related to the cleanliness of the substrate. The frequently used copper (Cu) substrates are cleaned with acetone to remove organic residuals and with acetic acid to remove oxides. Hydrogen (H_2) gas is used to further remove the oxide by reduction. Finally, methane (CH_4) gas is flowed over the Cu substrate at 1000 ℃ (Figure 1.2.1). CVD growth conditions significantly affect the characteristics of the graphene samples. For example, a conventional growth using 36 sccm of CH_4 rates for 20 minutes yields grain sizes in the range of 0.5-2 μm while growth using 3.6 sccm of CH_4 for 3 hours yields grain sizes in the range of 0.5-50 μm. In addition, longer growth times can also give rise to more multi-layer graphene regions. A thorough understanding of the growth mechanism is essential in order to produce graphene of consistent quality. Other metals such as nickel (Ni) have been explored as potential substrates. Nevertheless, the results are inconsistent due to the higher solubility of CH_4 in Ni at high temperatures.

Due to the increased interest in using graphene for industrial applications, Samsung Group and Sony Corporation have developed roll-to-roll processing techniques to manufacture large-area CVD graphene.[16,17] A local heating method able to produce graphene up to 100 meters long was reported recently. The quality of CVD graphene has improved over time. However, it remains more defective compared to mechanically exfoliated graphene as demonstrated by Raman spectroscopy and charge carrier mobility measurements.

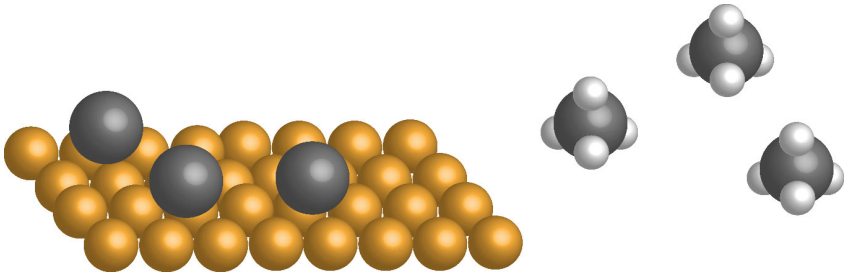

Figure 1.2.1. Chemical vapor deposited graphene. A mixture of H_2 and CH_4 gas is flowed over a Cu substrate at 1000 ℃ for 20 minutes. The method yields predominately single-layer graphene.

The total synthesis of macromolecules such as carbon nanotubes and graphene has been of interest to many organic chemists.[18–21] This method offers graphene without heteroatoms, defects or grain boundaries. Nevertheless, it is extremely difficult to achieve large-area graphene because solubility decreases as the size of the macromolecule increases. In addition, numerous side reactions will drastically reduce the yield of the synthesis. Furthermore, the total organic synthesis of graphene is particularly expensive and time consuming.

The reduction of graphene oxide is the most cost-effective method to produce graphene.[22–27] Graphene oxide can be prepared by the methods reported by Staudenmaier, Brodie, and Hummers.[28–30] The basal plane of graphene oxide is decorated with many oxygenated groups. The hydrophilic property allows graphene oxide to be well dispersed in water. While sonicating graphene oxide in water, a color change from dark yellow to clear can be observed as bulk graphene oxide delaminates to individual sheets. Graphene oxide can then be reduced to graphene using hydrazine hydrate at elevated temperatures. The reduction of graphene oxide to graphene is not efficient, therefore, many heteroatoms remain. The inferior quality is indicated by the large D band in the Raman spectrum.

Several other graphene preparation methods have been reported.[31–36] The most common methods used in the characterization and applications of graphene are mechanical exfoliation and chemical vapor deposition. Further improvements are needed to reduce the cost of scalable, large area, and high quality graphene for the material to be valuable in applications.

As of today, there is still no known method of producing graphene without defects. The performance of graphene can be severely affected by these defects as shown in the charge carrier mobility comparison between mechanically exfoliated graphene and chemical vapor deposited graphene. Research in the past has focused mostly on the applications of graphene. Nevertheless, it is very important for scientists to understand the effects of heteroatoms, structural defects, and grain boundaries on the properties of graphene.

1.3 Graphene Characterizations

Many methods are employed to characterize the properties of graphene. Optical microscopy provides an initial examination of the thickness and quality of the graphene sample. Atomic force microscopy and scanning tunneling microscopy are used to measure the thickness as well as detect defects and contamination on graphene. Raman spectroscopy provides a high throughput approach to confirm the quality and thickness of the graphene sample. Transmission electron microscopy is capable of measuring the grain size of graphene and resolving the structure of grain boundaries. Electrical, mechanical, and optical properties were characterized using various methods. They will not be discussed here but can be found in references 4-8, 15 and 37.[4–6,8,15,37]

1.3.1 Optical Microscopy

Optical microscopy provides an initial examination of the thickness and quality of a graphene sample.[37–39] Optical microscopy appears to be straight forward, but identifying an atomically thick graphene sample is no easy task since the material has an optical absorbance of 2.3%. One of the most important contributions of Geim and co-workers was recognizing that single-layer graphene is visible on 300 nm of SiO_2 on a Si substrate. The color of graphene on SiO_2/Si can provide experienced scientists information about the thickness of the graphene sample. In Figure 1.3.1, the light purple region in the middle of the image contains single- to multi-layer graphene. The

blue region on the left is graphite with tens to hundreds of layers, and the gold colored island in the center is bulk graphite.

Optical microscopy is also used to examine the quality of graphene. Large discontinuities and consistent contamination on a sample can be seen using optical microscopy. Discontinuities are occasionally found in CVD graphene due to modifications in the growth conditions. Additionally, CVD graphene is prone to contamination due to the preparation procedures. Large regions of polymer and metal particle contamination can be observed by optical microscopy.

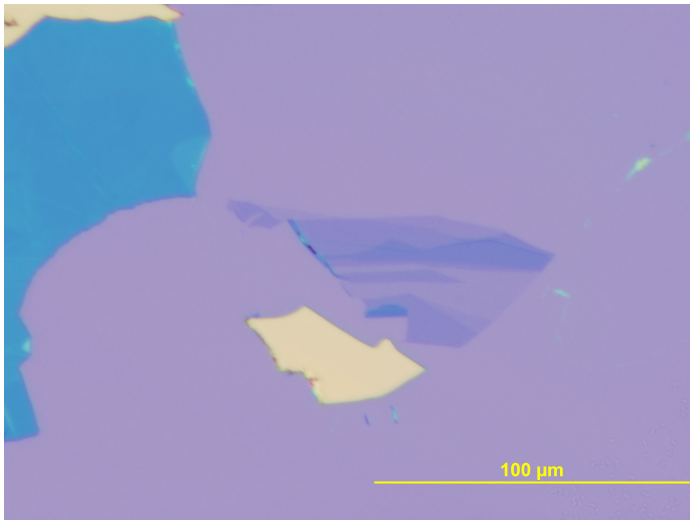

Figure 1.3.1. Optical micrograph of mechanically exfoliated graphene on a 300 nm SiO_2/Si substrate. The light purple region in the center contains single- and multi-layer graphene. The purple with the lowest contrast is single-layer graphene. The blue region on the left is graphite with hundreds of layers. The gold colored island is bulk graphite.

1.3.2 Atomic Force Microscopy and Scanning Tunneling Microscopy

The thickness of single-layer graphene can be measured using atomic force microscopy (AFM).[11,14] The step height of each successive layer was determined to be 0.34 nm. The height of graphene on a SiO_2/Si substrate has been reported to be approximately 1 nm. The difference between the measurements originates from the adsorbents on the SiO_2/Si substrate under ambient conditions. AFM is useful in identifying contaminations on graphene samples. Comparing the AFM images of a mechanically exfoliated graphene sample and a CVD graphene sample, one can clearly see that the height image of CVD graphene is rough, likely due to defects and contamination.

Scanning tunneling microscopy (STM) maps the electronic topography of surfaces with atomic resolution. The differences in the density of states between single-layer graphene and multi-layer graphene results in two dissimilar STM imags.[40–42] The density of states of all carbon atoms are equivalent in single-layer graphene (Figure 1.3.2A). Hence, a honeycomb structure is observed (Figure 1.3.2C). In multi-layer graphene or HOPG, the density of states of the carbon atoms are no longer equivalent. Half of the carbon atoms in the top layer overlap half of the carbon atoms in the next layer, thus contributing to a lower electron density to the STM tip. The other half of the carbon atoms in the top layer contribute a higher electron density to the STM tip. In multi-layer graphene, a three-for-six triangular structure is observed (Figure 1.3.2B). STM is also employed to identify interesting electronic properties of graphene defects.

Despite of the advantages, STM and AFM imaging is limited to examine small graphene samples. Additionally, the sample preparation is not trivial. Moisture and organic residues on the supporting substrate could affect the quality of the measurements under ambient conditions.

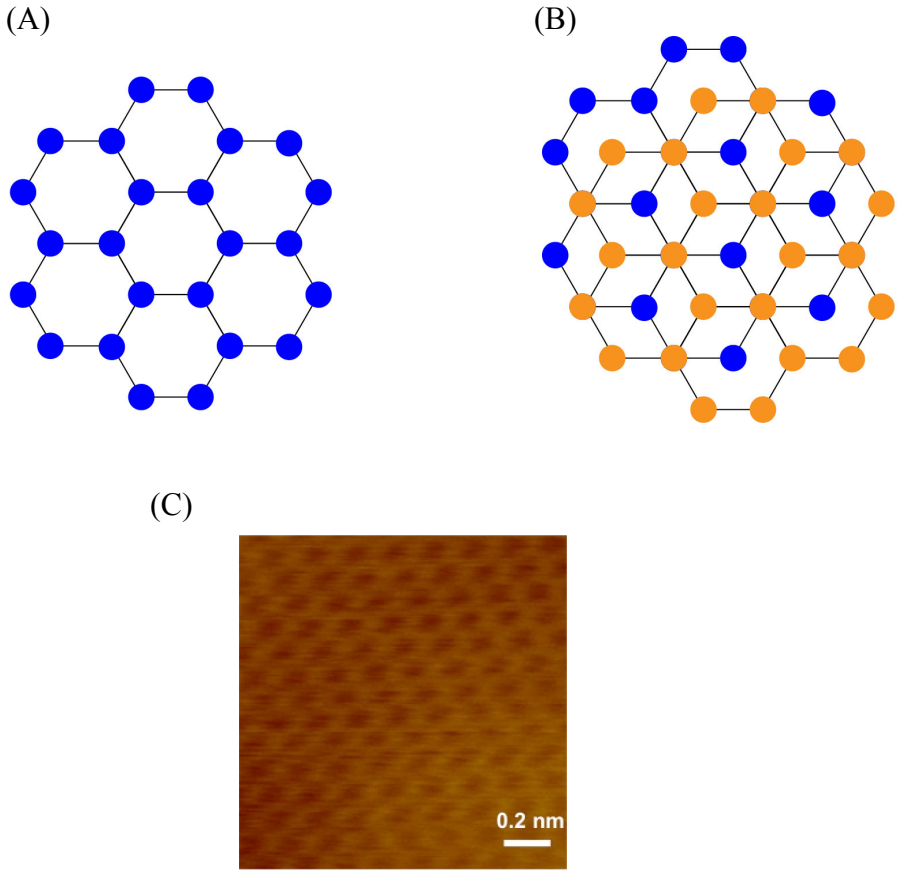

Figure 1.3.2. Scanning tunneling microscopy image of graphene. (A) Honeycomb structure is observed in single-layer graphene because the density of states of all carbon atoms is equivalent. (B) Three-for-six structure is observed in multi-layer graphene because the density of states of every other carbon atoms in the top layer is affected by the overlapping carbon atoms in the layer below. (C) STM image of a CVD graphene sample.

1.3.3 Raman Spectroscopy

Raman spectroscopy provides a high throughput approach to determine the characteristics of graphene.[43–50] Each of the three signature peaks at 1350 cm^{-1}, 1583 cm^{-1} and 2700 cm^{-1} provide important information regarding the quality and thickness of a graphene sample.

The peak at 1583 cm^{-1}, also known as the G peak, is a result of the E_{2g} vibrational mode. The G peak is common to all carbon materials, though the peak position for bulk graphite is slightly lower than single-layer graphene. The 2D peak at 2700 cm^{-1} involves second order two-phonon transitions. The position of this peak is related to the incident laser energy. Single-layer graphene has only one possible second order transition, therefore, a single sharp 2D peak at 2700 cm^{-1} is observed as depicted in Figure 1.3.3. Double-layer and triple-layer graphene have 4 and 15 second-order transitions, respectively. Hence, broad peaks comprising 4 and 15 peaks are observed around 2700 cm^{-1}. The intensity of the 2D peak decreases as the thickness of the graphene sample increases. The position of the second order two-phonon transitions for graphene of various thicknesses has been calculated using first-principles density functional theory (DFT).[51]

The D peak at 1350 cm^{-1} is an important feature that contains evidence of disorder on the graphene sample. The D peak is not Raman active for pristine graphene, but it is observed when symmetry is broken by disorder. The D peak could arise from any kind of imperfection – grain boundaries, heteroatoms, structural defects, or edges. It is important to note that not all imperfections give rise to the peak.

For example, the D peak does not exist for zigzag edges because of the direction of the momentum vector. Therefore, the intensity of the D peak cannot be used to quantify the number of defects. The position of the D peak is dependent on the incident laser energy, although the dispersion is not as significant as the 2D peak.

Raman mapping is routinely employed to examine the quality of graphene samples. The ratio between the D peak intensity and the G peak intensity can be plotted over an area of interest. The spatial map is useful in the comparison of defect concentrations of a graphene sample.[52,53] In conclusion, Raman provides a relatively high throughput method to determine the thickness and quality of graphene.

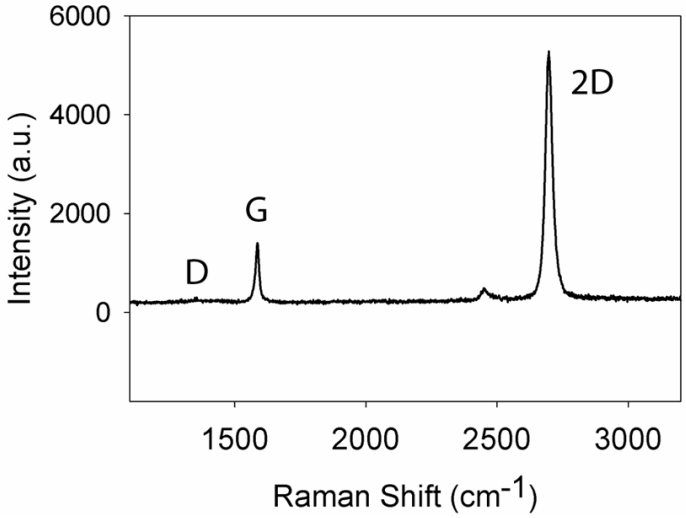

Figure 1.3.3. Raman spectrum of CVD graphene. The sharp 2D band indicates that the graphene sample is predominantly single layer and the small D band suggests that the graphene sample does not contain a significant density of defects.

1.3.4 Transmission Electron Microscopy

Transmission electron microscopy (TEM) provides essential information about graphene which no other characterization technique can attain.[12,54,55] Dark field TEM is commonly used to determine the grain size of a graphene sample. An example of a dark field TEM image of CVD graphene is presented in figure 1.3.4. The various colors correspond to the different grain orientations on the graphene sample – each grain orientation gives rise to an electron diffraction spot in the diffraction image. A selective aperture is applied to capture regions of the particular grain orientation on the graphene sample. The various grain orientations can be overlaid into a single image to give Figure D. The grain size of the CVD graphene shown is approximately 0.5-2 μm. High resolution TEM can be used to determine the structure of graphene grain boundaries. Contamination, not apparent in optical microscopy, can be observed by TEM (or scanning electron microscopy) given the much higher resolution. Metal nanoparticle residuals can be identified using TEM or SEM. Although TEM is very valuable in the investigation of graphene, it is very expensive, complex and time consuming.

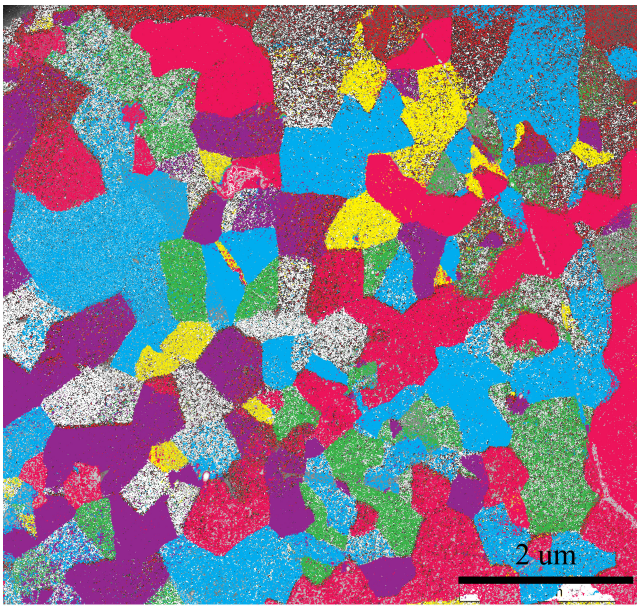

Figure 1.3.4. Dark field TEM image of CVD graphene. The various colors correspond to the different grain orientations on the graphene sample. The grain size is approximately 0.5-2 μm, typical of CVD growth at fast methane flow rates. The TEM image was obtained at 80 keV.

1.4 Graphene Applications

The extraordinary properties of graphene reported so far include high values of its Young's Modulus (~1,100 GPa), fracture strength (125 GPa), thermal conductivity (~5,000 W $m^{-1}K^{-1}$), mobility of charge carriers (200,000 cm^2 $V^{-1}s^{-1}$) and specific surface area (2,630 m^2 g^{-1}).[4–8,15] Therefore, graphene is proposed to be a great material for applications such as electronics, energy harvesting and storage, anti-corrosion, catalysis, and sensing.

The electrochemical properties of graphene electrodes were found to be particularly fascinating in applications such as energy harvesting and storage. A specific capacity of 540 $mAhg^{-1}$ was reported for graphene compared to 372 $mAhg^{-1}$ for graphite, the most commonly used anode material in lithium ion batteries.[56,57] The reason is believed to be the higher surface area and the ability to bind lithium ions more efficiently, forming a Li_2C_6 stoichiometry as opposed to LiC_6 in graphite.[58] Higher capacity, up to 2200 $mAhg^{-1}$, has been reported for graphene-nanoparticle mixtures.[59] Graphene is also tested as the electrode material in electrochemical double-layer capacitors.[60–62] The specific capacitance of modified graphene was reported to be 99 F/g and 135 F/g in organic and aqueous solvents, respectively. Furthermore, graphene exhibits a hydrogen adsorption capacity of 0.68 wt% at 77K and 1bar in fuel cell applications; it has a conversion efficiency of 14% as the electron acceptor material in photovoltaic devices; and it has demonstrated to be an extraordinary catalyst support for oxygen reduction and methanol oxidation.[57,63–67]

Graphene has been exploited as potential sensing materials. It has been shown to be sensitive to gas molecules such as CO, NO_2, H_2O, and NH_3.[68–72] The adsorption and desorption processes can be observed by the changes in resistance measured across the graphene sample. The changes in resistance were monitored over time. Electron donors, CO and NH_3, showed a positive change in resistance while electron acceptors, NO_2, H_2O, showed a negative change in resistance. Graphene has been demonstrated to be pH sensitive in a field effect transistor configuration. The change

in the Dirac point position is linearly related to the change in pH values, and slopes in the range of 2 to 99 mV/pH have been reported by various research groups.[73]

Graphene is an obvious candidate in electronic applications because of its astonishing charge carrier mobility, flexibility and transparency. One unique property of graphene is that it does not exhibit a band gap. In order to take full advantage of graphene's properties, a band gap has to be introduced. Chemical doping using gasses, organic molecules and metal atoms via adsorption and covalent functionalization have been reported to open up a band gap.[74–79] The efficiency of the various functionalization methods is not clear.

1.5 References

1. Boehm, H. P.; Clauss, A.; Fischer, G. O.; Hofmann, U. Das Adsorptionsverhalten Sehr Dünner Kohlenstoff-Folien. *Z. Anorg. Allg. Chem.* **1962**, *316*, 119–127.
2. Boehm, H. P.; Setton, R.; Stumpp, E. Nomenclature and Terminology of Graphite Intercalation Compounds. *Carbon* **1986**, *24*, 241–245.
3. Lu, X.; Yu, M.; Huang, H.; Ruoff, R. S. Tailoring Graphite with the Goal of Achieving Single Sheets. *Nanotech.* **1999**, *10*, 269.
4. Bolotin, K. I.; Sikes, K. J.; Jiang, Z.; Klima, M.; Fudenberg, G.; Hone, J.; Kim, P.; Stormer, H. L. Ultrahigh Electron Mobility in Suspended Graphene. *Solid State Commun.* **2008**, *146*, 351–355.
5. Morozov, S.; Novoselov, K.; Katsnelson, M.; Schedin, F.; Elias, D.; Jaszczak, J.; Geim, A. Giant Intrinsic Carrier Mobilities in Graphene and Its Bilayer. *Phys. Rev. Lett.* **2008**, *100*.
6. Lee, C.; Wei, X.; Kysar, J. W.; Hone, J. Measurement of the Elastic Properties and Intrinsic Strength of Monolayer Graphene. *Science* **2008**, *321*, 385–388.
7. Balandin, A. A.; Ghosh, S.; Bao, W.; Calizo, I.; Teweldebrhan, D.; Miao, F.; Lau, C. N. Superior Thermal Conductivity of Single-Layer Graphene. *Nano Lett.* **2008**, *8*, 902–907.
8. Cai, W.; Zhu, Y.; Li, X.; Piner, R. D.; Ruoff, R. S. Large Area Few-layer Graphene/graphite Films as Transparent Thin Conducting Electrodes. *Appl. Phys. Lett.* **2009**, *95*, 123115.

9. Li, X.; Zhu, Y.; Cai, W.; Borysiak, M.; Han, B.; Chen, D.; Piner, R. D.; Colombo, L.; Ruoff, R. S. Transfer of Large-Area Graphene Films for High-Performance Transparent Conductive Electrodes. *Nano Lett.* **2009**, *9*, 4359–4363.
10. Zhang, Y.; Small, J. P.; Pontius, W. V.; Kim, P. Fabrication and Electric-field-dependent Transport Measurements of Mesoscopic Graphite Devices. *Appl. Phys. Lett.* **2005**, *86*, 073104.
11. Novoselov, K. S. Electric Field Effect in Atomically Thin Carbon Films. *Science* **2004**, *306*, 666–669.
12. Meyer, J. C.; Geim, A. K.; Katsnelson, M. I.; Novoselov, K. S.; Booth, T. J.; Roth, S. The Structure of Suspended Graphene Sheets. *Nature* **2007**, *446*, 60–63.
13. Bolotin, K. I.; Sikes, K. J.; Hone, J.; Stormer, H. L.; Kim, P. Temperature-Dependent Transport in Suspended Graphene. *Phys. Rev. Lett.* **2008**, *101*.
14. Novoselov, K. S.; Jiang, D.; Schedin, F.; Booth, T. J.; Khotkevich, V. V.; Morozov, S. V.; Geim, A. K. Two-dimensional Atomic Crystals. *PNAS* **2005**, *102*, 10451–10453.
15. Li, X.; Cai, W.; An, J.; Kim, S.; Nah, J.; Yang, D.; Piner, R.; Velamakanni, A.; Jung, I.; Tutuc, E. *et al.* Large-Area Synthesis of High-Quality and Uniform Graphene Films on Copper Foils. *Science* **2009**, *324*, 1312–1314.
16. Bae, S.; Kim, H.; Lee, Y.; Xu, X.; Park, J.-S.; Zheng, Y.; Balakrishnan, J.; Lei, T.; Ri Kim, H.; Song, Y. I. *et al.* Roll-to-roll Production of 30-inch Graphene Films for Transparent Electrodes. *Nat. Nanotech.* **2010**, *5*, 574–578.

17. Kobayashi, T.; Bando, M.; Kimura, N.; Shimizu, K.; Kadono, K.; Umezu, N.; Miyahara, K.; Hayazaki, S.; Nagai, S.; Mizuguchi, Y. *et al.* Production of a 100-m-long High-quality Graphene Transparent Conductive Film by Roll-to-roll Chemical Vapor Deposition and Transfer Process. *Appl. Phys. Lett.* **2013**, *102*, 023112.

18. Muller, M.; Kubel, C.; Mullen, K. Giant Polycyclic Aromatic Hydrocarbons. *Chem. Eur. J.* **1998**, *4*, 2099–2109.

19. Tyutyulkov, N.; Madjarova, G.; Dietz, F.; Müllen, K. Is 2-D Graphite an Ultimate Large Hydrocarbon? 1. Energy Spectra of Giant Polycyclic Aromatic Hydrocarbons. *J. Phys. Chem. B* **1998**, *102*, 10183–10189.

20. Yang, X.; Dou, X.; Rouhanipour, A.; Zhi, L.; Räder, H. J.; Müllen, K. Two-Dimensional Graphene Nanoribbons. *J. Am. Chem. Soc.* **2008**, *130*, 4216–4217.

21. Wu, J.; Pisula, W.; Müllen, K. Graphenes as Potential Material for Electronics. *Chem. Rev.* **2007**, *107*, 718–747.

22. Stankovich, S.; Dikin, D. A.; Dommett, G. H. B.; Kohlhaas, K. M.; Zimney, E. J.; Stach, E. A.; Piner, R. D.; Nguyen, S. T.; Ruoff, R. S. Graphene-based Composite Materials. *Nature* **2006**, *442*, 282–286.

23. Stankovich, S.; Piner, R. D.; Chen, X.; Wu, N.; Nguyen, S. T.; Ruoff, R. S. Stable Aqueous Dispersions of Graphitic Nanoplatelets via the Reduction of Exfoliated Graphite Oxide in the Presence of Poly(sodium 4-styrenesulfonate). *J. Mat. Chem.* **2006**, *16*, 155.

24. Stankovich, S.; Dikin, D. A.; Piner, R. D.; Kohlhaas, K. A.; Kleinhammes, A.; Jia, Y.; Wu, Y.; Nguyen, S. T.; Ruoff, R. S. Synthesis of Graphene-based Nanosheets via Chemical Reduction of Exfoliated Graphite Oxide. *Carbon* **2007**, *45*, 1558–1565.

25. Hernandez, Y.; Nicolosi, V.; Lotya, M.; Blighe, F. M.; Sun, Z.; De, S.; McGovern, I. T.; Holland, B.; Byrne, M.; Gun'Ko, Y. K. *et al.* High-yield Production of Graphene by Liquid-phase Exfoliation of Graphite. *Nat. Nanotech.* **2008**, *3*, 563–568.

26. Gilje, S.; Han, S.; Wang, M.; Wang, K. L.; Kaner, R. B. A Chemical Route to Graphene for Device Applications. *Nano Lett.* **2007**, *7*, 3394–3398.

27. Li, D.; Müller, M. B.; Gilje, S.; Kaner, R. B.; Wallace, G. G. Processable Aqueous Dispersions of Graphene Nanosheets. *Nat. Nanotech.* **2008**, *3*, 101–105.

28. Staudenmaier, L. Verfahren Zur Darstellung Der Graphitsaure. *Ber. Dtsch. Chem. Ges.* **1898**, *31*, 1481–1499.

29. Brodie, B. C. Sur Le Poids Atomique Du Graphite. *Ann. Chim. Phys.* **1860**, *59*, 466–472.

30. Hummers Jr, W. S.; Offeman, R. E. Preparation of Graphitic Oxide. *J. Am. Chem. Soc.* **1958**, *80*, 1339–1339.

31. Berger, C.; Song, Z.; Li, T.; Li, X.; Ogbazghi, A. Y.; Feng, R.; Dai, Z.; Marchenkov, A. N.; Conrad, E. H.; First, P. N. *et al.* Ultrathin Epitaxial Graphite: 2D Electron Gas Properties and a Route Toward Graphene-based Nanoelectronics. *J. Phys. Chem. B* **2004**, *108*, 19912–19916.

32. Berger, C. Electronic Confinement and Coherence in Patterned Epitaxial Graphene. *Science* **2006**, *312*, 1191–1196.

33. Heer, W. A. de; Berger, C.; Wu, X.; First, P. N.; Conrad, E. H.; Li, X.; Li, T.; Sprinkle, M.; Hass, J.; Sadowski, M. L. *et al.* Epitaxial Graphene. *Solid State Commun.* **2007**, *143*, 92–100.

34. Reina, A.; Jia, X.; Ho, J.; Nezich, D.; Son, H.; Bulovic, V.; Dresselhaus, M. S.; Kong, J. Large Area, Few-Layer Graphene Films on Arbitrary Substrates by Chemical Vapor Deposition. *Nano Lett.* **2009**, *9*, 30–35.

35. Kim, K. S.; Zhao, Y.; Jang, H.; Lee, S. Y.; Kim, J. M.; Kim, K. S.; Ahn, J.-H.; Kim, P.; Choi, J.-Y.; Hong, B. H. Large-scale Pattern Growth of Graphene Films for Stretchable Transparent Electrodes. *Nature* **2009**, *457*, 706–710.

36. Sutter, P. W.; Flege, J.-I.; Sutter, E. A. Epitaxial Graphene on Ruthenium. *Nat. Mater.* **2008**, *7*, 406–411.

37. Stauber, T.; Peres, N.; Geim, A. Optical Conductivity of Graphene in the Visible Region of the Spectrum. *Phys. Rev. B* **2008**, *78*.

38. Nair, R. R.; Blake, P.; Grigorenko, A. N.; Novoselov, K. S.; Booth, T. J.; Stauber, T.; Peres, N. M. R.; Geim, A. K. Fine Structure Constant Defines Visual Transparency of Graphene. *Science* **2008**, *320*, 1308–1308.

39. Blake, P.; Hill, E. W.; Castro Neto, A. H.; Novoselov, K. S.; Jiang, D.; Yang, R.; Booth, T. J.; Geim, A. K. Making Graphene Visible. *Appl. Phys. Lett.* **2007**, *91*, 063124.

40. Rabe, J. P.; Buchholz, S. Commensurability and Mobility in 2-dimensional Molecular Patterns on Graphite. *Science* **1991**, *253*, 424–427.

41. Soler, J. M.; Baro, A. M.; García, N.; Rohrer, H. Interatomic Forces in Scanning Tunneling Microscopy: Giant Corrugations of the Graphite Surface. *Phys. Rev. Lett.* **1986**, *57*, 444–447.

42. Stolyarova, E.; Rim, K. T.; Ryu, S.; Maultzsch, J.; Kim, P.; Brus, L. E.; Heinz, T. F.; Hybertsen, M. S.; Flynn, G. W. High-resolution Scanning Tunneling Microscopy Imaging of Mesoscopic Graphene Sheets on an Insulating Surface. *PNAS* **2007**, *104*, 9209–9212.

43. Ferrari, A. C.; Meyer, J. C.; Scardaci, V.; Casiraghi, C.; Lazzeri, M.; Mauri, F.; Piscanec, S.; Jiang, D.; Novoselov, K. S.; Roth, S. *et al.* Raman Spectrum of Graphene and Graphene Layers. *Phys. Rev. Lett.* **2006**, *97*.

44. Ferrari, A. C.; Robertson, J. Interpretation of Raman Spectra of Disordered and Amorphous Carbon. *Phys. Rev. B* **2000**, *61*, 14095.

45. Casiraghi, C.; Pisana, S.; Novoselov, K. S.; Geim, A. K.; Ferrari, A. C. Raman Fingerprint of Charged Impurities in Graphene. *Appl. Phys. Lett.* **2007**, *91*, 233108.

46. Calizo, I.; Balandin, A. A.; Bao, W.; Miao, F.; Lau, C. N. Temperature Dependence of the Raman Spectra of Graphene and Graphene Multilayers. *Nano Lett.* **2007**, *7*, 2645–2649.

47. Matthews, M. J.; Pimenta, M. A.; Dresselhaus, G.; Dresselhaus, M. S.; Endo, M. Origin of Dispersive Effects of the Raman D Band in Carbon Materials. *Phys. Rev. B* **1999**, *59*, R6585–R6588.

48. Gupta, A.; Chen, G.; Joshi, P.; Tadigadapa, S.; Eklund, P. C. Raman Scattering from High-Frequency Phonons in Supported *n* -Graphene Layer Films. *Nano Lett.* **2006**, *6*, 2667–2673.

49. Pimenta, M. A.; Dresselhaus, G.; Dresselhaus, M. S.; Can?ado, L. G.; Jorio, A.; Saito, R. Studying Disorder in Graphite-based Systems by Raman Spectroscopy. *Phys. Chem. Chem. Phys.* **2007**, *9*, 1276.

50. Malard, L. M.; Pimenta, M. A.; Dresselhaus, G.; Dresselhaus, M. S. Raman Spectroscopy in Graphene. *Phys. Rep.* **2009**, *473*, 51–87.

51. Saha, S.; Waghmare, U.; Krishnamurthy, H.; Sood, A. Phonons in Few-layer Graphene and Interplanar Interaction: A First-principles Study. *Phys. Rev. B* **2008**, *78*.

52. Liu, H.; Ryu, S.; Chen, Z.; Steigerwald, M. L.; Nuckolls, C.; Brus, L. E. Photochemical Reactivity of Graphene. *J. Am. Chem. Soc.* **2009**, *131*, 17099–17101.

53. Sharma, R.; Baik, J. H.; Perera, C. J.; Strano, M. S. Anomalously Large Reactivity of Single Graphene Layers and Edges Toward Electron Transfer Chemistries. *Nano Lett.* **2010**, *10*, 398–405.

54. Meyer, J. C.; Kisielowski, C.; Erni, R.; Rossell, M. D.; Crommie, M. F.; Zettl, A. Direct Imaging of Lattice Atoms and Topological Defects in Graphene Membranes. *Nano Lett.* **2008**, *8*, 3582–3586.

55. Huang, P. Y.; Ruiz-Vargas, C. S.; Zande, A. M. van der; Whitney, W. S.; Levendorf, M. P.; Kevek, J. W.; Garg, S.; Alden, J. S.; Hustedt, C. J.; Zhu, Y. *et al.* Grains and Grain Boundaries in Single-layer Graphene Atomic Patchwork Quilts. *Nature* **2011**, *469*, 389–392.

56. Winter, M.; Besenhard, J. O.; Spahr, M. E.; Novak, P. Insertion Electrode Materials for Rechargeable Lithium Batteries. *Adv. Mater.* **1998**, *10*, 725–763.

57. Yoo, E.; Okata, T.; Akita, T.; Kohyama, M.; Nakamura, J.; Honma, I. Enhanced Electrocatalytic Activity of Pt Subnanoclusters on Graphene Nanosheet Surface. *Nano Lett.* **2009**, *9*, 2255–2259.

58. Liu, Y.; Xue, J. S.; Zheng, T.; Dahn, J. R. Mechanism of Lithium Insertion in Hard Carbons Prepared by Pyrolysis of Epoxy Resins. *Carbon* **1996**, *34*, 193–200.

59. Lee, J. K.; Smith, K. B.; Hayner, C. M.; Kung, H. H. Silicon Nanoparticles–graphene Paper Composites for Li Ion Battery Anodes. *Chem. Commun.* **2010**, *46*, 2025.

60. Simon, P.; Gogotsi, Y. Materials for Electrochemical Capacitors. *Nat. Mater.* **2008**, *7*, 845–854.

61. Stoller, M. D.; Park, S.; Zhu, Y.; An, J.; Ruoff, R. S. Graphene-Based Ultracapacitors. *Nano Lett.* **2008**, *8*, 3498–3502.

62. Wang, Y.; Shi, Z.; Huang, Y.; Ma, Y.; Wang, C.; Chen, M.; Chen, Y. Supercapacitor Devices Based on Graphene Materials. *J. Phys. Chem. C* **2009**, *113*, 13103–13107.

63. Srinivas, G.; Zhu, Y.; Piner, R.; Skipper, N.; Ellerby, M.; Ruoff, R. Synthesis of Graphene-like Nanosheets and Their Hydrogen Adsorption Capacity. *Carbon* **2010**, *48*, 630–635.

64. Li, Y.; Tang, L.; Li, J. Preparation and Electrochemical Performance for Methanol Oxidation of Pt/graphene Nanocomposites. *Electrochem. Comm.* **2009**, *11*, 846–849.

65. Seger, B.; Kamat, P. V. Electrocatalytically Active Graphene-Platinum Nanocomposites. Role of 2-D Carbon Support in PEM Fuel Cells. *J. Phys. Chem. C* **2009**, *113*, 7990–7995.

66. Xu, C.; Wang, X.; Zhu, J. Graphene−Metal Particle Nanocomposites. *J. Phys. Chem. C* **2008**, *112*, 19841–19845.

67. Kou, R.; Shao, Y.; Wang, D.; Engelhard, M. H.; Kwak, J. H.; Wang, J.; Viswanathan, V. V.; Wang, C.; Lin, Y.; Wang, Y. *et al.* Enhanced Activity and Stability of Pt Catalysts on Functionalized Graphene Sheets for Electrocatalytic Oxygen Reduction. *Electrochem. Comm.* **2009**, *11*, 954–957.

68. Schedin, F.; Geim, A. K.; Morozov, S. V.; Hill, E. W.; Blake, P.; Katsnelson, M. I.; Novoselov, K. S. Detection of Individual Gas Molecules Adsorbed on Graphene. *Nat. Mater.* **2007**, *6*, 652–655.

69. Leenaerts, O.; Partoens, B.; Peeters, F. Adsorption of H2O, NH3, CO, NO2, and NO on Graphene: A First-principles Study. *Phys. Rev. B* **2008**, *77*.

70. Huang, B.; Li, Z.; Liu, Z.; Zhou, G.; Hao, S.; Wu, J.; Gu, B.-L.; Duan, W. Adsorption of Gas Molecules on Graphene Nanoribbons and Its Implication for Nanoscale Molecule Sensor. *J. Phys. Chem. C* **2008**, *112*, 13442–13446.

71. Fowler, J. D.; Allen, M. J.; Tung, V. C.; Yang, Y.; Kaner, R. B.; Weiller, B. H. Practical Chemical Sensors from Chemically Derived Graphene. *ACS Nano* **2009**, *3*, 301–306.

72. Dan, Y.; Lu, Y.; Kybert, N. J.; Luo, Z.; Johnson, A. T. C. Intrinsic Response of Graphene Vapor Sensors. *Nano Lett.* **2009**, *9*, 1472–1475.

73. Ohno, Y.; Maehashi, K.; Yamashiro, Y.; Matsumoto, K. Electrolyte-Gated Graphene Field-Effect Transistors for Detecting pH and Protein Adsorption. *Nano Lett.* **2009**, *9*, 3318–3322.

74. Bostwick, A.; Ohta, T.; Seyller, T.; Horn, K.; Rotenberg, E. Quasiparticle Dynamics in Graphene. *Nat. Phys.* **2006**, *3*, 36–40.

75. Ohta, T. Controlling the Electronic Structure of Bilayer Graphene. *Science* **2006**, *313*, 951–954.

76. Wang, X.; Tabakman, S. M.; Dai, H. Atomic Layer Deposition of Metal Oxides on Pristine and Functionalized Graphene. *J. Am. Chem. Soc.* **2008**, *130*, 8152–8153.

77. Chen, W.; Chen, S.; Qi, D. C.; Gao, X. Y.; Wee, A. T. S. Surface Transfer p-Type Doping of Epitaxial Graphene. *J. Am. Chem. Soc.* **2007**, *129*, 10418–10422.

78. Gierz, I.; Riedl, C.; Starke, U.; Ast, C. R.; Kern, K. Atomic Hole Doping of Graphene. *Nano Lett.* **2008**, *8*, 4603–4607.

79. Chen, J.-H.; Jang, C.; Adam, S.; Fuhrer, M. S.; Williams, E. D.; Ishigami, M. Charged-impurity Scattering in Graphene. *Nat. Phys.* **2008**, *4*, 377–381.

Chapter 2

Investigating Graphene's Chemical Properties Using Cyclic Voltammetry

2.1 Introduction

Graphene exhibits many unique properties. It is a zero band gap semi-metal, has remarkably high charge carrier mobility, is 98% transparent, and has extraordinary mechanical strength and thermal conductivity.[1–6] The material has stimulated an enormous amount of research across many scientific disciplines from physics to biology to engineering. There is increased interest in understanding the chemistry of graphene, controlling its properties through chemical modifications, and using it in applications such as energy storage, sensors, catalysis, and electronics, just to name a few.

Several techniques have been employed to investigate the surface chemistry of graphene. Raman mapping is routinely used to examine graphene samples that are covalently functionalized with small organic molecules.[7–10] The D band intensity, caused by disorder, is higher with chemically modified graphene compared to pristine graphene. The ratio between the D peak intensity and the G peak intensity can be plotted over an area of interest. The spatial map is useful in monitoring the progress of the functionalization reaction on graphene. Scanning tunneling microscopy has been employed to study the self-assembly of molecules on graphene.[11] Despite these efforts,

current techniques provide limited information about an important aspect of chemistry – the reactivity of graphene towards chemical reactions.

Electrochemistry offers a library of tools to examine both heterogeneous and homogeneous electron transfer kinetics.[12–14] For instance, cyclic voltammetry can be used to investigate heterogeneous electron transfer at the electrode-solution interface as well as coupled chemical reactions. Rotating disk electrode voltammetry can provide information about heterogeneous electron transfers, homogenous electron transfers, and catalytic reactions. Cyclic voltammetry has long been used to study interesting carbon nano-structures such as graphene, carbon nanotubes and fullerene films.[15–20]

In this chapter, we discuss the electrochemistry of two types of graphene electrodes – mechanically exfoliated graphene and chemical vapor deposited (CVD) graphene. Mechanically exfoliated graphene was chosen for its quality and CVD graphene was chosen for its size, scalability, and its potential for practical applications. Cyclic voltammetry allows us to determine the effective area of the graphene electrodes as well as calculate the rate of heterogeneous electron transfer of hydroxymethyl ferrocene (FcMeOH) at graphene electrodes.

2.2 Experimental

Materials. All chemicals were used as received without further purification unless otherwise stated. The DI water used in these experiments was purified with a Millipore water purification system. Hydroxymethyl ferrocene (5.2 mM FcMeOH,

Alfa Aesar) with potassium chloride (0.1 M KCl, Mallinckrodt Chemicals) in water were used as the redox mediator and electrolyte, respectively.

Graphene electrode fabrication. Mechanically exfoliated graphene and CVD graphene were prepared using published methods described in Chapter 1. Two metal leads (1 nm Cr/50 nm Au, 99.999%, Kurt J. Lesker Company) were patterned on one end of the graphene sheet using lithography. To isolate the metal leads from the redox mediator/electrolyte solution, 100 nm of Al_2O_3 and 600 nm of Parylene were deposited using e-beam evaporation and thermal evaporation. A window exposing graphene was defined lithographically followed by plasma etch (60 mTorr, 50 sccm O_2, 150 W, 2 min) and base etch (AZ 300 MIF photoresist developer, Clariant Corportation, Somerville, NJ) to remove Parylene and Al_2O_3, respectively. The graphene working electrodes were annealed at 350 ℃ under vacuum to remove organic residuals from the fabrication process.

Electrochemistry. SECM and electrochemical measurements were carried out using a CHI 900 SECM/potentiostat (CH Instruments, Austin, TX). Mechanically exfoliated graphene and CVD graphene were employed as working electrodes. A Ag/AgCl reference electrode and a Au wire counter electrode were used. A micromanipulator was used to insert the graphene electrode into solution. The electrochemical experiment was conducted in a Faraday cage on an optical table to reduce electronic and acoustic noise.

2.3 Graphene Electrode Fabrication

The electrochemical properties of graphene electrodes were found to be particularly fascinating in applications such as energy harvesting and storage. A specific capacity of 540 $mAhg^{-1}$ was reported for graphene compared to 372 $mAhg^{-1}$ for graphite, the most commonly used anode material in lithium ion batteries.[21,22] The reason is believed to be the higher surface area and the ability to bind lithium ions more efficiently forming Li_2C_6 stoichiometry as opposed to LiC_6 in graphite.[23] Higher capacity up to 2200 $mAhg^{-1}$ has been reported for graphene-nanoparticle mixtures.[24] Graphene was also tested as the electrode material in electrochemical double-layer capacitors.[25–27] The specific capacitance of modified graphene was reported to be 99 Fg^{-1} and 135 Fg^{-1} in organic and aqueous solvents, respectively. Furthermore, graphene exhibits a hydrogen adsorption capacity of 0.68 wt% at 77K and 1bar in fuel cell applications; it has a conversion efficiency of 14% as the electron acceptor material in photovoltaic devices; and it has demonstrated to be an extraordinary catalyst support for oxygen reduction and methanol oxidation.[22,28–32] However, these studies were graphene flakes deposited on electrochemically active substrates such as platinum, gold and glassy carbon. It is not clear whether the remarkable electrochemical performance is extrinsically due to the properties of graphene or simply a reflection of the increased surface area and the exposure of electrochemically active supporting substrate.[33] An individual single-layer graphene electrode on an insulating substrate was designed and fabricated.

Figure 2.3.1 illustrates the fabrication process of the graphene electrodes. Mechanically exfoliated graphene was derived from Kish graphite using the Scotch tape method described in Chapter 1.2. The graphene was placed on to a 300 nm SiO_2/Si substrate. Metal contacts need to be extended from the graphene sheet for electrical connections with the potentiostat. A layer of photoresist was spin coated on the substrate, and the shape of the metal contacts was defined lithographically. Gold (Au) was then deposited via evaporation to generate the desired pattern. Al_2O_3 and Parylene were deposited to prevent electrochemical signals from the Au contacts. Graphene of a defined area was exposed for electrochemical measurements. The size of the window for exfoliated graphene was 15×15 μm^2. Finally, the graphene electrode was annealed at 350 ℃ under vacuum to remove any remaining organic residues from the fabrication process remained on the graphene surface. This design ensures that graphene is the only electrochemically active surface in contact with the solution, and more importantly that the area can be measured with accuracy. Chemical vapor deposited graphene was grown according to method described in Chapter 1.2. The area of the CVD graphene electrode defined lithographically was 380×500 μm^2. Contact resistance of the electrodes was measured to be in the range of 20-1000 Ω.

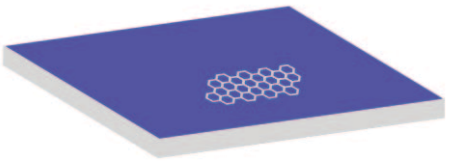

Graphene on SiO_2/Si

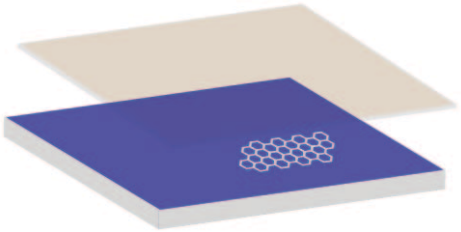

Photoresist deposition - light sensitive polymer is deposited for pattern generation

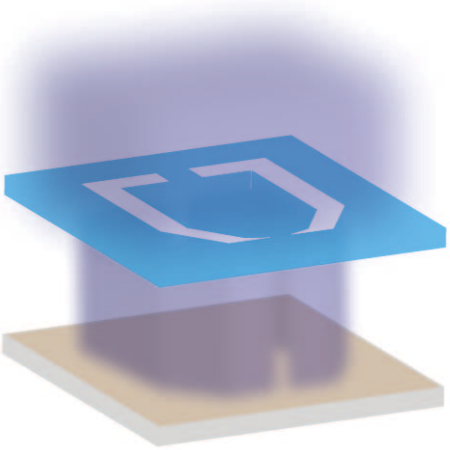

Expose - Exposure to UV light generates desired pattern on chip

Develop - Photoresist exposed to light becomes soluble in developer and can be washed away

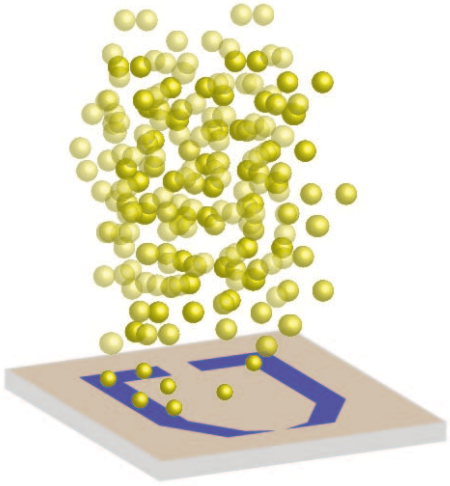

Au deposition - Au is deposited using e-beam evaporation

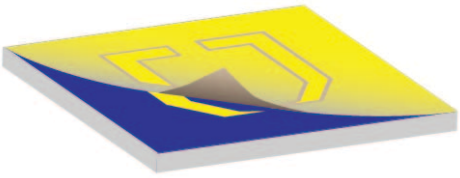

Lift-off - Au on desired pattern remains, Au on photoresist gets removed

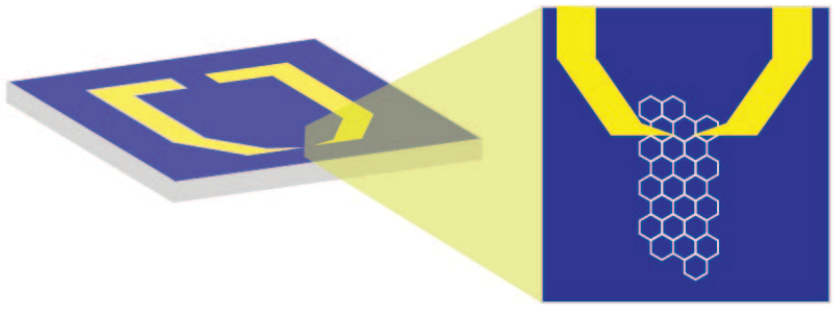

Au contacts are deposited on graphene

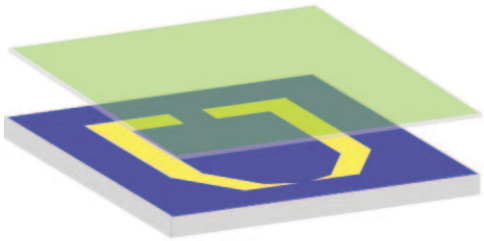

Protect - Al_2O_3

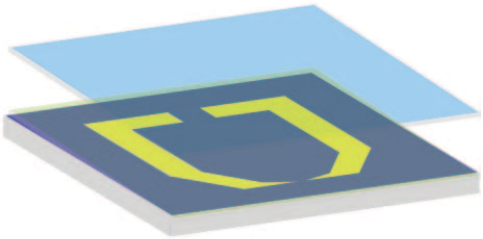

Protect - Parylene

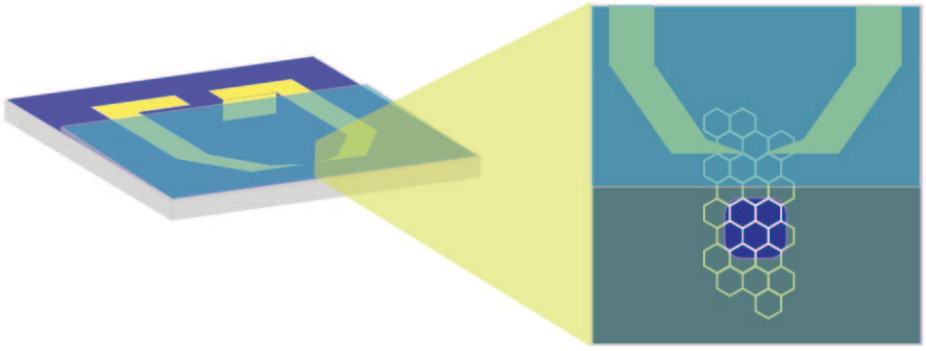

Expose - Expose graphene with a defined area

Figure 2.3.1. Schematics of the graphene electrode fabrication process.

The mechanically exfoliated and CVD graphene working electrodes were examined using various characterization methods. Sharp 2D peaks at 2700 cm^{-1} were observed in the Raman spectra of both types of graphene electrodes. No D peak was observed for the electrodes derived from mechanically exfoliated graphene.[34] In comparison, a small D peak at 1350 cm^{-1} was observed for CVD graphene electrodes indicating the presence of defects.[35–37] Atomic force microscopy (AFM) images further confirmed these observations. Predominately smooth surfaces were observed for electrodes made of exfoliated graphene sheets. Nanoscale surface corrugations and wrinkles are intrinsic to graphene as reported by many research groups.[38,39] In contrast, electrodes made of CVD graphene appear to contain more topographical features, possibly due to defects and contamination. The results were consistent with reported Raman and AFM data. Although clear differences in quality between mechanically exfoliated graphene and CVD graphene is observed, no clear difference was found before and after the graphene electrode fabrication process.

(A)

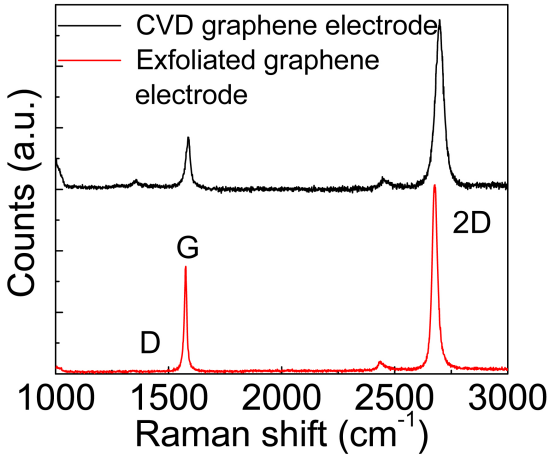

(B)

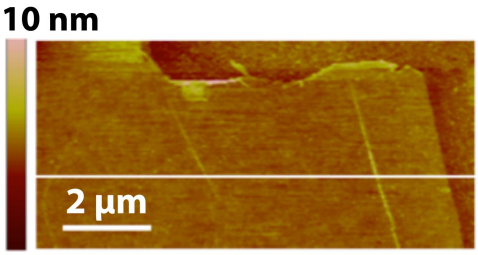

(C)

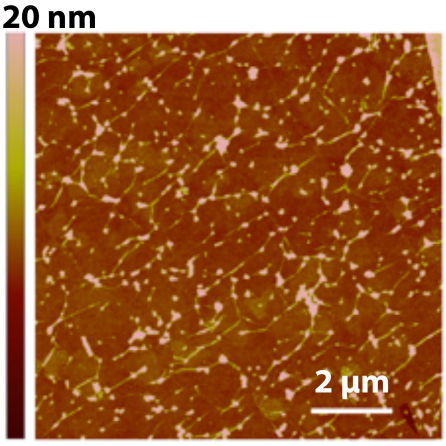

Figure 2.3.2. Characterization of graphene after the fabrication processes. (A) Raman spectra of mechanically exfoliated graphene (red) and CVD graphene (black)

electrodes. Sharp 2D peaks at 2700 cm^{-1} are observed for both electrodes. A small D at 1350 cm^{-1} is observed for CVD graphene. (B) AFM image of mechanically exfolicated graphene indicating a clean and smooth surface. (C) AFM image of CVD graphene representative of imperfections.

2.4 Cyclic Voltammetry

Cyclic voltammetry is a simple technique that reveals valuable information about electrochemical reactions at the electrode-solution interface. A three-electrode configuration is used in the cyclic voltammetry experiment. The working electrode, graphene, drives the electrochemical reaction as the potential applied to it is varied. This potential is referenced to a Ag/AgCl electrode. When a redox reaction occurs, current flows in response to the heterogeneous electron transfer between the redox mediator and the working electrode. The current profile is dependent on a variety of parameters, for example, the area of the working electrode, the rate of the heterogeneous electron transfer, and coupled chemical reactions.

The area of the electrochemically-active surface plays an important role in electrochemical measurements. The intensity of electrochemical signals is directly proportional to the area of the working electrode – the reason behind the graphene working electrode design. Furthermore, the shape of the cyclic voltammograms is also influenced by the working electrode area.

The diffusive flux near the electrode surface of a conventional, or "large", electrode is considered to be linear and homogeneous in spite of the very small contribution from the edges of the electrode. The diffusion layer is time dependent[14]

$$\delta = \sqrt{2D_{Ox}t} \qquad 2.4.2$$

For a conventional electrode with a radius of 2.5 mm, the diffusion layer reaches comparable dimension of the electrode in approximately 3000 seconds. Mass transport is affected by diffusion and convection due to this time scale. Hence, in the cyclic voltammogram of a "large" or conventional electrode, we observe an increase in current corresponding to the kinetically limited regime followed a decrease in current corresponding to the mass transport effect.

The current profile is different when the diffusion length is comparable to the size of the electrode. In this case, the diffusive flux from the edge of the electrode has a much greater contribution, therefore, we can no longer assume semi-infinite linear diffusion.[40] The diffusion layer reaches a limiting value of

$$\delta = \frac{\pi r}{4} \qquad 2.4.3$$

where *r* is the radius of the electrode.[14] For an electrode with a radius of 7.5 μm, it takes less than 1 second to reach the diffusion length. The current profile can be described by[41]

$$i(t) = 4nFD_{Ox}rC_{Ox}^{*}f(\tau) \qquad 2.4.4$$

$$f(\tau) = 0.7854 + 0.8862\tau^{-1/2} + 0.2146e^{-0.7823\tau^{-1/2}} \qquad 2.4.5$$

$$\tau = \frac{4D_{Ox}t}{r^2} \qquad 2.4.6$$

Evaluating these equations at diffusion limited conditions, the limiting steady state current is

$$i_{ss} = 4nFD_{Ox}C^*_{Ox}r \qquad 2.4.7$$

A sigmoidal steady state response is observed. This type of electrode is known as an ultramicroelectrode, and the radius is usually less than 25 μm. It is possible to observe a peak-shaped voltammogram with an ultramicroelectrode when an extremely fast sweep rate is used.

We have observed both phenomena in the cyclic voltammograms of the graphene electrodes. The redox mediator, hydroxymethyl ferrocene (FcMeOH), offers a simple one-electron process with no kinetic complications, and it is ideal for the investigation of new electrode materials.

The mechanically exfoliated graphene electrodes are small, with an area of approximately 100 μm^2. As anticipated, a steady state behavior was observed, characteristic of an ultramicroelectrode (Figure 2.4.1). In addition, the current profile was not affected by varying the sweep rate. The effective area of the mechanically exfoliated graphene electrode was calculated from Equation 2.4.7 to be 117 ± 8 μm^2. The area measured using AFM was 130 μm^2. The small discrepancy could be due to the nature of the two different measurement as well as contaminations and imperfections on the graphene surface.

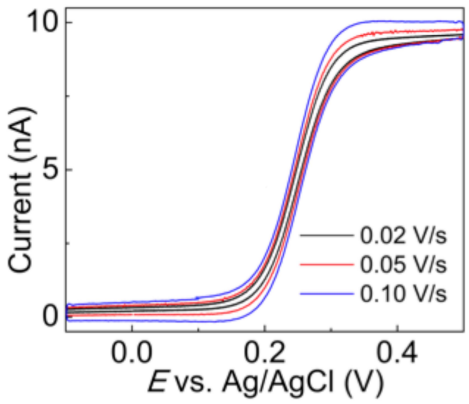

Figure 2.4.1. Cyclic voltammogram of a mechanically exfoliated graphene electrode. A steady state behavior is observed, characteristic of an ultramicroelectrode. The steady state current is not affected by the sweep rate. The area of the graphene electrode was found to be 117 ± 8 μm^2.

The size of ultramicroelectrodes offers the ability to measure fast reaction kinetics. A plot of E vs. $log[(i_{ss}-i)/i]$, where i is the current measured at an applied potential E, is commonly used to determine the reversibility of an electrochemical reaction. The plot yields a slope of $59/n$ for a reversible n electron transfer process. A much steeper slope should be observed for quasi-reversible processes. Figure 2.4.2A represents a plot of E vs. $log[(i_{ss}-i)/i]$ for the mechanically exfoliated graphene electrode. A slope of 58.3 ± 0.3 mV was determined for the one electron process. The plot and the current profile suggest that the heterogeneous electron transfer is reversible. The standard rate of heterogeneous electron transfer, k^0, can be obtained by using Equation 2.4.8 as illustrated in Figure 2.4.2B.[17]

$$i = \frac{i_{ss}}{1+e^{-F(E-E^{0\prime})/RT}+(\frac{FAC^{*}_{Ox}k^{0}}{i_{ss}})^{-1}e^{-F(1-\alpha)(E-E^{0\prime})/RT}} \qquad 2.4.8$$

E is the applied potential, $E^{0\prime}$ is the formal potential of the redox mediator, R is the gas constant, T is temperature, and α is the transfer coefficient. Satisfactory fits are obtained for k^{0} values greater than 0.5 cm/s, hence the lower limit of the heterogeneous electron transfer rate of FcMeOH at the mechanically exfoliated graphene electrode is 0.5 cm/s.

(A)

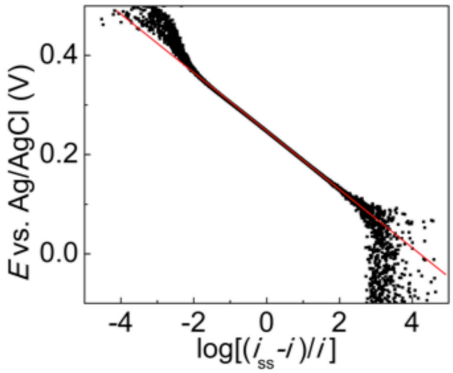

(B)

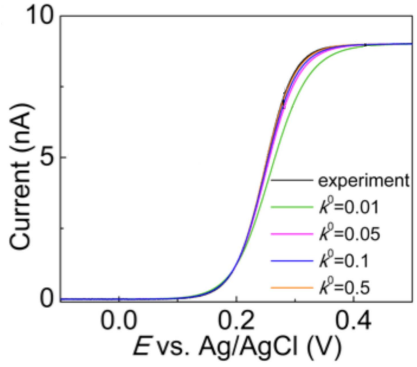

Figure 2.4.2. Analysis of heterogeneous electron transfer kinetics of FcMeOH at a mechanically exfoliated graphene electrode. (A) A slope of 58.2 was determined

indicating a reversible electron transfer process. (B) Fitting the cyclic voltammogram to Equation 2.4.8 yielded a heterogeneous electron transfer rate of at least 0.5 cm/s.

The area of the CVD graphene electrode was approximately 1000 times greater than that of the mechanically exfoliated graphene electrode. As anticipated, peak-shaped voltammograms are observed given the large electrode area as illustrated in Figure 2.4.3. An increase in peak current is observed with an increase in sweep rate. In addition to the electrode area, the peak current is also a function of the square root of sweep rate, $v^{1/2}$, as demonstrated in the Randles-Sevcik equation:

$$i_p = (2.69\times10^5)n^{3/2}AD_{Ox}^{1/2}C_{Ox}^{*}v^{1/2} \qquad 2.4.9$$

The area of the electrode was calculated to be 0.172 ± 0.006 mm^2, in good agreement with the designed area of 0.19 mm^2.

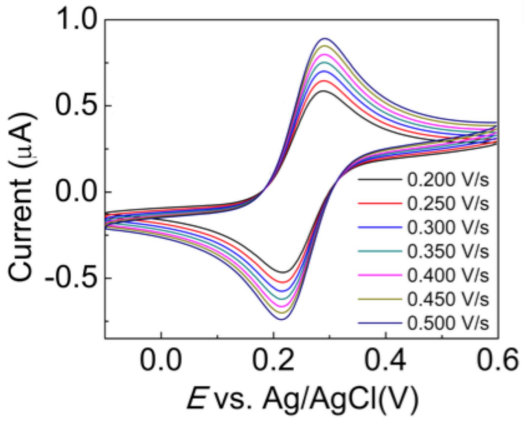

Figure 2.4.3. Cyclic voltammogram of a CVD graphene electrode. An increase in peak current is observed with an increase in sweep rate. The effective area was calculated to be 0.172 ± 0.006 mm^2.

The heterogeneous electron transfer rate can be derived from the potential difference between the oxidation and reduction peaks, ΔE_p, as a function of sweep rate, ν. The current measured is in the order of micro-Ampere, thus contributions from the contact resistance of the working electrode has to be considered. ΔE_p are converted into the dimensionless Nicholson's kinetic parameter, ψ, then the standard heterogeneous electron transfer rate, k^0, can be determined from[12,14,42]

$$\psi = k^0 \nu^{-1/2} \sqrt{\frac{RT}{\pi n F D_{Ox}}} \qquad 2.4.10$$

The standard heterogeneous electron transfer was calculated to be 0.042 ± 0.002 cm/s as illustrated in Figure 2.4.4. To ensure that we have not overestimated the contribution from resistance, we calculated k^0 without resistance correction. The value of was determined to be 0.037 cm/s, which indicates that contact resistance of 1100 Ω has a small effect on the rate of heterogeneous electron transfer.

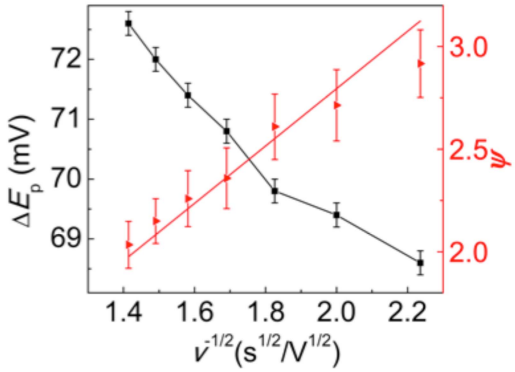

Figure 2.4.4. Analysis of heterogeneous electron transfer kinetics of FcMeOH at a CVD graphene electrode. The heterogeneous electron transfer rate was found to be 0.042 ± 0.002 cm/s.

The values of k^0 can be compared to those reported for ferrocene derivatives at sp^2 carbon surfaces. Using similar experimental and analysis methods, we found a k^0 of 0.007 cm/s at the basal plane of a freshly cleaved HOPG electrode. A k^0 of 0.003 cm/s has been reported for ferrocenedicarboxylic acid at HOPG electrodes.[43,44] Very fast heterogeneous electron transfer rates of 1.1 cm/s and 4 cm/s have been reported for hydroxymethyl ferrocene and ferrocenylmethyl-trimethylammonium, respectively, at single wall carbon nanotube electrodes.[17,45] The comparison is illustrated in Table 2.4.1. The enhanced k^0 values at graphene and single wall carbon nanotubes are likely related to the favorable chemical reactivity when compared to the basal plane of HOPG.[46] This enhancement could be a result of the intrinsic corrugations of graphene and carbon nanotube which are not present in the atomically flat HOPG surface. The corrugations lead to considerable curvature and strain in graphene sheets at the atomic level, hence activate the graphene surface towards chemical reactions, which in turn contribute to the enhancement of k^0.

Electrode Material	**Redox Mediator**	**k^0 (cm/s)**
HOPG	Ferrocenedicarboxylic acid	0.003
HOPG	Hydroxymethyl ferrocene	0.007
Mechanically exfoliated graphene	Hydroxymethyl ferrocene	0.5
CVD graphene	Hydroxymethyl ferrocene	0.042
Carbon nanotube	Hydroxymethyl ferrocene	1.1
Carbon nanotube	ferrocenylmethyl-trimethylammonium	4

Table 2.4.1. Heterogeneous electron transfer rates of ferrocene derivatives at various sp^2 carbon electrodes.

2.5 Conclusions

Individual, single-layer graphene working electrodes with a defined area on an insulating substrate were designed and fabricated. The geometric areas determined electrochemically were in agreement with the expected electrode areas. The standard rates of heterogeneous electron transfer of mechanically exfoliated graphene and CVD graphene have been calculated to be 0.5 cm/s and 0.042 cm/s. The results show that cyclic voltammetry is valuable in investigating the heterogeneous electron transfer at the redox mediator-graphene interface. Nevertheless, alternative method is necessary to further understand the differences between the surface chemistry of the various types of graphene electrodes as a clear difference in the rate of heterogeneous electron transfer between mechanically exfoliated graphene and CVD graphene is observed.

2.6 References

1. Bolotin, K. I.; Sikes, K. J.; Jiang, Z.; Klima, M.; Fudenberg, G.; Hone, J.; Kim, P.; Stormer, H. L. Ultrahigh Electron Mobility in Suspended Graphene. *Solid State Commun.* **2008**, *146*, 351–355.
2. Morozov, S.; Novoselov, K.; Katsnelson, M.; Schedin, F.; Elias, D.; Jaszczak, J.; Geim, A. Giant Intrinsic Carrier Mobilities in Graphene and Its Bilayer. *Phys. Rev. Lett.* **2008**, *100*.
3. Lee, C.; Wei, X.; Kysar, J. W.; Hone, J. Measurement of the Elastic Properties and Intrinsic Strength of Monolayer Graphene. *Science* **2008**, *321*, 385–388.
4. Balandin, A. A.; Ghosh, S.; Bao, W.; Calizo, I.; Teweldebrhan, D.; Miao, F.; Lau, C. N. Superior Thermal Conductivity of Single-Layer Graphene. *Nano Lett.* **2008**, *8*, 902–907.
5. Cai, W.; Zhu, Y.; Li, X.; Piner, R. D.; Ruoff, R. S. Large Area Few-layer Graphene/graphite Films as Transparent Thin Conducting Electrodes. *Appl. Phys. Lett.* **2009**, *95*, 123115.
6. Li, X.; Cai, W.; An, J.; Kim, S.; Nah, J.; Yang, D.; Piner, R.; Velamakanni, A.; Jung, I.; Tutuc, E. *et al.* Large-Area Synthesis of High-Quality and Uniform Graphene Films on Copper Foils. *Science* **2009**, *324*, 1312–1314.
7. Sharma, R.; Baik, J. H.; Perera, C. J.; Strano, M. S. Anomalously Large Reactivity of Single Graphene Layers and Edges Toward Electron Transfer Chemistries. *Nano Lett.* **2010**, *10*, 398–405.

8. Liu, H.; Ryu, S.; Chen, Z.; Steigerwald, M. L.; Nuckolls, C.; Brus, L. E. Photochemical Reactivity of Graphene. *J. Am. Chem. Soc.* **2009**, *131*, 17099–17101.
9. Ryu, S.; Han, M. Y.; Maultzsch, J.; Heinz, T. F.; Kim, P.; Steigerwald, M. L.; Brus, L. E. Reversible Basal Plane Hydrogenation of Graphene. *Nano Lett.* **2008**, *8*, 4597–4602.
10. Elias, D. C.; Nair, R. R.; Mohiuddin, T. M. G.; Morozov, S. V.; Blake, P.; Halsall, M. P.; Ferrari, A. C.; Boukhvalov, D. W.; Katsnelson, M. I.; Geim, A. K. Control of Graphene's Properties by Reversible Hydrogenation: Evidence for Graphane. *Science* **2009**, *323*, 610–613.
11. Wang, Q. H.; Hersam, M. C. Room-temperature Molecular-resolution Characterization of Self-assembled Organic Monolayers on Epitaxial Graphene. *Nat. Chem.* **2009**, *1*, 206–211.
12. Nicholson, R. S. Theory and Application of Cyclic Voltammetry for Measurement of Electrode Reaction Kinetics. *Anal. Chem.* **1965**, *37*, 1351–1355.
13. Oldham, K. B.; Myland, J. C.; Zoski, C. G.; Bond, A. M. Kinetic Parameters from Steady-state Voltammograms at Microdisc Electrodes. *J. of Electroanal. Chem. and Interf. Electrochem.* **1989**, *270*, 79–101.
14. Bard, A. J.; Faulkner, L. R. *Electrochemical Methods*; 2nd ed.; John Wiley & Sons: Hoboken, NJ, 2000.
15. McCreery, R. L. Advanced Carbon Electrode Materials for Molecular Electrochemistry. *Chem. Rev.* **2008**, *108*, 2646–2687.

16. Campbell, J. K.; Sun, L.; Crooks, R. M. Electrochemistry Using Single Carbon Nanotubes. *J. Am. Chem. Soc.* **1999**, *121*, 3779–3780.

17. Heller, I.; Kong, J.; Heering, H. A.; Williams, K. A.; Lemay, S. G.; Dekker, C. Individual Single-Walled Carbon Nanotubes as Nanoelectrodes for Electrochemistry. *Nano Lett.* **2005**, *5*, 137–142.

18. Chlistunoff, J.; Cliffel, D.; Bard, A. J. Electrochemistry of Fullerene Films. *Thin Solid Films* **1995**, *257*, 166–184.

19. Alehashem, S.; Chambers, F.; Strojek, J. W.; Swain, G. M.; Ramesham, R. Cyclic Voltammetric Studies of Charge Transfer Reactions at Highly Boron-doped Polycrystalline Diamond Thin-film Electrodes. *Anal. Chem.* **1995**, *67*, 2812–2821.

20. Pleskov, Y. V. Electrochemistry of Diamond: A Review. *Russ. J. Electrochem.* **2002**, *38*, 1275–1291.

21. Winter, M.; Besenhard, J. O.; Spahr, M. E.; Novak, P. Insertion Electrode Materials for Rechargeable Lithium Batteries. *Adv. Mater.* **1998**, *10*, 725–763.

22. Yoo, E.; Okata, T.; Akita, T.; Kohyama, M.; Nakamura, J.; Honma, I. Enhanced Electrocatalytic Activity of Pt Subnanoclusters on Graphene Nanosheet Surface. *Nano Lett.* **2009**, *9*, 2255–2259.

23. Liu, Y.; Xue, J. S.; Zheng, T.; Dahn, J. R. Mechanism of Lithium Insertion in Hard Carbons Prepared by Pyrolysis of Epoxy Resins. *Carbon* **1996**, *34*, 193–200.

24. Lee, J. K.; Smith, K. B.; Hayner, C. M.; Kung, H. H. Silicon Nanoparticles–graphene Paper Composites for Li Ion Battery Anodes. *Chem. Commun.* **2010**, *46*, 2025.

25. Simon, P.; Gogotsi, Y. Materials for Electrochemical Capacitors. *Nat. Mater.* **2008**, *7*, 845–854.

26. Stoller, M. D.; Park, S.; Zhu, Y.; An, J.; Ruoff, R. S. Graphene-Based Ultracapacitors. *Nano Lett.* **2008**, *8*, 3498–3502.

27. Wang, Y.; Shi, Z.; Huang, Y.; Ma, Y.; Wang, C.; Chen, M.; Chen, Y. Supercapacitor Devices Based on Graphene Materials. *J. Phys. Chem. C* **2009**, *113*, 13103–13107.

28. Srinivas, G.; Zhu, Y.; Piner, R.; Skipper, N.; Ellerby, M.; Ruoff, R. Synthesis of Graphene-like Nanosheets and Their Hydrogen Adsorption Capacity. *Carbon* **2010**, *48*, 630–635.

29. Li, Y.; Tang, L.; Li, J. Preparation and Electrochemical Performance for Methanol Oxidation of Pt/graphene Nanocomposites. *Electrochem. Comm.* **2009**, *11*, 846–849.

30. Seger, B.; Kamat, P. V. Electrocatalytically Active Graphene-Platinum Nanocomposites. Role of 2-D Carbon Support in PEM Fuel Cells. *J. Phys. Chem. C* **2009**, *113*, 7990–7995.

31. Xu, C.; Wang, X.; Zhu, J. Graphene-Metal Particle Nanocomposites. *J. Phys. Chem. C* **2008**, *112*, 19841–19845.

32. Kou, R.; Shao, Y.; Wang, D.; Engelhard, M. H.; Kwak, J. H.; Wang, J.; Viswanathan, V. V.; Wang, C.; Lin, Y.; Wang, Y. *et al.* Enhanced Activity and Stability of Pt Catalysts on Functionalized Graphene Sheets for Electrocatalytic Oxygen Reduction. *Electrochem. Comm.* **2009**, *11*, 954–957.

33. Murray, R. Roses and Raspberries. *Anal. Chem.* **2010**, *82*, 3405–3405.

34. Ferrari, A. C.; Meyer, J. C.; Scardaci, V.; Casiraghi, C.; Lazzeri, M.; Mauri, F.; Piscanec, S.; Jiang, D.; Novoselov, K. S.; Roth, S. *et al.* Raman Spectrum of Graphene and Graphene Layers. *Phys. Rev. Lett.* **2006**, *97*.

35. Levendorf, M. P.; Ruiz-Vargas, C. S.; Garg, S.; Park, J. Transfer-Free Batch Fabrication of Single Layer Graphene Transistors. *Nano Lett.* **2009**, *9*, 4479–4483.

36. Lee, Y.; Bae, S.; Jang, H.; Jang, S.; Zhu, S.-E.; Sim, S. H.; Song, Y. I.; Hong, B. H.; Ahn, J.-H. Wafer-Scale Synthesis and Transfer of Graphene Films. *Nano Lett.* **2010**, *10*, 490–493.

37. Cao, H.; Yu, Q.; Jauregui, L. A.; Tian, J.; Wu, W.; Liu, Z.; Jalilian, R.; Benjamin, D. K.; Jiang, Z.; Bao, J. *et al.* Electronic Transport in Chemical Vapor Deposited Graphene Synthesized on Cu: Quantum Hall Effect and Weak Localization. *Appl. Phys. Lett.* **2010**, *96*, 122106.

38. Meyer, J. C.; Geim, A. K.; Katsnelson, M. I.; Novoselov, K. S.; Booth, T. J.; Roth, S. The Structure of Suspended Graphene Sheets. *Nature* **2007**, *446*, 60–63.

39. Ishigami, M.; Chen, J. H.; Cullen, W. G.; Fuhrer, M. S.; Williams, E. D. Atomic Structure of Graphene on SiO_2. *Nano Lett.* **2007**, *7*, 1643–1648.

40. Heinze, J. Ultramicroelectrodes in Electrochemistry. *Angew. Chem. Int. Ed.* **1993**, *32*, 1268–1288.

41. Shoup, D.; Szabo, A. Chronoamperometric Current at Finite Disk Electrodes. *J. Electroanal. Chem.* **1982**, *140*, 237–245.

42. Lavagnini, I.; Antiochia, R.; Magno, F. An Extended Method for the Practical Evaluation of the Standard Rate Constant from Cyclic Voltammetric Data. *Electroanal.* **2004**, *16*, 505–506.

43. Nielson, R. M.; McManis, G. E.; Safford, L. K.; Weaver, M. J. Solvent and Electrolyte Effects on the Kinetics of Ferrocenium-ferrocene Self-exchange. A Reevaluation. *J. Phys. Chem.* **1989**, *93*, 2152–2157.

44. Cline, K. K.; McDermott, M. T.; McCreery, R. L. Anomalously Slow Electron Transfer at Ordered Graphite Electrodes: Influence of Electronic Factors and Reactive Sites. *J. Phys. Chem.* **1994**, *98*, 5314–5319.

45. Patil, A. V.; Beker, A. F.; Wiertz, F. G. M.; Heering, H. A.; Coslovich, G.; Vlijm, R.; Oosterkamp, T. H. Fabrication and Characterization of Polymer Insulated Carbon Nanotube Modified Electrochemical Nanoprobes. *Nanoscale* **2010**, *2*, 734.

46. Niyogi, S.; Hamon, M. A.; Hu, H.; Zhao, B.; Bhowmik, P.; Sen, R.; Itkis, M. E.; Haddon, R. C. Chemistry of Single-Walled Carbon Nanotubes. *Acc. Chem. Res.* **2002**, *35*, 1105–1113.

Chapter 3

Introduction to Scanning Electrochemical Microscopy

3.1 Introduction to Scanning Electrochemical Microscopy

Electrochemical methods such as cyclic voltammetry provide important information about the electrode-solution interface. However, these techniques are generally limited to macroscopic understanding of materials. Electrochemical-microscopy coupled techniques have been employed to investigate the microscopic properties and processes at the electrode-solution interface. Although scanning electron microscopy and transmission electron microscopy could achieve atomic resolution, these techniques are challenging in solution phase experiments due to their rigorous experimental conditions (e.g. high vacuum). These methods are used to identify changes in the surface properties of an electrode before and after an electrochemical experiment. Solution-phase atomic force microscopy and electrochemical scanning tunneling microscopy are used to monitor changes about topographical information concurrently with an electrochemical experiment.[1] In the early 1990's, Bard and co-workers developed the first *in-situ* scan probe technique known as scanning electrochemical microscopy.[2] It probes surface reactions, hence examines the chemical properties of the surface of interest.

Scanning electrochemical microscopy (SECM) involves two independently controlled working electrodes – the probe electrode and the substrate electrode. The position of the probe electrode is controlled by three piezoelectric positioners in the x,

y and z directions. The probe electrode is usually an ultramicroelectrode beveled for SECM experiments. The two electrodes are brought in close proximity and a current, due to the electrochemical reactions, is measured at the probe electrode. The small distance between the probe and substrate electrodes has two possible effects on the current. First, the substrate blocks the diffusion of redox mediators to the probe, thus, a decrease in current is observed. Second, if the substrate electrode has the ability to regenerate the redox mediator, then an increase in current is observed. The effectiveness of the redox mediator regeneration is dependent on the probe-substrate distance (d), the heterogeneous electron transfer rate constant at the substrate electrode (k^0), and the overpotential $(E_s - E^{0\prime})$.[3] This phenomenon is known as the feedback mode of SECM. It is particularly useful in the determination of fast heterogeneous electron transfer reactions and in examination of differential surface reactivity.

SECM in the generation-collection mode can be used to determine the rate of homogeneous reactions (i.e. coupled chemical reactions). This method is very similar to rotating ring disk electrode (RRDE) experiments where the electrochemically active species is generated at one electrode and collected at the other electrode. The generation-collection efficiency is close to unity using SECM, much higher than that of RRDE. The rate of homogeneous reactions is determined by plotting the generation-collection efficiency *versus* the probe-substrate distance. For example, in the synthesis of a Nylon precursor, adiponitrile, the acryltonitrile anion radical decomposes at a very fast rate. Consequently, the reverse reaction cannot be observed

by cyclic voltammetry, even at very fast sweep rates. However, the rate of decomposition can be observed using the generation-collection mode of SECM at very small probe-substrate distances, and was determined to be $6\times10^{7}\mathrm{M}^{-1}\mathrm{s}^{-1}$.[4,5]

In this chapter, we will consider a simple reaction

$$Ox + e^{-} \rightleftarrows Red \qquad (3.1.1)$$

at the probe working electrode. For simplicity, we assume that there are no kinetic complications and that the diffusion coefficients of the oxidized species and the reduced species are the same.

3.2 Experimental

Materials. All materials were used as received without further purification unless otherwise stated.

Eutectic Ga-In alloy. A mixture of 15% gallium metal (99.999%, Alfa Aesar) and 85% indium metal (99.99%, Alpha Aesar) was heated to 50℃ under vacuum in a quartz tube. At the eutectic point, the Ga-In alloy is in the liquid phase as shown in Figure 3.2.1.[6–9]

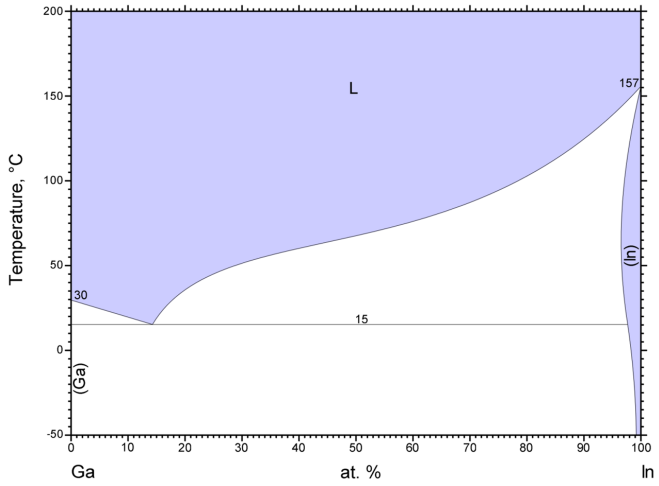

Figure 3.2.1. Binary phase diagram of Ga-In. At the eutectic point, the Ga-In alloy is in the liquid phase.[6–9]

SECM probe electrode. The SECM probe electrode was fabricated by inserting a Pt wire (radius r = 7.5 μm, 99.99%, Goodfellow Corporation, Oakdale, PA) into a soft glass capillary tube with a sealed end. The capillary tube was heated using a pipet puller (Narishige Scientific Instrument Lab, Tokyo, Japan) from the sealed end under vacuum, the best seals were achieved by heating the assembly at a rate of 2 mm/2 min. Back contact was made using a eutectic Ga-In alloy. The probe electrode was sharpened using BuehlerMet II 320 (P400), 400 (P800) and 600 (P1200) sandpapers (Buehler, Lake Bluff, IL) followed by 1 μm alumina on a polishing cloth (Buehler, Lake Bluff, IL). In addition, the 500 nm Pt probe electrodes were polished with 0.3 μm and 0.05 μm alumina on a polishing cloth. After reaching the desired sharpness, the geometric area and the RG ratio (radius of the entire electrode assembly to the radius of the electrochemically active Pt) were determined using optical microscopy,

scanning electron microscopy, cyclic voltammetry and SECM approach curves. Before each measurement, the probe was polished using 1 μm or 0.05 μm alumina on a polishing cloth, rinsed with water, and sonicated in water.

Scanning Electrochemical Microscopy. A bipotentiostat is used to independently control the probe working electrode and the substrate working electrode. As in previous electrochemical experiments, a Ag/AgCl reference electrode and a Au auxiliary electrode were employed. The position of the probe working electrode is controlled by piezoelectric positioners in the x, y and z directions. The minimum step size of the piezoelectric positioners is 0.1 μm. The probe electrode is inserted into a Teflon electrochemical cell that contains the substrate electrode, redox mediator solution, reference electrode and auxiliary electrode as shown in Figure 3.2.2. The tilt of the substrate electrode can be determined by performing line scans in the x and y directions at a probe-substrate distance of a few micrometers. It can be adjusted by turning the knobs below the SECM stage.

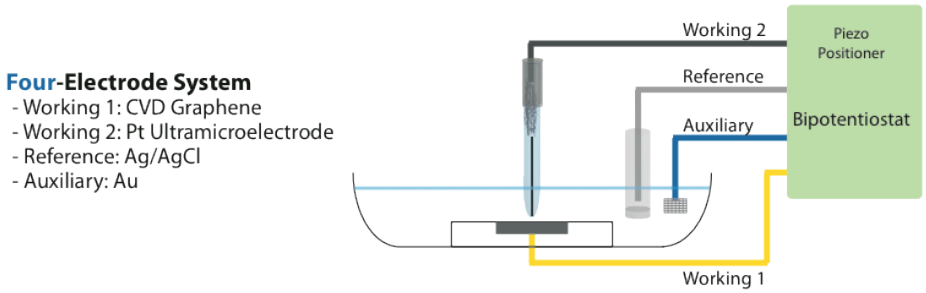

Figure 3.2.2. SECM schematics. SECM involves four electrodes – probe working electrode, substrate working electrode, reference electrode and auxiliary electrode. These electrodes are immersed in a solution of the redox mediator and electrolyte.

3.3 Ultramicroelectrode for Scanning Electrochemical Microscopy

The probe working electrode plays an important role in scanning electrochemical microscopy (SECM) experiments. The feedback current in SECM is the result of the diffusive interactions of a redox mediator between the probe and substrate electrodes. The probe electrode measures the feedback current and defines the spatial resolution of SECM imaging. Furthermore, kinetic information can be extracted from the change in feedback current with probe-substrate distance. In this section, we will discuss the preparation and characterization of the SECM probe working electrodes.

The probe electrode used in SECM is an ultramicroelectrode (UME). In electrochemistry, an UME is defined as an electrode with at least one dimension similar to the dimensions of the diffusion layer. In an UME, the diffusion profile is finite and results in a diffusion length of

$$\delta = \frac{\pi}{4} r \qquad 3.3.1$$

where *r* is the radius of the UME. The current profile has been modeled and reported by Shoup and Szabo as[10,11]

$$i(t) = 4nFD_{Ox} r C_{Ox}^{*} f(\tau) \qquad 3.3.2$$

$$f(\tau) = 0.7854 + 0.8862\tau^{-1/2} + 0.2146e^{-0.7823\tau^{-1/2}} \qquad 3.3.3$$

$$\tau = \frac{4D_{Ox}t}{r^2} \qquad 3.3.4$$

where n is the number of electrons transferred, F is the Faraday constant, C_{Ox}^{*} is the concentration of the redox mediator. Eventually, the current reaches a steady state, and is defined as[12]

$$i_{ss} = i_{T,inf} = 4nFD_{Ox}C_{Ox}^{*}r \qquad 3.3.5$$

This current is also known as the limiting current, $i_{T,inf}$, in SECM. Several UME geometries are available. The disk-in-glass geometry is the most commonly used as SECM probe electrodes due to its ease of preparation and use.

The seemingly simple SECM probe electrode has to be prepared with caution. An error in the feedback current measurement propagates and gives rise to uncertainties in SECM imaging and kinetic measurements. A thin Pt wire is inserted into a soft glass capillary tube with a sealed end. To ensure good adhesion between the glass and the Pt wire, the open end of the capillary tube is connected to a vacuum line to remove air and moisture. The capillary tube containing the thin wire is then heated using a nichrome wire helix, and the soft glass capillary melts around the thin Pt wire. This step should be done slowly and carefully. First, the wire assembly needs to be straight. A slightly bent SECM probe electrode introduces difficulties in the polishing step and gives rise to higher feedback currents. Second, any trapped air bubbles around the Pt wire can introduce uncompensated feedback currents in SECM measurements. The back contact is made with an eutectic Ga-In alloy followed by a Kynar wire. At room temperature, the Ga-In eutectic alloy is liquid, which is very convenient for making electrical contacts between two thin metal wires in a capillary tube. The end of the SECM probe electrode is polished to expose the thin Pt wire. A

cyclic voltammetry experiment is performed to test the electrical contact and to determine the radius of the probe working electrode. By varying the potential, a change in current should be observed. The resulting current profile should resemble that of an UME. The radius of a disk SECM probe electrode, *r*, can be determined by solving Equation 3.3.5. If the electrochemically measured radius is much larger than expected, more Pt could be exposed as a result of a slanted cross section. If a higher capacitance is observed, it is possible that the mediator solution has leaked into the trapped air bubbles around the Pt wire. The electrochemically determined radius can be compared to the value determined using optical microscopy.

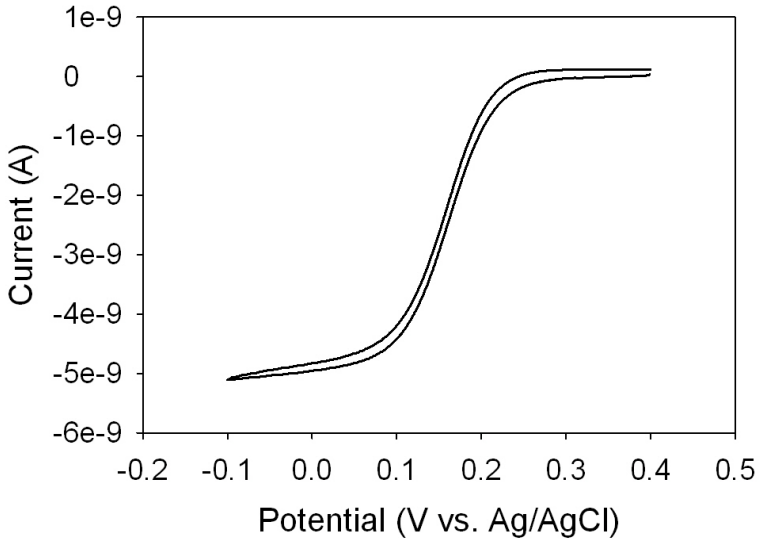

Figure 3.3.1. Cyclic voltammogram of a SECM probe electrode or an ultramicroelectrode (UME). The radius of the disk electrode was determined to be 15 μm.

After the initial characterization, the UME can then be polished using sandpaper and alumina to yield the desired SECM probe electrode. The important parameter of a SECM probe electrode is the ratio between the radius of the entire electrode assembly and the radius of the Pt wire depicted in Figure 3.3.2. This ratio, RG, is also known as the shielding ratio because a thick insulating layer prevents the redox mediator from diffusing to the surface of the electrode. The RG can be determined using a combination of SECM approach curves and scanning electron microscopy. The principles of a SECM approach curve will be discussed in Chapter 3.4. RG can be evaluated electrochemically by measuring the feedback current as the probe-substrate distance decreases.[3,13,14] The approach curve of a conducting substrate can be modeled as

$$I_T(L) = a + \frac{b}{L} + c \times exp(\frac{d}{L}) \qquad 3.3.6$$

where L is the distance between the probe electrode and the substrate electrode normalized to the radius of the probe electrode. $I_T(L)$ is the current normalized to the steady state current $i_{T,inf}$ defined in Equation 3.3.5. Constants a, b, c and d are represented in Table 3.3.1. The approach curve of an insulating substrate can be modeled as

$$I_T(L) = [a + \frac{b}{L} + c \times \exp\left(\frac{d}{L}\right)]^{-1} + e \times \frac{L}{f+L} \qquad 3.3.7$$

Constants a, b, c, d, e and f are presented in Table 3.3.2. The approach curve is strongly dependent on RG because the diffusion of *Ox* is blocked by the insulating layer. In addition, the insulating substrate electrode cannot regenerate the oxidized species, therefore, Red accumulates near the probe electrode. The dependence of

approach curves on RG is shown in Figure 3.3.3. The approach curve to an insulating substrate is known as negative feedback, and is used to evaluate the RG of all SECM probe electrodes. The optimal RG ratio for a SECM probe electrode is between 2 and 10.

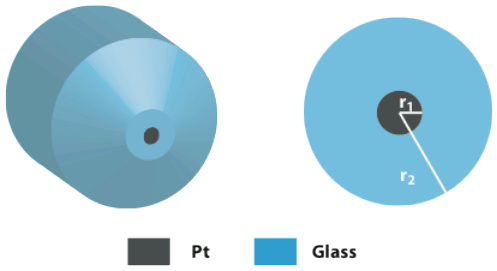

Figure 3.3.2. Schematics of a SECM probe electrode. The radius of the Pt disk is r_1 and the radius of the entire electrode assembly is r_2. The ratio of r_2 and r_1 is the RG of the SECM probe electrode.

RG	a	b	c	d
1.1	0.5882629	0.6007009	0.3872741	-0.869822
1.5	0.6368360	0.6677381	0.3581836	-1.496865
2.0	0.6686604	0.6973984	0.3218171	-1.744691
10	0.7449932	0.7582943	0.2353042	-1.683087

Table 3.3.1. Parameter values for Equation 3.3.6.[3,13,14]

RG	a	b	c	d	e	f
1.1	1.1675162	1.0309985	0.3800855	-1.701797	0.3463761	0.0367416
1.5	1.0035959	0.9294275	0.4022603	-1.788572	0.2832628	0.1401598
2.0	0.7838573	0.877792	0.4248160	-1.743799	0.1638432	0.1993907
10	0.4571825	1.4604238	0.4312735	-2.350667	-0.145437	5.5768952

Table 3.3.2. Parameter values for Equation 3.3.7.[3,13,14]

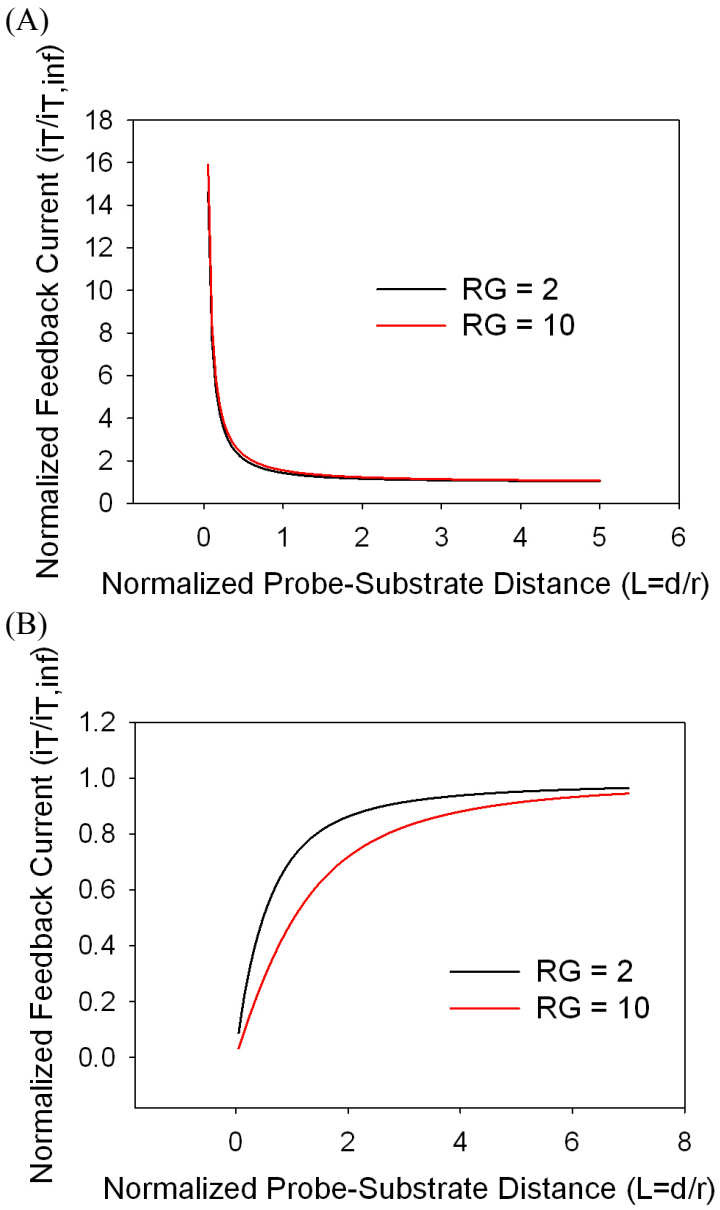

Figure 3.3.3. SECM approach curves. (A) The approach curves are less sensitive to the RG ratio with a conducting substrate (positive approach curve). (B) The approach curves are more sensitive to the RG ratio with an insulating substrate (negative approach curve).

The radius of the probe electrode determines the spatial resolution of SECM. To improve the resolution of SECM, Wollaston wires are employed in the preparation of sub-micrometer-sized SECM probe electrodes. The Pt Wollaston wire in this discussion has a radius of 500 nm, and it was coated with 50-100 μm of Ag. The Pt Wollaston wire was inserted into a soft glass capillary tube. A 10/90 v/v HNO_3/H_2O mixture was drawn by capillary force into the capillary tube to dissolve the Ag coating. Extreme caution is required because the unprotected Pt wire is now very fragile. The same procedures described earlier can be employed to prepare and characterize the sub-micrometer-sized Pt probe electrode. An example of the characterization using scanning electron microscopy, cyclic voltammetry, and SECM approach curve is shown in Figure 3.3.4. The radius of the probe electrode was determined to be 500 nm and 536 nm using SEM and cyclic voltammetry, respectively. An RG of 10 was determined by fitting the negative feedback approach curve to the model described in Equation 3.3.7.

(A)

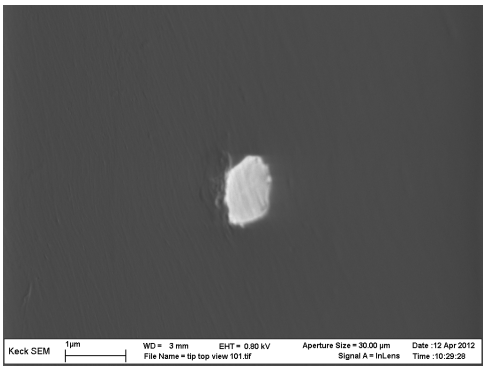

(B)

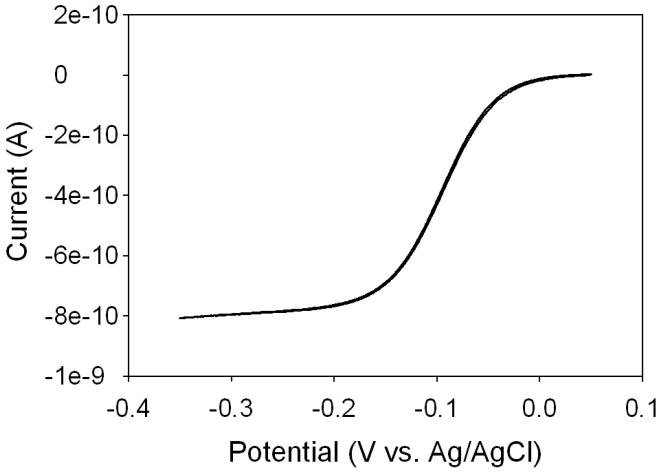

(C)

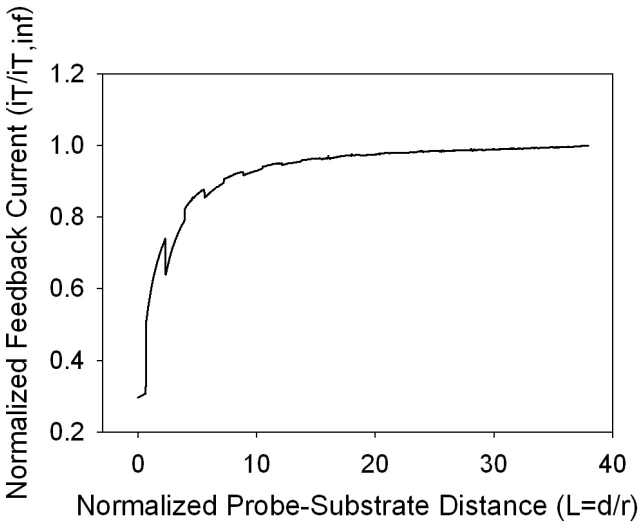

Figure 3.3.4. Characterization of a sub-micrometer Pt probe electrode. (A) and (B) The radius of the probe electrode was determined to be 500 nm and 536 nm using

SEM and cyclic voltammetry, respectively. (C) Fitting the negative feedback approach curve to the model in Equation 3.3.7 yielded an RG of 10.

3.4 Scanning Electrochemical Microscopy in the Feedback Mode

The SECM technique can be employed to measure the heterogeneous electron transfer rate by using what is known, in SECM parlence, as the feedback mode. The use of a bipotentiostat allows the independent control of probe and substrate potentials. In the feedback mode, an SECM probe is held at a potential where a steady state electrochemical reaction of a mediator redox pair *Ox/Red* takes place Figure 4.4.1A. This steady state current, i_{ss} or $i_{T,inf}$, resulting from the reduction of *Ox* to *Red*, for instance, is proportional to the number of electrons in the redox process (n), Faraday's constant (F), the diffusion coefficient of the mediator (D_{Ox}), the concentration of the mediator (C_{Ox}^{*}), and the radius of the ultramicroelectrode (r):

$$i_{ss} = i_{T,inf} = 4nFD_{Ox}C_{Ox}^{*}r \qquad 3.4.1$$

As the probe approaches a conductive substrate (Figure 4.4.1B), *Red,* generated at the probe, reaches the substrate by diffusion. When the substrate is biased at a potential where it can engage in the reaction opposite to that at the probe, a diffusive feedback loop is established which increases the flux of *Ox* towards the SECM probe. This, in turn, increases the feedback current as a function of decreasing the probe-substrate spacing, *d* (positive feedback). In contrast, if the probe approaches an insulating substrate (Figure 4.4.1C), there is no feedback loop operative. In addition, the current decreases as a function of decreasing *d* (negative feedback) because diffusion of *Red*

to the probe is hindered by the substrate. Figure 4.4.2 shows approach curves, which are the current profiles *versus* the normalized distance $L = d/r$, as the probe approaches a conductor (red) and an insulator (blue). The resulting current, also known as the feedback current, provides information about the distance between the probe and substrate working electrodes, and the rate of heterogeneous electron transfer.

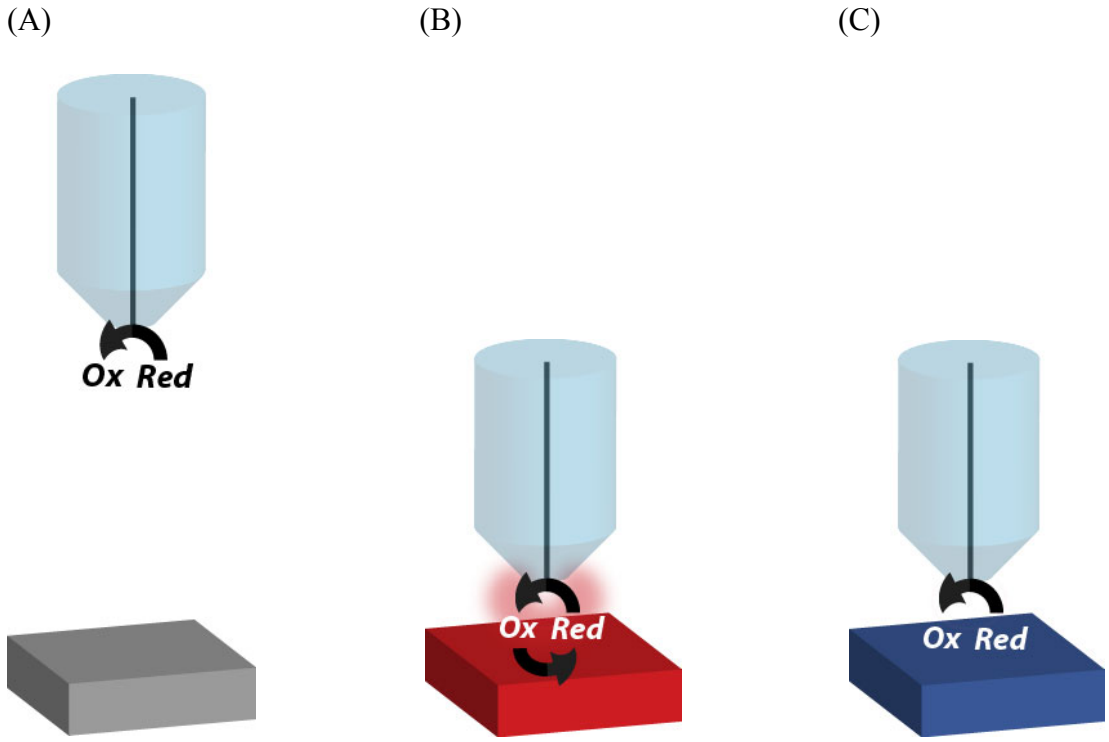

Figure 3.4.1. SECM in the feedback mode. (A) Probe electrode is far from substrate electrode. The feedback current equals the steady state current of the UME. (B) Probe electrode close to a conducting substrate results in positive feedback current. (C) Probe electrode close to an insulating substrate results in negative feedback current.

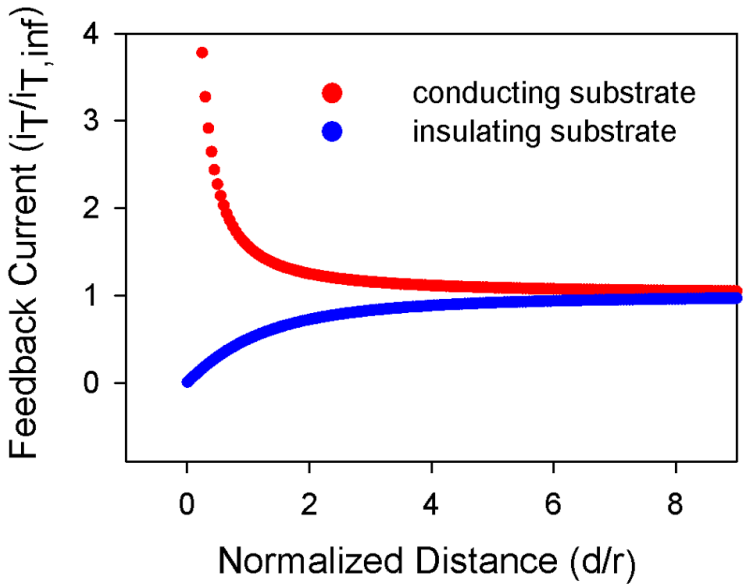

Figure 3.4.2. Feedback current profiles for conducting and insulating substrates. The feedback current is normalized to the steady state current of the UME. The probe-substrate distance is normalized to the radius of the UME.

The feedback current is dependent on the rate of the heterogeneous electron transfer, the substrate potential, and the probe-substrate distance. Assuming the diffusion coefficient of the oxidized species is the same as that of the reduced species, the feedback current at a conducting substrate is[2]

$$i(E_S, L) = \frac{a+b/L+c\times exp(d/L)}{1+\exp\left[nF\left(E_S-E^{0'}\right)/RT\right]} \qquad 3.4.2$$

and the feedback current for at insulating substrate is

$$i(E_S, L) = \frac{[a+b/L+c\times exp(d)/L]^{-1}+eL/(f+L)}{1+\exp\left[nF\left(E_S-E^{0'}\right)/RT\right]} \qquad 3.4.3$$

where E_S is the electrode potential, and $E^{0'}$ is the formal potential. At constant substrate potential and constant probe-substrate distance, an SECM image of the substrate surface can be generated by moving the probe electrode in the x and y directions. At a constant substrate potential, Equations 3.4.2 and 3.4.3 become the positive and negative feedback approach curves, respectively. At a constant probe-substrate distance, electron transfer mechanisms can be determined.[15,16] An example will be discussed in Chapter 4.

Kinetic information can be obtained using cyclic voltammetry and rotating disk electrode experiments, however, the accuracy of the rate of heterogeneous electron transfer can be compromised due to resistance effects. Resistance has less impact on SECM measurements for two reasons. First, according to Equation 3.4.1, the current of a SECM probe electrode should be in the nA range. Assuming a resistance of 1000 Ω, the *iR* drop should be much less than 1 mV. Second, SECM measures the variation in the diffusive flux of *Ox* and *Red* caused by interactions with the substrate, thus, it is not affected by the resistance of either electrode. Furthermore, the size of conventional electrodes limits the kinetics measurement to only moderate value. SECM can be used to measure very fast rate constants, up to 20 cm/s.[17]

UME's are particularly important in fast electron transfer rate constant measurements. In order to determine the rate of electron transfer, the electron transfer has to be much slower than the mass transfer, hence the rate determining step. Mass transport determines the upper accessible rate constant. In UME's, the mass transport is defined as

$$m = \frac{\pi}{2}\frac{D}{r} \qquad 3.4.4$$

where D is the diffusion coefficient of the redox mediator and r is the radius of the probe electrode. In SECM, much higher electron transfer rate constant can be obtained. The mass transport in SECM is faster than in a conventional UME experiment when the probe and substrate electrodes are in close proximity

$$m = \frac{D}{d} \qquad 3.4.5$$

where d is the distance between probe and substrate electrodes. For example, the rate constant accessible with an UME ($r = 1\ \mu m, D = 1{\times}10^{-5}\ cm^2/s$) is 0.1 cm/s, and the rate constant accessible with SECM is 20 cm/s.

The heterogeneous electron transfer rate at the substrate electrode is of particular interest. Early models for rate constants have been developed and solved by Bard and co-workers using alternating direction implicit method (ADI) and multidimensional integral equation (MIE).[2] The feedback currents simulated for various rate constants, probe-substrate distances, and overpotentials are shown in Table 3.4.1.[2] Figure 3.4.3 shows simulated current profiles at an overpotential of 0 V for various dimensionless heterogeneous rate constants, $K = kr/D$, where k is the heterogeneous electron transfer rate constant, r is the radius of the probe electrode, and D is the diffusion coefficient of the mediator.[2] The largest and smallest possible feedback currents at a given distance correspond to complete positive feedback and complete negative feedback, respectively.

	K=25			K=5			K=1			K=0.5			K=0.1			K=0.05			K=0.001		
	E_S-$E^{0\prime}$			E_S-$E^{0\prime}$			E_S-$E^{0\prime}$			E_S-$E^{0\prime}$			E_S-$E^{0\prime}$			E_S-$E^{0\prime}$			E_S-$E^{0\prime}$		
L	**0**	**0.59**	**2.93**	**0**	**1.17**	**4.68**	**0**	**2.34**	**7.8**	**0**	**3.9**	**9.75**	**0**	**7.8**	**11.7**	**0**	**7.8**	**13.7**	**0**	**15.6**	**21.4**
0.1	3.71	4.79	7.66	2.4	3.84	7.38	1	2.42	7.39	0.68	2.62	7.67	0.21	3.25	6.95	0.17	2.07	7.31	0.11	2.04	7.3
0.2	2.12	2.74	4.2	1.66	2.62	4.22	0.93	2.05	4.24	0.72	2.22	4.32	0.24	2.59	4.1	0.19	1.89	4.22	0.14	1.86	4.21
0.5	1.16	1.48	2.2	1.07	1.62	2.26	0.84	1.61	2.28	0.69	1.72	2.29	0.49	1.87	2.25	0.43	1.6	2.27	0.36	1.6	2.27
0.8	0.89	1.14	1.68	0.85	1.3	1.74	0.78	1.39	1.76	0.68	1.49	1.76	0.6	1.58	1.75	0.57	1.44	1.76	0.5	1.44	1.76
1	0.81	1.03	1.51	0.79	1.18	1.57	0.72	1.31	1.58	0.67	1.4	1.58	0.61	1.47	1.57	0.6	1.37	1.58	0.55	1.37	1.58
1.5	0.7	0.89	1.32	0.69	1.03	1.35	0.68	1.18	1.36	0.67	1.27	1.36	0.66	1.31	1.35	0.66	1.26	1.36	0.67	1.26	1.36
2	0.66	0.82	1.21	0.65	0.96	1.24	0.66	1.12	1.25	0.66	1.19	1.25	0.7	1.22	1.25	0.73	1.2	1.25	0.78	1.2	1.25
5	0.63	0.78	1.05	0.64	0.9	1.08	0.65	1.01	1.08	0.66	1.06	1.08	0.74	1.07	1.08	0.79	1.07	1.08	0.92	1.07	1.08

Table 3.4.1. Feedback currents calculated for various dimensionless rate constants (K), normalized tip-substrate distances (L), and overpotentials ($E_S - E^{0\prime}$).[2]

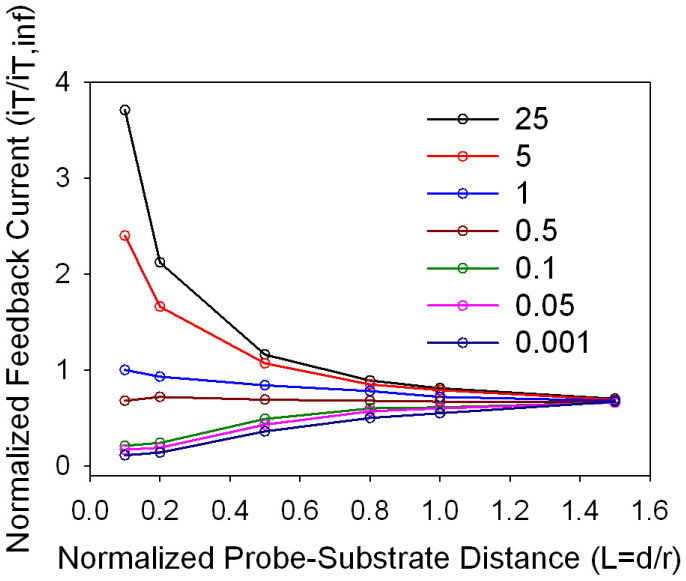

Figure 3.4.3. SECM approach curves at various rate constants.[2] The normalized feedback current is plotted against the normalized probe-substrate distance at various dimensionless rate constants, K. $E_S = E^{0\prime}$

An aspect of the feedback mode of SECM that is important to point out is the behavior of feedback currents under open circuit conditions. A positive feedback

current is observed with a conducting substrate electrode at open circuit. The extent of the feedback current is related to the size of the conducting substrate electrode. When the substrate electrode is large, the *Red* species generated at the probe electrode diffuse to the substrate. The concentration of the *Red* species is very small compared to the *Ox* species near the large conducting substrate electrode surface. According to the Nernst relationship in Equation 3.4.6, the substrate potential will be positive of $E^{0\prime}$.

$$E = E^{0\prime} + \frac{RT}{nF}\ln\left(\frac{C_{Ox}}{C_{Red}}\right) \qquad 3.4.6$$

To compensate for this small non-equilibrium, there will be a small electron transfer at the substrate electrode. When the conducting region of the substrate electrode is small, the *Red* species dominates at the substrate electrode, hence the substrate potential is negative of $E^{0\prime}$. Therefore, there is no electron transfer at the substrate electrode. The current density of the heterogeneous electron transfer can be described by[17]

$$J = -k^0 e^{-\alpha f\left(E_{S,OC}-E^{0\prime}\right)}C_{S,Ox} + k^0 e^{(1-\alpha)f\left(E_{S,OC}-E^{0\prime}\right)}C_{S,Red} \qquad 3.4.7$$

In summary, SECM is particularly advantageous in examining the chemical properties of new surfaces. It provides an alternative method to measure the rate of heterogeneous electron transfer and homogeneous electron transfer using the feedback and generation/collection modes, respectively. Furthermore, it maps the reactivity of surfaces with spatial and temporal resolution.

3.5 References

1. Manne, S.; Hansma, P. K.; Massie, J.; Elings, V. B.; Gewirth, A. A. Atomic-Resolution Electrochemistry with the Atomic Force Microscope: Copper Deposition on Gold. *Science* **1991**, *251*, 183–186.
2. Bard, A. J.; Mirkin, M. V. *Scanning Electrochemical Microscopy*; Marcel Dekker: New York, 2001.
3. Bard, A. J.; Mirkin, M. V.; Unwin, P. R.; Wipf, D. O. Scanning Electrochemical Microscopy. 12. Theory and Experiment of the Feedback Mode with Finite Heterogeneous Electron-transfer Kinetics and Arbitrary Substrate Size. *J. Phys. Chem.* **1992**, *96*, 1861–1868.
4. Zhou, F.; Bard, A. J. Detection of the Electrohydrodimerization Intermediate Acrylonitrile Radical Anion by Scanning Electrochemical Microscopy. *J. Am. Chem. Soc.* **1994**, *116*, 393–394.
5. Zhou, F.; Unwin, P. R.; Bard, A. J. Scanning Electrochemical Microscopy. 16. Study of Second-order Homogeneous Chemical Reactions via the Feedback and Generation/collection Modes. *J. Phys. Chem.* **1992**, *96*, 4917–4924.
6. Anderson, T. J.; Ansara, I. Gallium-Indium. In *Binary Alloy Phase Diagrams*; 1990; Vol. 2, pp. 1811–1814.
7. Okamoto, H. *Phase Diagrams for Binary Alloys*; 2000; Vol. 1.
8. Sharma, B. D.; Donohue, J. A. A Refinement of the Crystal Structure of Gallium. *Z. Kristallogr.* **1962**, *117*, 293–300.

9. Kuznetsova, S. K.; Shkalikova, K. I.; Kuznetsov, G. M. The System Ge-In-Ga. *Inorg. Mater.* **1975**, *11*, 868–870.
10. Amatore, C. Electrochemistry at Ultramicroelectrodes. In *Physical Electrochemistry, Principles, Methods and Applications*; Marcel Dekker: New York, 1995; pp. 131–208.
11. Shoup, D.; Szabo, A. Chronoamperometric Current at Finite Disk Electrodes. *J. Electroanal. Chem.* **1982**, *140*, 237–245.
12. Bard, A. J.; Faulkner, L. R. *Electrochemical Methods*; 2nd ed.; John Wiley & Sons: Hoboken, NJ, 2000.
13. Amphlett, J. L.; Denuault, G. J. Scanning Electrochemical Microscopy (SECM): An Investigation of the Effects of Tip Geometry on Amperometric Tip Response. *J. Phys. Chem. B* **1998**, *102*, 9946–9951.
14. Wei, C.; Bard, A. J.; Mirkin, M. V. Scanning Electrochemical Microscopy. 31. Application of SECM to the Study of Charge Transfer Processes at the Liquid/liquid Interface. *J. Phys. Chem.* **1995**, *99*, 16033–16042.
15. Lefrou, C.; Cornut, R. Analytical Expressions for Quantitative Scanning Electrochemical Microscopy (SECM). *Chem. Phys. Chem.* **2010**, *11*, 547–556.
16. Cornut, R.; Lefrou, C. Studying Permeable Films with Scanning Electrochemical Microscopy (SECM): Quantitative Dtermination of Permeability Parameter. *J. of Electroanal. Chem. and Interf. Electrochem.* **2008**, *623*, 197–203.

17. Wipf, D. O.; Bard, A. J. Scanning Electrochemical Microscopy VII. Effect of Heterogeneous Electron-Transfer Rate at the Substrate on the Tip Feedback Current. *J. Electrochem. Soc.* **1991**, *138*, 469–474.

Chapter 4

Mapping the Reactivity of Chemical Vapor Deposited Graphene Using Scanning Electrochemical Microscopy

4.1 Introduction

In chapter 2, we discussed the investigation of graphene's electrochemical properties using cyclic voltammetry. Cyclic voltammetry gave us a fundamental understanding of graphene's electrochemical properties, however, it provided limited information regarding the local properties of graphene. Graphene, like any material, is not perfect; rather, it can have a high density of grain boundaries and defects. Therefore, it is essential to understand the chemical properties of graphene with spatial resolution.

Graphene defects are generally classified as intrinsic and extrinsic. Intrinsic defects are structural defects, for example, vacancies, carbon adatoms, Stone-Wales defects, and grain boundaries.[1] STM studies have shown an increase in the local density of states at some intrinsic defect sites.[2] Extrinsic defects are the result of the introduction of foreign atoms. Intrinsic defects are prone to attack by foreign atoms to form extrinsic defects due to the strain energy in the carbon-carbon bonds within the structurally unstable intrinsic defects. Computational studies have shown that chemical functional groups can be attached to structural defects.[3,4] For the purpose of the discussions here, all functional groups other than 6-carbon-sp^2-hybridized structures are treated as defects. Early studies by McCreery and co-workers have

shown that surface defects play an important role in the electrochemical activity of highly oriented pyrolytic graphite (HOPG) electrodes.[5–12] On an HOPG surface, a 0.1% increase in defects could result in an increase in the electron charge transfer kinetics of three orders of magnitude.[10] These defects are usually composed of phenol, carbonyl, carboxylic acid, lactone, and quinone functional groups.[13] While there have been many computational reports about the reactivity of graphene defects,[14–17] there is a general lack of experimental verification. There have been some examples of electrochemical studies in which the area-averaged characteristics of single layer graphene are modified by oxygenated groups,[18] the insertion of nitrogen,[19] or graphitic islands.[20]

Here, we discuss spatially resolved measurements of the electrochemical reactivity of graphene and its defects using scanning electrochemical microscopy (SECM). SECM is a powerful tool that can image the surface of a substrate through electrochemical means. It is useful for the determination of heterogeneous electron charge transfer kinetics with spatial resolution and for the fabrication of high-resolution patterns on metal and semiconducting surfaces.[21–24] Studies of the electrochemical activity of carbon nanostructures, where high-accuracy measurement of electron transfer rates was required, have been done using SECM.[25–27]

Defects on graphene can be generated during growth, by ion or electron irradiation, or by chemical oxidation.[1] We introduced defects into our samples by deliberate mechanical damage and by chemical oxidation. The electrochemical reactivity of these graphene defect sites was investigated using the feedback mode of

SECM. We examined the passivation of defects on graphene using the electropolymerization of *o*-phenylenediamne (OPD) and studied the mechanism of OPD growth. Electropolymerization of OPD has been widely used in photovoltaic cells, anticorrosion coatings, and biosensors. OPD polymerization has also been used for the selective passivation of imperfections of n-WSe_2 and n-$MoSe_2$ photoelectrodes.[28] The oligomeric structures resulting from OPD electropolymerization have been analyzed previously using mass spectrometry.[29]

4.2 Experimental

Materials. All chemicals were used as received without further purification unless otherwise stated. The DI water used in these experiments was purified with a Millipore water purification system. Potassium chloride (KCl), sodium sulfate (Na_2SO_4), and 0.2 M phosphate buffer (PBS, pH 6.8) were used as electrolyte and were purchased from Mallinckrodt Chemicals. *o*-Phenylenediamine (OPD, 99.5%, Sigma-Aldrich) was recrystallized twice from ethyl acetate.

CVD graphene. Monolayer graphene was grown by chemical vapor deposition on Cu foil (0.025mm thick, 1×1 cm^2, 99.8%, Alfa Aesar). The copper foils were treated with acetone (10 s, AR, Mallinckrodt Chemicals), water (DI), glacial acetic acid (10 min., Mallinckrodt Chemicals), water (DI), acetone (10 s), and isopropanol (10 s, BDH) before growth. They were then loaded into a quartz tube in a tube furnace. The system was pumped to 8.0×10^{-5} torr. After reaching the base pressure, 300 sccm of H_2 (99.999%, Airgas) was flowed and H_2 was present for the entire

growth process. The system was then heated at 1000 ℃ for 10 min and the graphene was grown under the flow of 157.5 sccm of CH_4 (99.999%, Airgas) for 13 min. After removal from the furnace, the graphene was transferred from the Cu foil to an oxidized Si substrate. For support during the transfer, 8% PMMA in anisole (Nano^{TM} 495 PMMA series resists in anisole, MicroChem) was first spin coated on top of the graphene at 4000 RPM for 60 sec. The Cu-graphene-PMMA multilayer was then floated on a ferric chloride etch solution (CE-100 grade, Transene Company) to remove the Cu. The graphene-PMMA membrane was transferred into fresh DI water 6 times to remove residual impurities. Finally, the membrane was scooped out of DI water with a piece of plasma-cleaned Si/SiO_2 substrate (300 nm SiO_2, prime grade, Silicon Quest International). The chip was blow-dried using N_2 (99.999%, Airgas). To remove the PMMA, the chip was soaked in anisole (2 h, 99.7%, Sigma-Aldrich), dichloromethane (Mallinckrodt Chemicals) and acetone mixture (1:1, 4 h), and isopropanol (2 h). The quality of the graphene was characterized using a Renishaw InVia Confocal Raman microscope (Renishaw, Gloucestershire, UK) using a 488nm laser. The average grain size of the graphene is approximately 0.25-1.7μm.[30]

Electrical contact to graphene. We used a CVC SC4500 electron-gun evaporator to deposit 20 Å of Ti (99.995%, Kurt J. Lesker Company) onto one end of the single-layer graphene as an adhesion layer followed by 1000 Å of Au (99.999%, Kurt J. Lesker Company).

Electrochemistry. SECM and electrochemical measurements were carried out using a CHI 900 SECM/potentiostat (CH Instruments, Austin, TX). A homemade

Teflon SECM cell was used. A monolayer CVD graphene electrode and a Pt ultramicroelectrode were employed as the substrate and probe electrodes, respectively. Fresh monolayer CVD graphene electrodes were prepared for each experiment. The Pt ultramicroelectrode was polished using 1μm alumina on microcloth pads (Buehler) and sonicated in water before each use. A Ag/AgCl saturated KCl reference electrode, isolated from the working electrolyte solution through an agar/0.1 M potassium nitrate bridge to prevent excessive chloride or silver contamination, and a Au wire counter electrode were used. In the mediator selection experiment, 1 mM of hydroxymethylferrocene (FcMeOH, Alfa Aesar) with 0.1 M KCl in water and 2 mM potassium ferricyanide ($K_3Fe(CN)_6$, Fisher Chemicals) in phosphate buffer were employed. Mechanical defects were induced using a glass tip approximately 20 μm in radius. Chemical defects were created using microdroplets (ranging from 50 to 100 μm in diameter) of 10 mM NaOCl in water (final pH ~ 8, diluted from a concentrated 5.25% solution, BP) dispensed by a piezoelectric micro-dispenser with an orifice 30 μm in diameter (Microfab Inc. Plano, Texas). OPD (13.7 mM) and Na_2SO_4 (0.1 M) were prepared in borate buffer (pH 8.1) and the solutions were stored in a dark environment. Electropolymerization of OPD on graphene was carried out by potential cycling between 0 and +0.8 V *vs*. Ag/AgCl at 0.1 V/s for the desired number of cycles. In the carboxylic acid-aminoferrocene coupling reaction, a solution of 2 mM of aminoferrocene (96%, TCI America) and 4 mM of N, N'-dicyclohexylcarbodiimide (DCC, 99%, Sigma-Aldrich) in N, N-dimethylformamide (DMF, Mallinckrodt

Chemicals) was poured into the electrochemical cell containing the graphene substrate electrode and reacted overnight.

All approach curves and tip positioning procedures were analyzed using reported expressions.[31,32] For feedback imaging experiments, potassium ferricyanide (between 1 and 2 mM) in 0.2 M pH 7 phosphate buffer was used. The SECM tip, E_T = -0.1 V *vs*. Ag/AgCl, was positioned by a negative feedback-like approach curve obtained with the substrate at open circuit. During imaging, the substrate electrodes were biased to E_S = 0.8 V *vs*. Ag/AgCl unless noted otherwise. For feedback experiments after deposition of OPD, hydroxymethylferrocene (~1 mM) in 0.1 M potassium chloride was used. The SECM tip, E_T = 0.4 V *vs*. Ag/AgCl, was positioned by a positive feedback-like approach curve obtained with the substrate at an appropriate potential. In all OPD deposition experiments, care must be taken not to immerse the Pt tip into the deposition solution, as it was observed that even in the absence of tip biasing, the OPD solution would poison the Pt tip so that distorted voltammograms, of otherwise reversible mediators, were observed. For this reason, between each round of OPD deposition and SECM imaging the electrochemical cell was rinsed, at least 10 times, with DI water and the salt bridge was replaced.

4.3 Selection of Redox Mediators

The choice of mediator is important if one is to observe kinetic differences between pristine and defective areas on the graphene surface. We examined two common mediators, hydroxymethylferrocene (FcMeOH) and potassium ferricyanide

[$K_3Fe(CN)_6$]. FcMeOH has a standard potential of $E^0 = 0.21$ V *vs*. Ag/AgCl, thus, the Pt tip electrode was held at a potential of $E_T = 0.5$ V *vs*. Ag/AgCl to ensure complete diffusion-limited oxidation of the Fe(II) species originally present in solution to Fe(III). The graphene substrate electrode was biased at $E_S = -0.2$ V *vs*. Ag/AgCl to ensure complete reduction of the species generated at the tip. Positive feedback was observed when the tip approached the graphene using FcMeOH as mediator (Figure 4.3.1A and 4.3.1B). The tip was scanned over the graphene surface at a constant tip-substrate separation of 6 μm to generate a feedback image of the substrate with an approximate resolution of the radius of the tip (~7.5 μm). Nanometer-scale topographic features have no influence on the response because these features are three orders of magnitude smaller than the distance between the tip and the substrate. Thus, only changes in the heterogeneous electron transfer kinetics at the substrate can give rise to changes in the feedback current. The heterogeneous electron transfer rate for FcMeOH at a CVD graphene substrate is very fast, $k^0 = 4.2 \times 10^{-2}$ cm/s, as discussed earlier in chapter 2,[33] thus approaching complete positive feedback under conditions described above. In this case, small changes in the kinetics between defects and more pristine areas of graphene cannot be distinguished due to the lack of contrast arising from the fast interfacial kinetics. Occasional voids in the graphene, which exposed the underlying Si/SiO_2 wafer, were created by damaging the graphene surface with a glass tip. This produced insulating areas in the substrate that disabled the diffusive feedback loop.

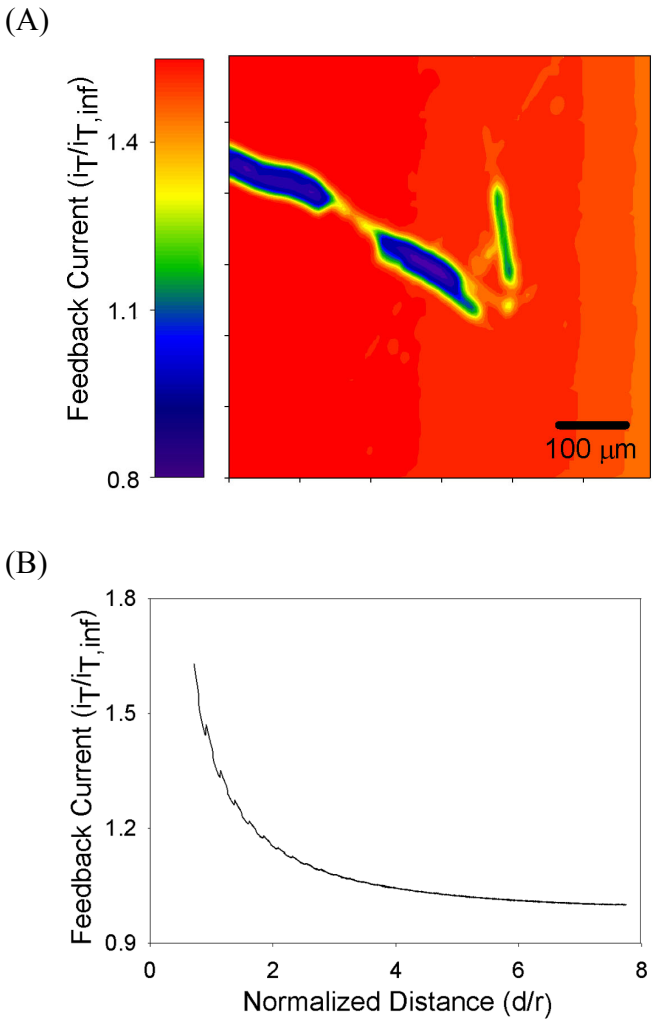

Figure 4.3.1. SECM image of monolayer graphene using FcMeOH as the redox mediator. (A) Positive feedback SECM image showing graphene in red and exposed Si/SiO_2 in blue with 1 mM FcMeOH as mediator. The graphene electrode was biased at -0.2 V *vs*. Ag/AgCl and the tip was biased at 0.5 V *vs*. Ag/AgCl. (B) Positive feedback current profile as the tip approaches a pristine area of the graphene surface.

Imaging was also performed using $K_3Fe(CN)_6$ as a mediator, which has a standard potential of $E^0 = 0.16$ V *vs*. Ag/AgCl (Figure 4.3.2A). $K_3Fe(CN)_6$ has been reported to be highly sensitive to defects on HOPG electrodes with standard heterogeneous rate constants ranging from 8×10^{-7} to 4.1×10^{-2} cm/s.[9,10] The much slower kinetics, using $K_3Fe(CN)_6$, resulted in intermediate to negative feedback currents (Figure 4.3.2B). In our measurements with $K_3Fe(CN)_6$, the tip was held at a potential of $E_T = -0.1$ V *vs*. Ag/AgCl to ensure complete reduction of the Fe(III) species originally present in solution to Fe(II), and the graphene electrode was biased at various potentials: $E_S = 0.4$, 0.6 and 0.8 V *vs*. Ag/AgCl to regenerate the Fe(III) species. Larger variations (and thus higher contrast) in the electrochemical activity of the graphene surface were observed at all potentials using this mediator compared to FcMeOH which has a much narrower range of heterogeneous kinetics. At 0.8 V *vs*. Ag/AgCl, a set of clear, localized defects was observed with size scales ranging up to hundreds of microns, providing a strong contrast with respect to a more pristine graphene surface. We propose that different defects may have different chemical or physical identities, leading to a wide range of electron transfer kinetics using $K_3Fe(CN)_6$ as mediator. It is important to note that topographic features cannot be observed in this case. Topological features resulting in a smaller *d* would still give the same negative approach curve followed by a current overload when the tip crashes into these features. This current would be at least a few orders of magnitude higher compared to the usual SECM feedback current. We used $K_3Fe(CN)_6$ as mediator with the graphene electrode biased at $E_S = 0.8$ V *vs*. Ag/AgCl because under these

conditions, the SECM feedback current depends strongly on the kinetics of the graphene imperfections/defects. In addition, oxidative damage to the graphene surface is unlikely at this potential.

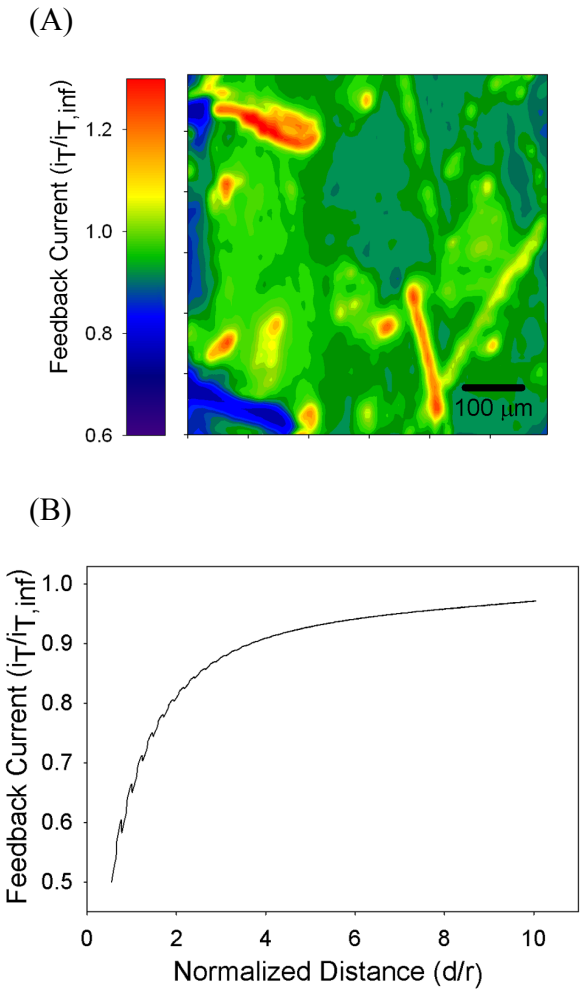

Figure 4.3.2. SECM images of monolayer graphene using $K_3Fe(CN)_6$ as the redox mediator. (A) An intermediate-negative feedback SECM image showing the bulk graphene in green/blue and defects of higher activity in orange with 2 mM $K_3Fe(CN)_6$ as the mediator. The graphene electrode was biased at 0.8 V *vs*. Ag/AgCl and the tip was biased at -0.1 V *vs*. Ag/AgCl. (B) Intermediate-negative feedback current profile

as the tip approaches a pristine area of the graphene surface. The large features in the SECM images coincide with regions in which graphene was deliberately removed by scratching the surface with a glass tip.

4.4 Mapping the Reactivity of Chemical Vapor Deposited Graphene Using Scanning Electrochemical Microscopy

To study the influence of graphene imperfections in a more controlled manner, we created mechanically- and chemically-induced defects. Optical microscopy images before and after the deliberate creation of defects are shown in Figure 4.4.1. Mechanical defects were created by damaging the graphene surface with a glass tip using a piezoelectric positioner. Figure 4.4.2A shows the schematic of a mechanical defect – a hole in the graphene. The defect and its surrounding areas were examined using SECM as shown in Figure 4.4.2B. The edges of the defect show a much higher feedback current than the surface of the graphene far from the defect. The feedback currents correspond to k_f values between ~4.5×10^{-5} cm/s for bulk graphene and ~2.6×10^{-4} cm/s for defect sites (Figure 4.4.2C). This result indicates that the defect sites have higher electron transfer kinetics by approximately an order of magnitude, and thus, are more reactive than the overall surface of graphene. This is in agreement with previous computational and STM results.[2] The higher activities observed on mechanical defects could be due to the exposed edges in the graphene surface and perhaps to the chemical oxidation of sp^2 carbons in an aqueous environment. The higher activity of defects on HOPG has been observed and studied thoroughly.[5–12]

This result could also explain the higher heterogeneous electron transfer kinetics reported for graphene paste which is smaller in size and therefore high in edge density when compared to the individual monolayer graphene used in this study. Furthermore, it is difficult to distinguish the contributions to the rate of the underlying substrates typically used in the graphene paste experiments. In our experiments, the underlying substrate is Si/SiO_2 so no such ambiguity is present.

(A)

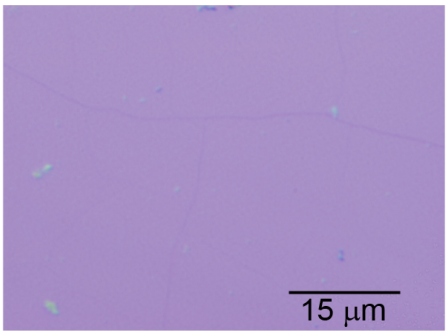

(B)

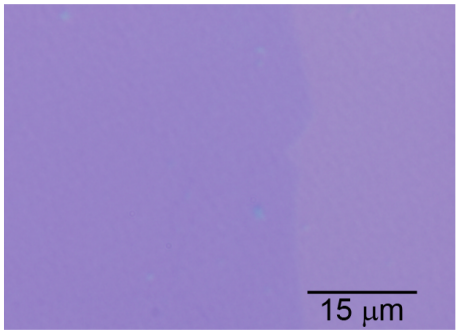

(C)

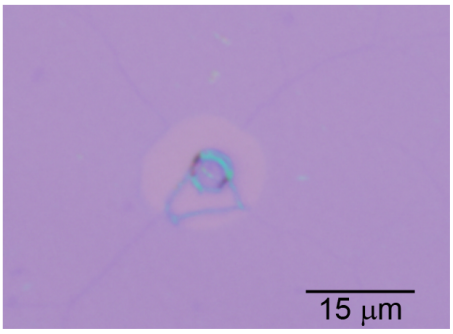

Figure 4.4.1. Optical microscopy images of graphene. (A) CVD graphene on Si/SiO_2 before any deliberate creation of defects. (B) Mechanically-induced defect edge. The dark purple is graphene and the light purple is Si/SiO_2. (C) Chemically-induced defect. No obvious contamination was observed around the edges of the defect sites.

(A)

(B)

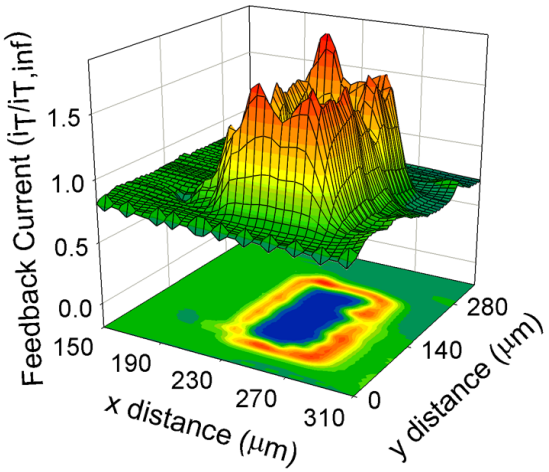

(C)

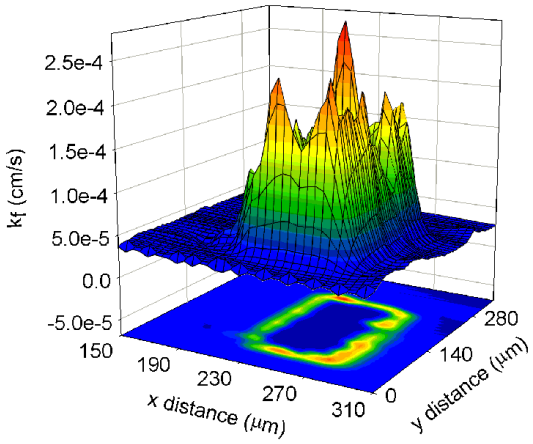

Figure 4.4.2. SECM images of a mechanically-induced defect. (A) Schematic of a mechanically-induced defect (not to scale) on the graphene electrode. (B) SECM image of graphene with mechanically-induced defect. (C) SECM image of a mechanically-induced defect with the z-axis as the forward rate of heterogeneous

electron transfer, k_f. It shows that sites with a large concentration of defects are ~1 order of magnitude faster when compared to more pristine graphene surfaces towards electrochemical reactions. SECM tip: Pt radius = 7.5 μm biased at -0.1 V *vs*. Ag/AgCl; graphene electrode: biased at 0.8 V *vs*. Ag/AgCl. Mediator: 2 mM $K_3Fe(CN)_6$; electrolyte: 0.2 M PBS.

4.5 Electropolymerization and Characterization of *o*-Phenylenediamine on Graphene

We investigated whether the enhanced electrochemical reactivity of the mechanically-induced defects could be passivated by selective electropolymerization of *o*-phenylenediamine (OPD), following the work of Bard and co-workers on the selective passivation of imperfections in n-WSe_2 and n-$MoSe_2$ semiconductor electrodes.[28] We immersed the graphene electrode in a solution of OPD and swept its potential between 0 and 0.8 V *vs*. Ag/AgCl as shown in Figure 4.5.1. After one cycle of potential sweep, we exchanged the OPD solution with a fresh $K_3Fe(CN)_6$ solution for SECM imaging. A small increase in the feedback current was often observed after the first cycle. This could be due to the competitive desorption of impurities on the graphene that previously could have partially blocked electron transfer or the initial formation of an electrochemically active species on the graphene electrode surface. However, after an additional three potential sweeps, we observed a dramatic change in the activity of the active edges, as observed in Figure 4.5.2B, indicating that the electrochemically inactive OPD polymer passivated the reactivity of graphene defects.

Note, compared to Figure 4.5.2A, the overall electrochemical activity of the graphene electrode decreased slightly. This small decrease could be due to either the passivation of widely-distributed small defects on the graphene surface by the electropolymerization process or to the electropolymerization of OPD on the pristine surface. Additional experiments suggest the presence of widely-distributed defects on graphene, and it is most likely that OPD will attack these defect sites before the pristine areas. The carefully controlled electropolymerization of OPD is able to effectively passivate the active mechanically-generated defects while causing little impact on the electrochemical activity of the bulk graphene surface. Upon further electropolymerization of OPD, an insulating film started to form on the graphene surface, diminishing the activity of the entire graphene surface. The possible mechanism of film formation and film thickness will be discussed in a later section.

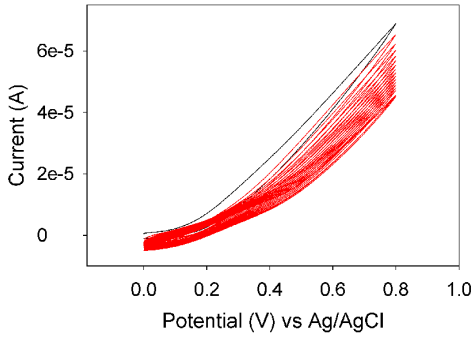

Figure 4.5.1. Electropolymerization of OPD on graphene. First cycle is in black; as the graphene electrode was swept between 0 and 0.8V, the activity of the electrode decreased. Working electrode: monolayer CVD graphene; reference electrode: Ag/AgCl; counter electrode: Au. The cyclic voltammetry was done in a solution of 13.7 mM OPD, 0.1 M Na_2SO_4 and borate buffer (pH 8.1).

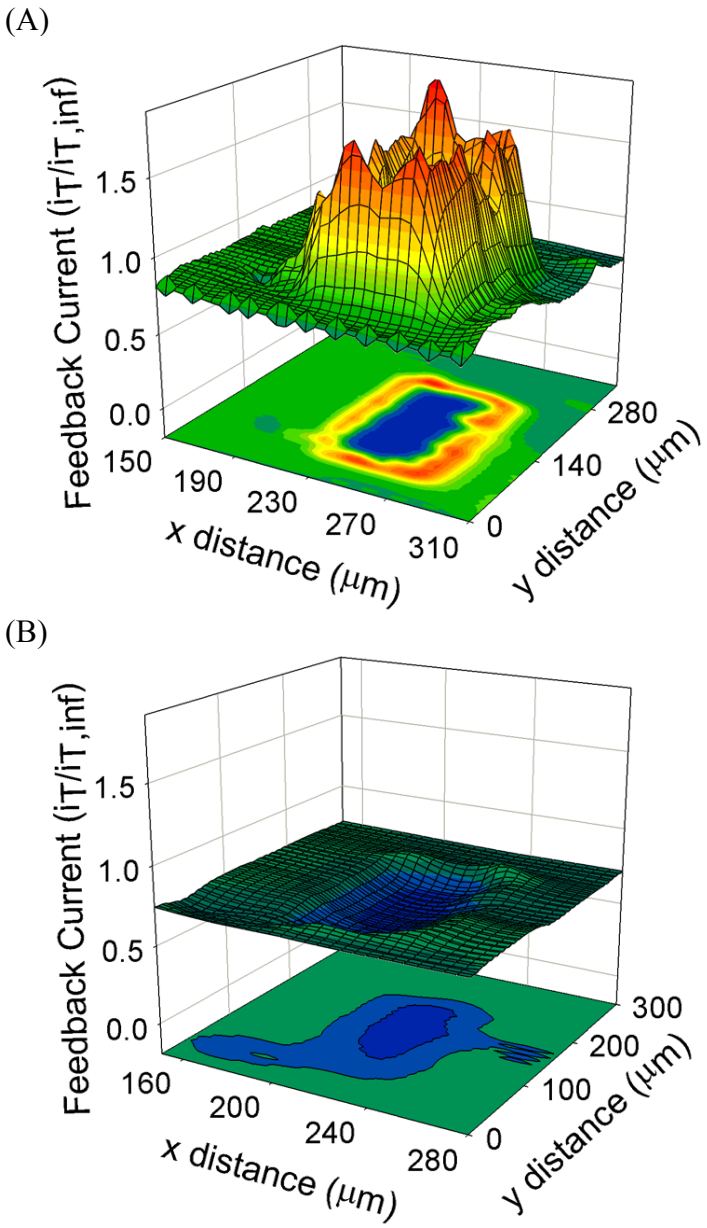

Figure 4.5.2. SECM images of a mechanically-induced defect and its passivation. (A) SECM image of graphene with mechanically-induced defect. (B) Mechanically-induced defect after 4 cycles of OPD electropolymerization. SECM tip: Pt radius = 7.5 µm biased at -0.1 V *vs*. Ag/AgCl; graphene electrode: biased at 0.8 V *vs*. Ag/AgCl. Mediator: 2 mM $K_3Fe(CN)_6$; electrolyte: 0.2 M PBS.

The reactivity of chemically-induced defects was also examined. Arrays of small droplets of an oxidizer, NaOCl, were dispensed onto the graphene electrode using a piezoelectric dispenser. The sample was heated to 100^{o}C for 30 min. to accelerate the oxidative etching process. The graphene was then rinsed with copious amounts of water to remove any remaining NaOCl residues. Small holes of ~30 × 30 μm^2 can be observed at the droplet site as shown in Figure 4.5.3A. We initially observed a higher feedback current around the edges of the defect and a slight increase in current after one cycle of OPD deposition as seen with the mechanically-induced defects. Upon sweeping the potential for an additional three cycles, there was a significant decrease in the activity of the defect sites (Figure 4.5.3B). Finally with further cycling, an insulating film of OPD developed. A smaller contrast in activity between the defect sites and the overall graphene, compared to that of mechanical defects, suggests possible differences in the chemical functionalization or defect concentrations. A smaller passivating effect is observed in the chemically-induced defect compared to the mechanically-induced defects with the same number of polymerization cycles. This discrepancy can be explained by the variation in reactivity towards OPD polymerization of the two types of defects. We also observe differences between chemically-induced and mechanically-induced defects in Raman mapping experiments of the D band intensity (Figure 4.5.4), similar to previous studies by the groups of Saito and Brus.[34,35] Despite the possible differences, OPD electropolymerization passivated the defect sites efficiently after a few cycles, while

retaining the pre-existing activity of the bulk graphene electrode as was similarly observed in the case of mechanically-induced damage.

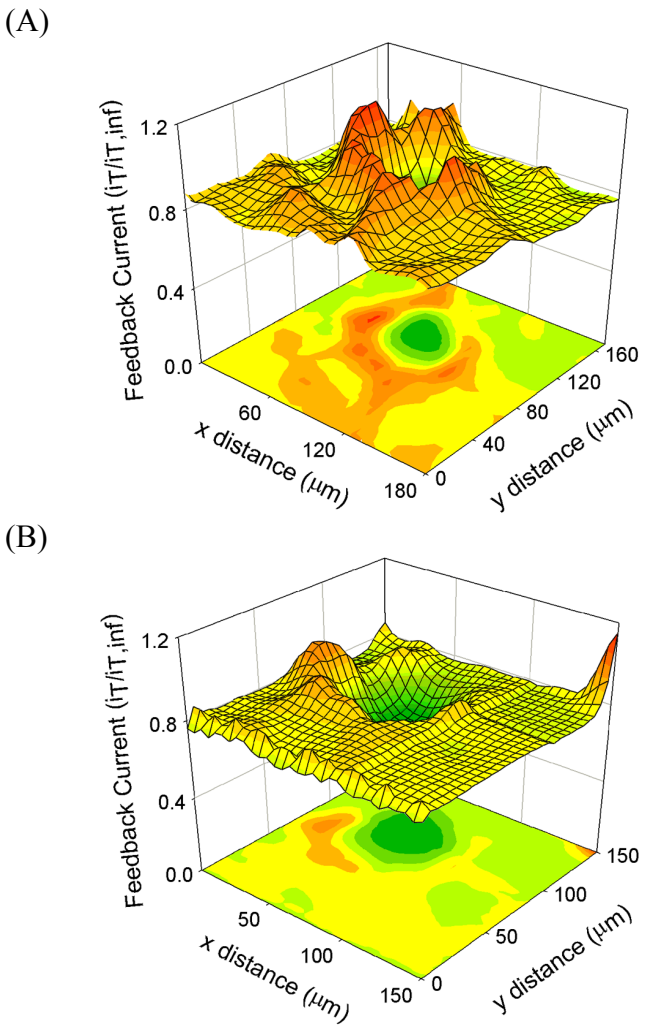

Figure 4.5.3. SECM images of a chemically-induced defect and its passivation. (A) Chemically-induced defect using NaOCl. (B) Chemically-induced defect after a total of four cycles of OPD electropolymerization. Chemically-induced defects were induced by droplets of 10 mM NaOCl. SECM tip: Pt radius = 7.5 μm biased at -0.1 V *vs*. Ag/AgCl; graphene electrode: biased at 0.8 V *vs*. Ag/AgCl. Mediator: 2 mM $K_3Fe(CN)_6$; electrolyte: 0.2 M PBS.

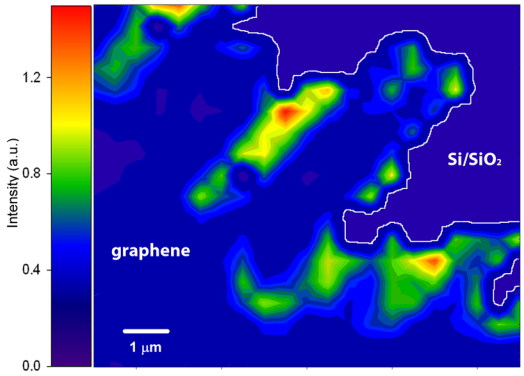

Figure 4.5.4. Raman mapping image. The edge of a chemically-induced defect has higher I_D/I_G ratio compare to the rest of the graphene. The analysis was done according to references 34 and 35. The edge of the graphene is outlined in white. The z-axis is the ratio of I_D/I_G.

As noted above, while the electropolymerization of OPD successfully passivated the mechanically- and chemically-induced defects, a concomitant decrease in the feedback current of the bulk graphene surface was also observed after many cycles. We believe that CVD graphene exhibits many defects and can be passivated by the electropolymerization process, hence the lower feedback current. Because of the instability of structural defects due to strain energies, they are prone to chemical attack by foreign atoms in the environment – most likely oxygen-containing groups. Carboxylic acid functionalized defects are among the most abundant chemical functional groups on carbon materials and can readily react with amino-functionalized groups using an activator such as dicyclohexylcarbodiimide (DCC). As a test, graphene was reacted with an amino-functionalized ferrocene in the presence of DCC.

Figures 4.5.5A and 4.5.5B show images of a graphene "coastline" (left portion is graphene, right portion is Si/SiO_2) before and after the ferrocene functionalization. A comparison of these images shows a dramatic difference in feedback current. The increase in activity is due to the higher electron transfer kinetics of the redox-active ferrocene pendant. The homogeneity indicates that carboxylic acid-functionalized defects exist all over the graphene surface and are functionalized by the ferrocene derivative. This experiment explains why there is a decrease in feedback current over the entire CVD graphene electrode after four cycles of OPD electropolymerization. As shown in Figure 4.5.6, this effect was not observed in the absence of the amino-functionalized ferrocene in the same reaction mixture.

(A)

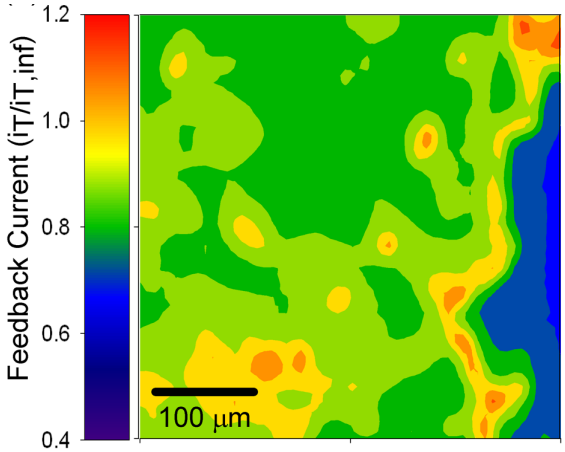

(B)

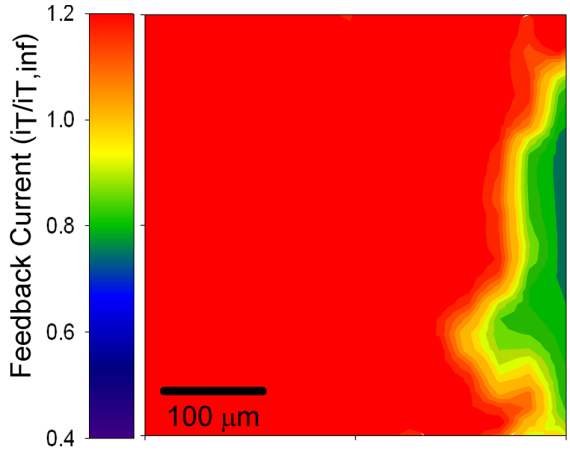

Figure 4.5.5. SECM images of aminoferrocene functionalization experiments on graphene. (A) Bare graphene (green, yellow, red) and Si/SiO_2 substrate (blue). (B) Graphene after aminoferrocene functionalization showing a significant increase in feedback current (red). SECM tip: Pt radius = 7.5 μm biased at -0.1 V *vs*. Ag/AgCl; graphene electrode: biased at 0.8 V *vs*. Ag/AgCl. Mediator: 2 mM $K_3Fe(CN)_6$; electrolyte: 0.2 M PBS.

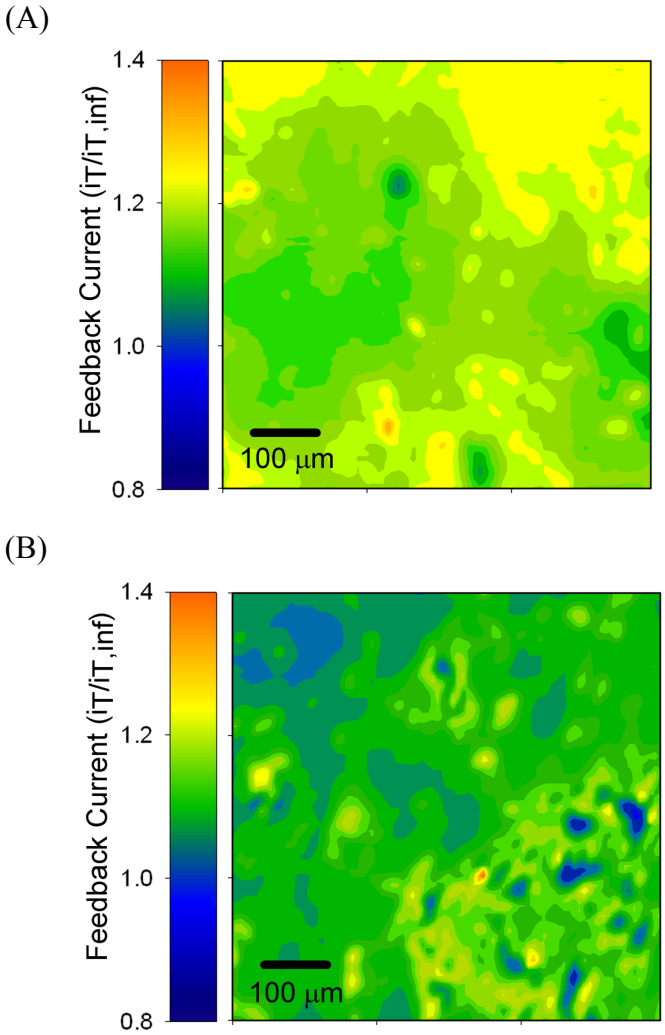

Figure 4.5.6. Control for the aminoferrocene functionalization experiment. (A) and (B) SECM images before and after, in the absence of aminoferrocene under the same conditions as Figure 4.5.5. SECM tip: Pt radius = 7.5 μm biased at -0.1 V *vs*. Ag/AgCl; graphene electrode: biased at 0.8 V *vs*. Ag/AgCl. Mediator: 2 mM $K_3Fe(CN)_6$; electrolyte: 0.2 M PBS.

The electropolymerization of *o*-phenylenediamine (OPD) has been previously studied intensively because of its application in electronics and biosensors.[28,36,37] A thin film of OPD started to grow on graphene after sweeping the potential for more than 10 cycles. The formation of this film could possibly serve as a protective or insulating layer in graphene applications, for instance, selective protection of graphene from aggressive solvents and prevention of defect-induced oxidative damage to graphene. To explore the properties of the OPD polymer film, we performed experiments with FcMeOH as the mediator. As mentioned earlier, in a previous study, we had determined the rate constant of FcMeOH at a CVD graphene electrode surface to be $k^0 = 4.2 \times 10^{-2}$ cm/s.[33] FcMeOH is an ideal candidate for probing the barrier properties of the OPD polymer because it shows nearly diffusion limited substrate kinetics – almost complete positive feedback as shown in Figure 4.5.7A. At the same time, it has slow enough heterogeneous kinetics that the presence of a thin blocking layer at the electrode would affect the feedback currents in SECM approach curve measurements (Figure 4.5.7).

(A)

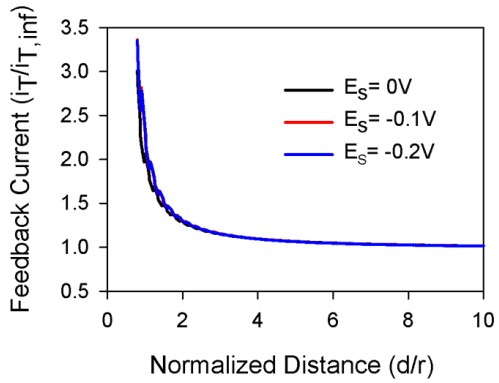

(B)

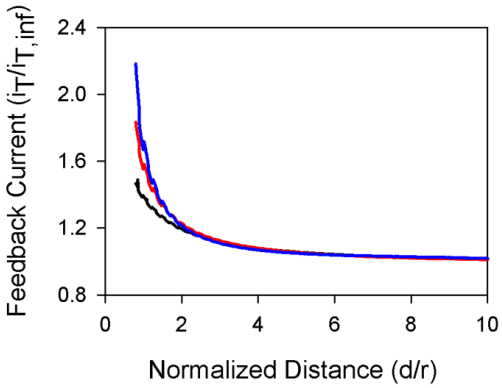

(C)

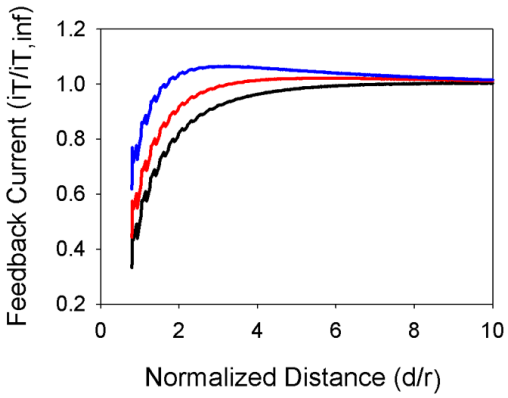

Figure 4.5.7. Approach curves showing the feedback responses with different amounts of OPD at various potentials. Figure (A) and (B) show that when there is no OPD or after 3 cycles of OPD electropolymerization, the electron transfer is fast, as indicated

by the positive feedback currents. (C) With further electropolymerization (38 cycles), a film of OPD blocks the electron transfer resulting in an insulating response. SECM tip: Pt radius = 7.5 μm biased at 0.5 V *vs*. Ag/AgCl; graphene electrode: biased at 0, -0.1 and -0.2 V *vs*. Ag/AgCl. Mediator: 1 mM FcMeOH; electrolyte: 0.1 M KCl.

Two possible electron transfer mechanisms through the OPD film can be proposed and studied using SECM. The first one treats the OPD film as an insulating film for which electron tunneling through the film controls the rate of electrochemical reaction (Figure 4.5.8A).[38,39] In this case, the apparent rate of electron transfer can be described by

$$k_{app} = k_f e^{-\beta x} \qquad 4.5.1$$

where k_f is the rate of electron transfer of the forward reaction in the absence of the insulating layer, β is the tunneling constant which is controlled by the nature of the polymer chain and ranges from 0.4 for π-conjugated molecules to 1.2 $Å^{-1}$ for saturated chains, and x is the thickness of the film.[40] From the Butler-Volmer formalism, the kinetics of the forward reaction depends on the difference between the substrate potential (E_s) and the standard potential ($E^{0\prime}$),[21] that is, the effective overpotential:

$$k_f = k^0 e^{-\alpha f(E_s - E^{0\prime})} \qquad 4.5.2$$

where k^0 is the standard heterogeneous rate of electron transfer, α is the transfer coefficient, and $f = 38.94\ V^{-1}$ at 298 K. Plotting the natural logarithm of k_{app} against x yields a line of slope β and a y-intercept of $k_f(E)$ where $k_f(E)$ represents the

potential-dependent forward rate constant. If evaluated at different substrate potentials, this intercept should show a dependence on $E_s - E^{0\prime}$, and k^0 can be determined by extrapolation. Here we assume that the thickness of the OPD film has a linear dependence on the number of oxidative electropolymerization cycles.

In the second proposed mechanism, the polymer film is permeable.[41–44] Provided that the film is electrochemically inactive and uniform, mediator molecules must partition into the film to complete the redox reaction (Figure 4.5.8B). The apparent rate of electron transfer can then be described by

$$k_{app} = \frac{PD_{film}}{x} \qquad 4.5.3$$

where the P is the permeability constant, D_{film} is the diffusion coefficient of the mediator in the film, and x is the thickness of the film. In this case, the rate of electron transfer is inversely dependent on the thickness of the film, regardless of the potential of the substrate electrode.

Figures 4.5.8C and 4.5.8D show the plots corresponding to the two scenarios described for rate constants extracted from approach curves obtained at different substrate potentials and different numbers of OPD polymerization cycles. An example of the determination of the rate constants is shown in Figure 4.5.9 and Table 4.5.1. A well-correlated linear response was obtained when assuming the electron tunneling mechanism through the blocking layer at a number of oxidative polymerization cycles larger than 10. For less than 10 cycles of OPD polymerization, less than a monolayer is formed. The extrapolated value of k^0 in this case is 2×10^{-3} cm/s. The strong

potential dependence on the measured rates excludes the permeation mechanism, indicating that the tunneling model is more plausible and that the OPD film is insulating. Assuming a β value of 0.6 $Å^{-1}$ for π-conjugated systems, the growth rate of the film on grapheme can be extrapolated from the slope to be 20 Å for every 10 cycles.

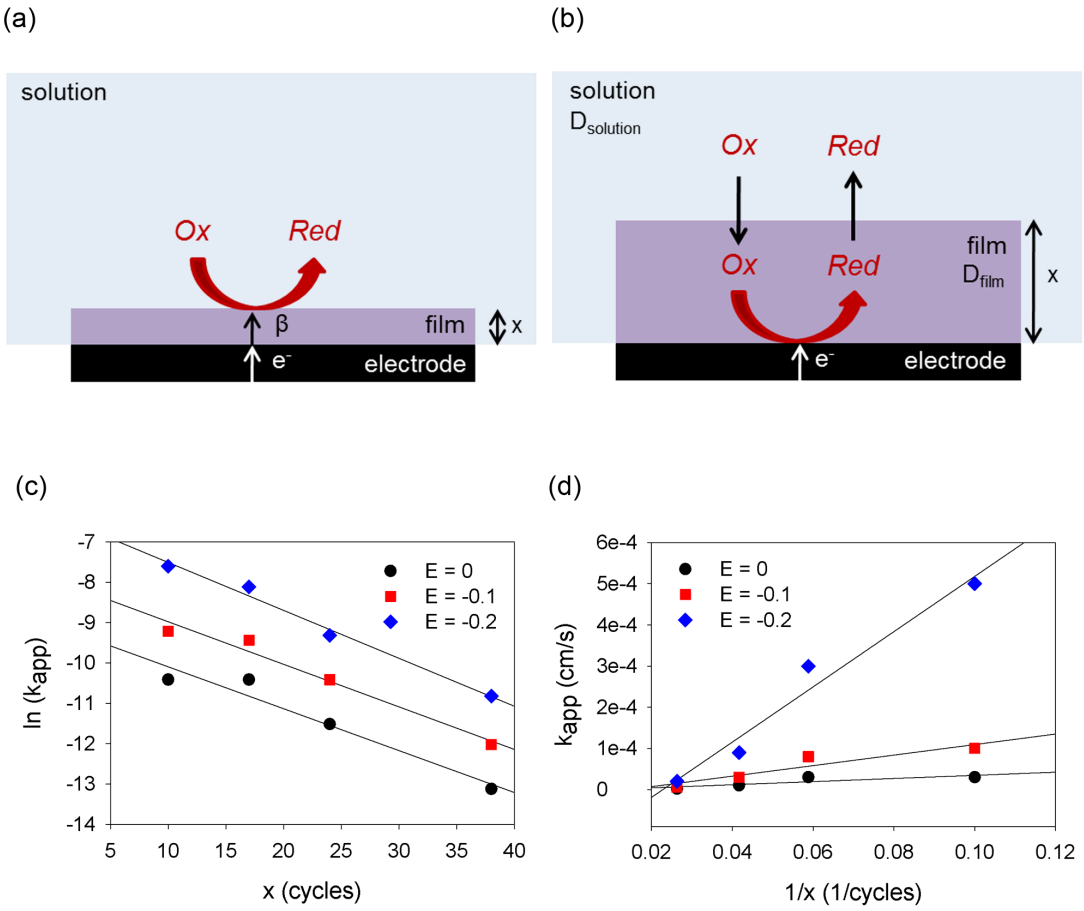

Figure 4.5.8. Determination of the properties of the OPD film on graphene. (A) Schematic of electron tunneling through an insulating film. (B) Schematic of electron transfer through a permeable film. (C) Plot of $\ln(k_f)$ *vs.* x following the tunneling model. (D) Plot of k_f *vs.* $1/x$ following the permeation model. The unit of k_{app} is cm/s.

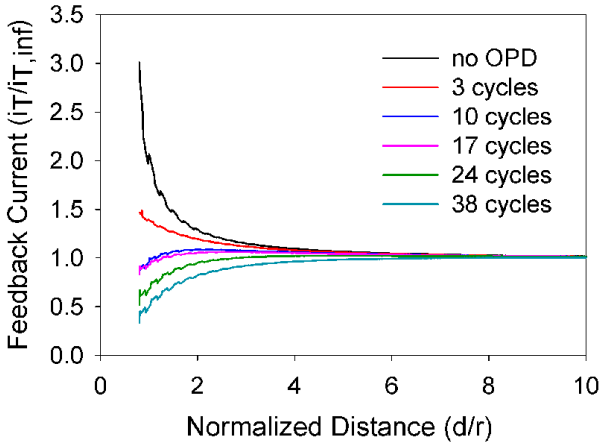

Figure 4.5.9. Determination of the forward rate of heterogeneous electron transfer, k_f. Approach curves above were fitted to theoretical curves to determine k_f after a different number of potential sweep cycles of OPD electropolymerization. SECM tip: Pt radius = 7.5 µm biased at 0.5 V *vs*. Ag/AgCl; graphene electrode: biased at 0 V *vs*. Ag/AgCl. Mediator: 1 mM FcMeOH; electrolyte: 0.1 M KCl. The same was done for graphene electrode biased at 0.1 V and 0.2 V *vs*. Ag/AgCl. The noise came from the movement of the z-piezo motor.

Number of Cycles	k_f(cm/s)
no OPD	$> 3\times10^{-3}$
3 cycles	3×10^{-4}
10 cycles	3×10^{-5}
17 cycles	3×10^{-5}
24 cycles	1×10^{-5}
38 cycles	2×10^{-6}

Table 4.5.1. Determination of the forward rate of heterogeneous electron transfer, k_f. Approach curves above were fitted to theoretical curves to determine k_f after a different number of potential sweep cycles of OPD electropolymerization.

4.6 Conclusions

We have examined the spatially resolved electrochemical activity of monolayer CVD graphene imperfections using SECM. $K_3Fe(CN)_6$ was our mediator of choice because it provides good contrast of the electrochemical activity of the defect sites *versus* pristine graphene. The variations in feedback current indicate that the defect sites have very different electron transfer kinetics compared to the overall graphene surface as predicted by computational studies and STM.[2,14–16] By carefully controlling the concentration and the number of oxidative cycles in the electropolymerization of OPD, we selectively passivated the activity of graphene defects. The slight decrease in overall electrochemical activity is believed to be the passivation of inherent defect sites. With further electropolymerization, an insulating thin film of OPD was formed, covering the bulk graphene electrode. We are currently working to improve the spatial resolution of our SECM by fabricating nano-sized probe electrodes to examine the defects inherent to the growth and fabrication of graphene.

4.7 References

1. Banhart, F.; Kotakoski, J.; Krasheninnikov, A. V. Structural Defects in Graphene. *ACS Nano* **2011**, *5*, 26–41.
2. Ugeda, M. M.; Brihuega, I.; Guinea, F.; Gómez-Rodríguez, J. M. Missing Atom as a Source of Carbon Magnetism. *Phys. Rev. Lett.* **2010**, *104*.
3. Boukhvalov, D. W.; Katsnelson, M. I. Chemical Functionalization of Graphene with Defects. *Nano Lett.* **2008**, *8*, 4373–4379.
4. Cantele, G.; Lee, Y.-S.; Ninno, D.; Marzari, N. Spin Channels in Functionalized Graphene Nanoribbons. *Nano Lett.* **2009**, *9*, 3425–3429.
5. Rice, R. J.; McCreery, R. L. Quantitative Relationship Between Electron Transfer Rate and Surface Microstructure of Laser-modified Graphite Electrodes. *Anal. Chem.* **1989**, *61*, 1637–1641.
6. Rice, R. J.; Pontikos, N. M.; McCreery, R. L. Quantitative Correlations of Heterogeneous Electron-transfer Kinetics with Surface Properties of Glassy Carbon Electrodes. *J. Am. Chem. Soc.* **1990**, *112*, 4617–4622.
7. Robinson, R. S.; Sternitzke, K.; McDermott, M. T.; McCreery, R. L. Morphology and Electrochemical Effects of Defects on Highly Oriented Pyrolytic Graphite. *J. Electrochem. Soc.* **1991**, *138*, 2412–2418.
8. McDermott, C. A.; Kneten, K. R.; McCreery, R. L. Electron Transfer Kinetics of Aquated $Fe^{+3/+2}$, $Eu^{+3/+2}$, and $V^{+3/+2}$ at Carbon Electrodes Inner Sphere Catalysis by Surface Oxides. *J. Electrochem. Soc.* **1993**, *140*, 2593–2599.

9. Kneten, K.; McCreery, R. L. Effects of Redox System Structure on Electron-Transfer Kinetics at Ordered Graphite and Glassy Carbon Electrodes. *Anal. Chem.* **1992**, *64*, 2518–2524.
10. McDermott, M. T.; Kneten, K.; McCreery, R. L. Anthraquinonedisulfonate Adsorption, Electron-transfer Kinetics, and Capacitance on Ordered Graphite Electrodes: The Important Role of Surface Defects. *J. Phys. Chem.* **1992**, *96*, 3124–3130.
11. Cline, K. K.; McDermott, M. T.; McCreery, R. L. Anomalously Slow Electron Transfer at Ordered Graphite Electrodes: Influence of Electronic Factors and Reactive Sites. *J. Phys. Chem.* **1994**, *98*, 5314–5319.
12. McCreery, R. L. Advanced Carbon Electrode Materials for Molecular Electrochemistry. *Chem. Rev.* **2008**, *108*, 2646–2687.
13. Wildgoose, G. G.; Abiman, P.; Compton, R. G. Characterising Chemical Functionality on Carbon Surfaces. *J. Mat. Chem.* **2009**, *19*, 4875.
14. Sanyal, B.; Eriksson, O.; Jansson, U.; Grennberg, H. Molecular Adsorption in Graphene with Divacancy Defects. *Phys. Rev. B* **2009**, *79*.
15. Tachikawa, H.; Kawabata, H. Electronic States of Defect Sites of Graphene Model Compounds: A DFT and Direct Molecular Orbital-Molecular Dynamics Study. *J. Phys. Chem. C* **2009**, *113*, 7603–7609.
16. Hu, B.; Hwang, E.; Sarma, S. Das Density of States of Disordered Graphene. *Phys. Rev. B* **2008**, *78*.

17. Ghaderi, N.; Peressi, M. First-Principle Study of Hydroxyl Functional Groups on Pristine, Defected Graphene, and Graphene Epoxide. *J. Phys. Chem. C* **2010**, *114*, 21625–21630.
18. Lim, C. X.; Hoh, H. Y.; Ang, P. K.; Loh, K. P. Direct Voltammetric Detection of DNA and pH Sensing on Epitaxial Graphene: An Insight into the Role of Oxygenated Defects. *Anal. Chem.* **2010**, *82*, 7387–7393.
19. Qu, L.; Liu, Y.; Baek, J.-B.; Dai, L. Nitrogen-Doped Graphene as Efficient Metal-Free Electrocatalyst for Oxygen Reduction in Fuel Cells. *ACS Nano* **2010**, *4*, 1321–1326.
20. Brownson, D. A. C.; Banks, C. E. CVD Graphene Electrochemistry: The Role of Graphitic Islands. *Phys. Chem. Chem. Phys.* **2011**, *13*, 15825.
21. Wipf, D. O.; Bard, A. J. Scanning Electrochemical Microscopy VII. Effect of Heterogeneous Electron-Transfer Rate at the Substrate on the Tip Feedback Current. *J. Electrochem. Soc.* **1991**, *138*, 469–474.
22. Bard, A. J.; Mirkin, M. V. *Scanning Electrochemical Microscopy*; Marcel Dekker: New York, 2001.
23. Bard, A. J.; Fan, F.-R. F.; Mirkin, M. V. *Electroanalytical Chemistry: Scanning Electrochemical Microscopy*; Marcel Dekker: New York; Vol. 18.
24. Bard, A. J.; Denuault, G.; Lee, C.; Mandler, D.; Wipf, D. O. Scanning Electrochemical Microscopy-a New Technique for the Characterization and Modification of Surfaces. *Acc. Chem. Res.* **1990**, *23*, 357–363.

25. Dumitrescu, I.; Dudin, P. V.; Edgeworth, J. P.; Macpherson, J. V.; Unwin, P. R. Electron Transfer Kinetics at Single-Walled Carbon Nanotube Electrodes Using Scanning Electrochemical Microscopy. *J. Phys. Chem. C* **2010**, *114*, 2633–2639.
26. Edwards, M. A.; Bertoncello, P.; Unwin, P. R. Slow Diffusion Reveals the Intrinsic Electrochemical Activity of Basal Plane Highly Oriented Pyrolytic Graphite Electrodes. *J. Phys. Chem. C* **2009**, *113*, 9218–9223.
27. Xie, X.; Zhao, K.; Xu, X.; Zhao, W.; Liu, S.; Zhu, Z.; Li, M.; Shi, Z.; Shao, Y. Study of Heterogeneous Electron Transfer on the Graphene/Self-Assembled Monolayer Modified Gold Electrode by Electrochemical Approaches. *J. Phys. Chem. C* **2010**, *114*, 14243–14250.
28. White, H. S.; Abruna, H. D.; Bard, A. J. Improvement of Performance of n-WSe2 Electrodes by Electrochemial Polymerization of o-Phenylenediamine at Surface Imperfections. *J. Electrochem. Soc.* **1982**, *129*, 265–271.
29. Losito, I.; Palmisano, F.; Zambonin, P. G. *o*-Phenylenediamine Electropolymerization by Cyclic Voltammetry Combined with Electrospray Ionization-Ion Trap Mass Spectrometry. *Anal. Chem.* **2003**, *75*, 4988–4995.
30. Huang, P. Y.; Ruiz-Vargas, C. S.; Zande, A. M. van der; Whitney, W. S.; Levendorf, M. P.; Kevek, J. W.; Garg, S.; Alden, J. S.; Hustedt, C. J.; Zhu, Y. *et al.* Grains and Grain Boundaries in Single-layer Graphene Atomic Patchwork Quilts. *Nature* **2011**, *469*, 389–392.
31. Lefrou, C.; Cornut, R. Analytical Expressions for Quantitative Scanning Electrochemical Microscopy (SECM). *Chem. Phys. Chem.* **2010**, *11*, 547–556.

32. Bard, A. J.; Mirkin, M. V.; Unwin, P. R.; Wipf, D. O. Scanning Electrochemical Microscopy. 12. Theory and Experiment of the Feedback Mode with Finite Heterogeneous Electron-transfer Kinetics and Arbitrary Substrate Size. *J. Phys. Chem.* **1992**, *96*, 1861–1868.

33. Li, W.; Tan, C.; Lowe, M. A.; Abruña, H. D.; Ralph, D. C. Electrochemistry of Individual Monolayer Graphene Sheets. *ACS Nano* **2011**, *5*, 2264–2270.

34. Pimenta, M. A.; Dresselhaus, G.; Dresselhaus, M. S.; Can?ado, L. G.; Jorio, A.; Saito, R. Studying Disorder in Graphite-based Systems by Raman Spectroscopy. *Phys. Chem. Chem. Phys.* **2007**, *9*, 1276.

35. Liu, H.; Ryu, S.; Chen, Z.; Steigerwald, M. L.; Nuckolls, C.; Brus, L. E. Photochemical Reactivity of Graphene. *J. Am. Chem. Soc.* **2009**, *131*, 17099–17101.

36. Lowry, J. P.; McAteer, K.; El Atrash, S. S.; Duff, A.; O'Neill, R. D. Characterization of Glucose Oxidase-modified Poly (phenylenediamine)-coated Electrodes in Vitro and in Vivo: Homogeneous Interference by Ascorbic Acid in Hydrogen Peroxide Detection. *Anal. Chem.* **1994**, *66*, 1754–1761.

37. Losito, I.; Giglio, E. De; Cioffi, N.; Malitesta, C. Spectroscopic Investigation on Polymer Films Obtained by Oxidation of O-phenylenediamine on Platinum Electrodes at Different pHs. *J. Mat. Chem.* **2001**, *11*, 1812–1817.

38. Liu, B.; Bard, A. J.; Mirkin, M. V.; Creager, S. E. Electron Transfer at Self-Assembled Monolayers Measured by Scanning Electrochemical Microscopy. *J. Am. Chem. Soc.* **2004**, *126*, 1485–1492.

39. Kiani, A.; Alpuche-Aviles, M. A.; Eggers, P. K.; Jones, M.; Gooding, J. J.; Paddon-Row, M. N.; Bard, A. J. Scanning Electrochemical Microscopy. 59. Effect of Defects and Structure on Electron Transfer Through Self-Assembled Monolayers. *Langmuir* **2008**, *24*, 2841–2849.

40. Bard, A. J.; Faulkner, L. R. *Electrochemical Methods*; 2nd ed.; John Wiley & Sons: Hoboken, NJ, 2000.

41. Williams, M. E.; Benkstein, K. D.; Abel, C.; Dinolfo, P. H.; Hupp, J. T. Shape-selective Transport Through Rectangle-based Molecular Materials: Thin-film Scanning Electrochemical Microscopy Studies. *PNAS* **2002**, *99*, 5171–5177.

42. Williams, M. E.; Hupp, J. T. Scanning Electrochemical Microscopy Assessment of Rates of Molecular Transport Through Mesoporous Thin-Films of Porphyrinic "Molecular Squares". *J. Phys. Chem. B* **2001**, *105*, 8944–8950.

43. Williams, M. E.; Stevenson, K. J.; Massari, A. M.; Hupp, J. T. Imaging Size-Selective Permeation Through Micropatterned Thin Films Using Scanning Electrochemical Microscopy. *Anal. Chem.* **2000**, *72*, 3122–3128.

44. Cornut, R.; Lefrou, C. Studying Permeable Films with Scanning Electrochemical Microscopy (SECM): Quantitative Dtermination of Permeability Parameter. *J. of Electroanal. Chem. and Interf. Electrochem.* **2008**, *623*, 197–203.

Chapter 5

Outlook

The development of individual single-layer graphene electrodes has allowed us to design novel experiments where graphene's structure and electrochemical activity play critical roles. Graphene can be used for numerous applications as described in Chapter 1. In addition, graphene can serve as a platform for molecular assembly, and consequently opens up a wide range of opportunities in both academic research and industrial applications.

5.1 Diffusion of Tripodal Molecules on Graphene Studied using Scanning Electrochemical Microscopy

Graphene, a very unique surface, can serve as a platform for electrochemical experiments such as the investigation of the diffusion of adsorbed molecules. Scanning electrochemical microscopy was used to detect the activity and quantify the surface diffusion of a cobalt bis-terpyridine tripodal compound adsorbed onto single-layer graphene and the basal plane of HOPG using two complementary methods (Figure 5.1.1).[1] The first method used the substrate generation/tip collection (G/C) mode of SECM to exploit the electrocatalytic properties of the adsorbed tripod, which produced larger amounts of H_2O_2 than the bare graphene surface in the oxygen reduction reaction. A second method used the feedback mode, in which the tripod mediated the oxidation of ferrocyanide produced at the tip faster than the bare

graphene electrode. For each measurement, the increased electrochemical activity of the adsorbed molecules relative to the single-layer graphene electrode provided sufficient contrast to image microspots of the tripodal molecules with spatial resolution. We attribute the decreased electrochemical response of the tripodal microspots over time to diffusion of the molecules onto the unfunctionalized regions of the single-layer graphene electrode. The two imaging strategies yielded similar values of the macroscopic surface diffusion of the tripod on the graphene surface: D_{eff} $=1.6\times10^{-9}$ cm^2/s and D_{eff} $=1.5\times10^{-9}$ cm^2/s for G/C and feedback modes, respectively.

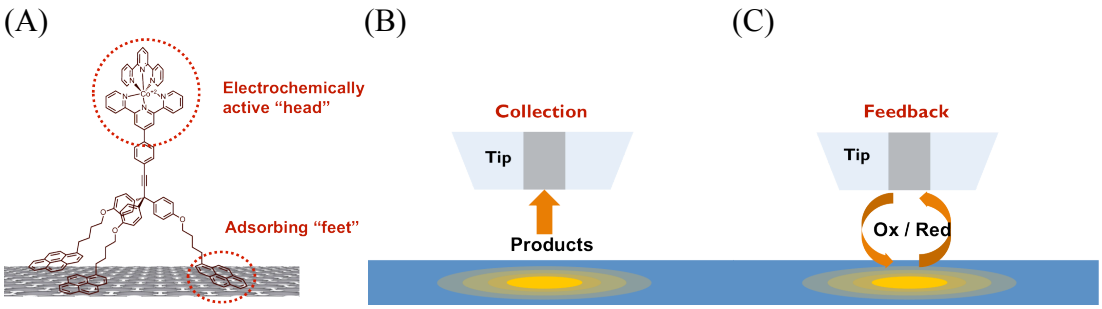

Figure 5.1.1. (A) Cobalt bis-terpyridine tripod adsorbed onto single-layer graphene electrode. The diffusion of the tripodal molecule is investigated using the (B) generation-collection and (C) feedback modes of SECM.

The spatially resolved feedback current is dependent on the localized surface concentration of the adsorbed molecule and we are interested in studying the impact of defects on the graphene surface on the mobility of the tripodal molecules. Furthermore, studying the effects of electrode potential on the mobility of adsorbed species on graphene electrodes could be a great leap forward in the understanding of

surface mediated dynamics. The development of graphene electrode in combination with SECM offers the capability to examine these dynamic processes.[2–4]

5.2 Electropolymerization on Graphene

Electropolymerization is a widely used deposition method, which offers many advantages over other polymerization or surface modification methods. Electropolymerization of an electrochemically inactive molecule, *o*-phenylenediamine, was discussed in Chapter 4. Moreover, we have explored the electropolymerization of 3,4-ethylenedioxythiophene and 3,4-dihydroxybenzaldehyde on CVD graphene.

Poly(3,4-ethylenedioxythiophene) (PEDOT) and its derivatives have been of enormous interest in applications such as batteries, electronic displays, and photovoltaic devices.[5–9] They are also effective candidates for electrochromic applications because of their stability, chemical diversity, and high contrast ratio.[10] PEDOT is transparent in the oxidized state and dark blue in the neutral state (Figure 5.2.1). Many different colors can be achieved by PEDOT derivatives as reported by many research groups. A thin film of PEDOT was deposited onto a CVD graphene electrode via electropolymerization of the monomer unit, 3,4-ethylenedioxythiophene (EDOT). Preliminary results indicate that EDOT can be anodically electropolymerized onto graphene electrodes. An increase in double layer capacitance and a decrease in oxidative potential with the number of oxidative cycles were observed (Figure 5.2.2A). The increase in capacitance is due to the increase in PEDOT deposited on the

graphene surface, and the decrease in anodic peak potential is a result of an increase in the length of the conjugated polymer chain. The electrode was examined in a fresh electrolyte solution. A color change from dark blue to clear was observed as the potential is scanned cathodically (negative) as illustrated in Figure 5.2.2B.

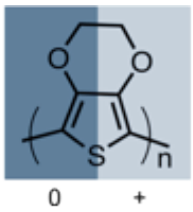

Figure 5.2.1. PEDOT and its derivatives exhibit electrochromic properties. PEDOT is transparent in the oxidized state and dark blue in the neutral state.

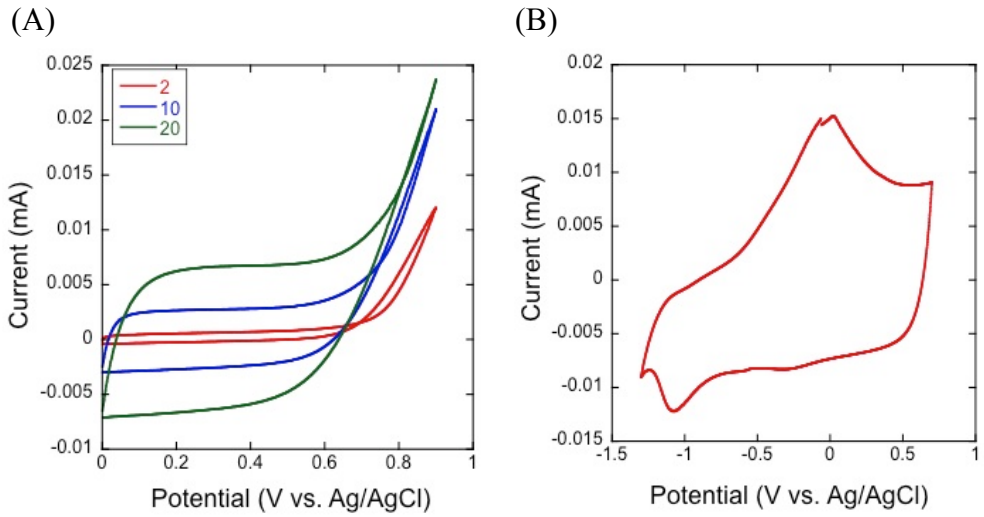

Figure 5.2.2. Electropolymerization of PEDOT on CVD graphene electrode.

The electropolymerization of 3,4-dihydroxybenzaldehyde (DHB) is also of vast interest in biochemistry because its ability to catalyze NADH oxidation

reactions.[11] Cyclic voltammogram suggests that DHB can be anodically electropolymerized on graphene electrodes (Figure 5.2.3). Cyclic voltammetry experiments at various sweep rates showed that the redox active DHB is immobilized onto the graphene electrode. In addition, due to the nature of the redox active functional group, the redox potential is linearly dependent on the pH of the electrolyte solution as illustrated in Figure 5.2.4. The relationship can be described by

$$E = E^{0\prime} + 0.059pH \qquad 5.2.1$$

The experimental data yielded a slope of 0.058 which is in agreement with Equation 5.2.1. The immobolized DHB acts as a catalyst in the oxidation of NADH as shown in Figure 5.2.5. The oxidation potential on bare graphene electrode is 0.47 V *vs*. Ag/AgCl and that on DHB modified graphene electrode is 0.23 V *vs*. Ag/AgCl.

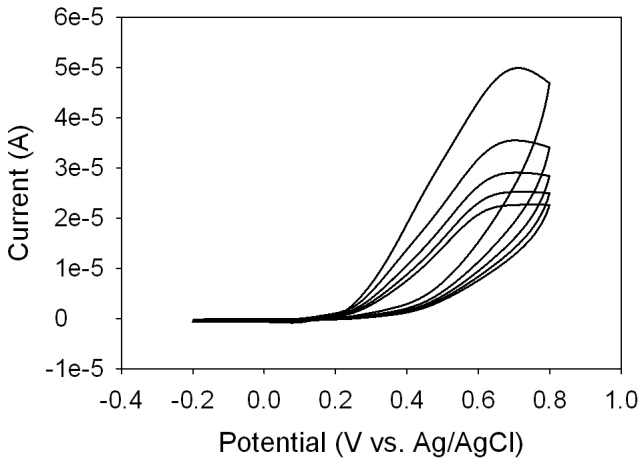

Figure 5.2.3. Electropolymerization of 3,4-dihydroxybenzaldehyde on CVD graphene electrode.

(A)

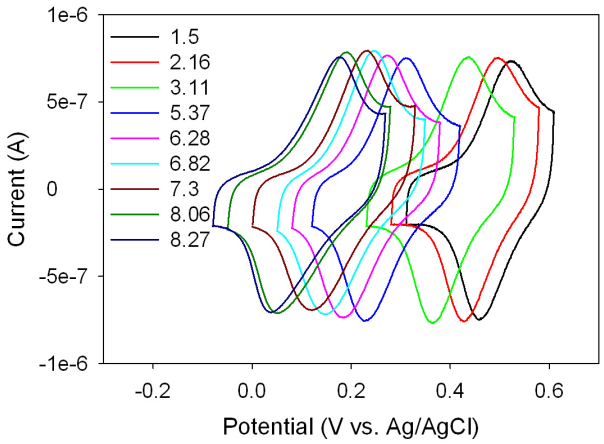

(B)

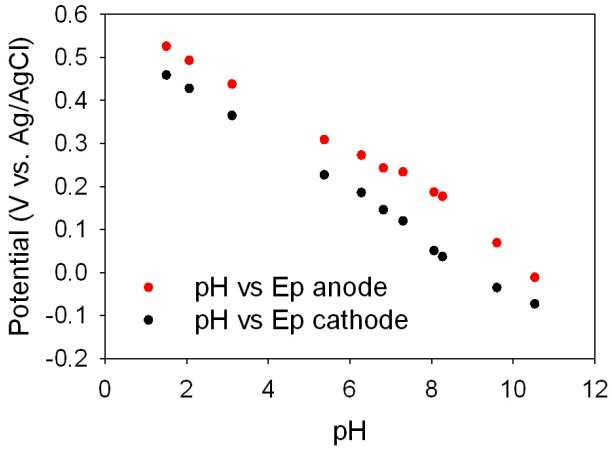

Figure 5.2.4. (A) The anodic (oxidative) peak and the cathodic (reductive) peak potentials is linearly related to the pH of the solution. (B) A slope of 58 was determined from both anodic and cathodic peak potentials.

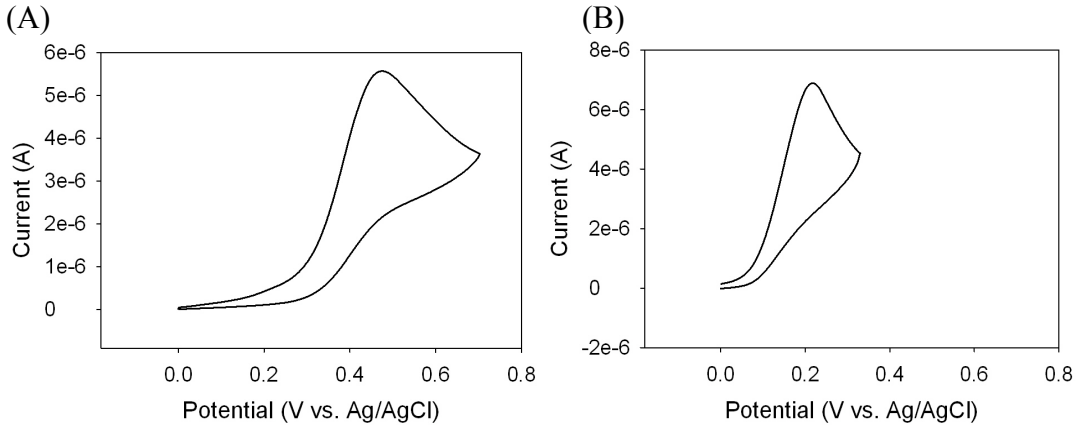

Figure 5.2.5. Oxidation of NADH on graphene electrode and DHB modified graphene electrode. The oxidation potential on (A) bare graphene electrode is 0.47 V *vs*. Ag/AgCl and that on (B) DHB modified graphene electrode is 0.23 V *vs*. Ag/AgCl. A solution of 0.5 mM NADH in pH 7.5 phosphate buffer is used for both experiments.

5.3 Investigating Graphene's Intrinsic Properties: Grain Size *versus* Reactivity

We anticipate obtaining information about the impact of structural features in graphene, for example, grain boundaries and defects, on reactivity by means of SECM imaging. The use of SECM probes with radii between 0.1 and 1 mm and selective redox mediators could help us identify different domains in graphene samples and identify their reactivity differences. The grain size can be determined by transmission electron microscopy.[12] The various colors correspond to the different grain orientations on the graphene sample – each grain orientation gives rise to an electron diffraction spot in the diffraction image. A selective aperture is applied to capture regions of a particular grain orientation on the graphene sample. The various grain orientations can be overlaid into a single image to give Figure 5.3.1. Because of the

rapid development and advancement in graphene preparation methods over the past 4 years, it is possible to achieve large grain size graphene up to a few millimeters. It is of our interest to be able to correlate TEM images of grain size and SECM images of reactivity.

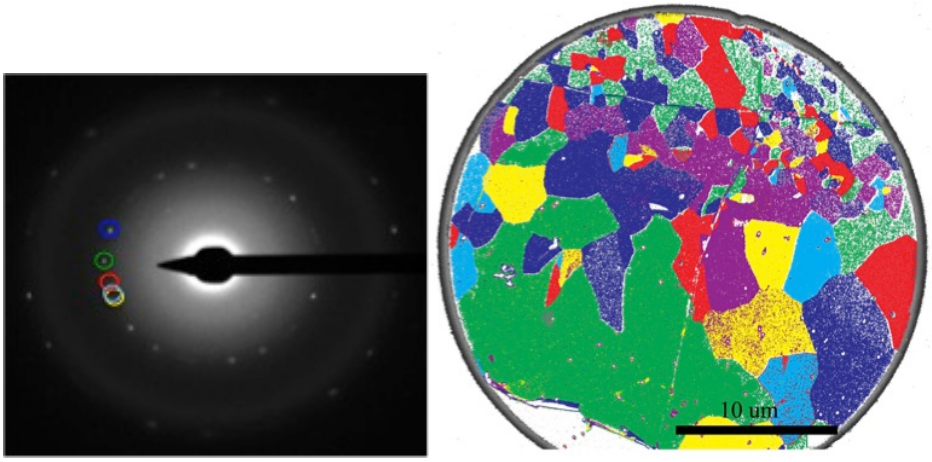

Figure 5.3.1. TEM image of CVD graphene. Each grain orientation gives rise to an electron diffraction spot in the diffraction image. A selective aperture is applied to capture regions of a particular grain orientation on the graphene sample.

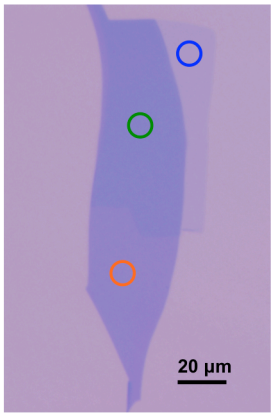

Figure 5.3.2. Optical micrograph of single-, few- and multi-layer mechanically exfoliated graphene on SiO_2/Si.

We are also interested in investigating the intrinsic properties of mechanically exfoliated graphene of various thicknesses. SECM allows us to examine the rate of heterogeneous electron transfer at the location of choice. It could possibly eliminate a lot of artifacts from contact resistance to trapped redox mediator molecules between graphene and the Al_2O_3 protective layer in cyclic voltammetry measurements.

5.4 Outlook

Graphene is indeed a unique material. Its fascinating properties have allowed it to be employed in many applications. At the same time, many other two-dimensional or pseudo two-dimension materials with distinctive properties have emerged. Molybdenum disulfide and *h*-boron nitride, for example, are semi-conducting and insulating, respectively. In addition, the basal planes and edges of molybdenum disulfide exhibit very different reactivity. *h*-Boron nitride, although an insulator, could be used to probe the reactivity of graphene. Strano and co-workers have demonstrated that the reactivity of graphene is substrate dependent.[13] *h*-Boron nitride and alkyl modified silicon substrates hinder the chemical reactivity of graphene, while SiO_2 and Al_2O_3 promote it. The differences are ascribed to the amplitudes of substrate-induced electron-hole charge fluctuations. Graphene, molybdenum disulfide and *h*-boron nitride provide a lot of prospects to the world of two-dimensional materials. There is much demand for continuing the investigation of the physical, electrical and chemical properties for further improvements and advancements.

5.5 References

1. Rodríguez-López, J.; Ritzert, N. L.; Mann, J. A.; Tan, C.; Dichtel, W. R.; Abruña, H. D. Quantification of the Surface Diffusion of Tripodal Binding Motifs on Graphene Using Scanning Electrochemical Microscopy. *J. Am. Chem. Soc.* **2012**, *134*, 6224–6236.
2. Li, W.; Tan, C.; Lowe, M. A.; Abruña, H. D.; Ralph, D. C. Electrochemistry of Individual Monolayer Graphene Sheets. *ACS Nano* **2011**, *5*, 2264–2270.
3. Tan, C.; Rodríguez-López, J.; Parks, J. J.; Ritzert, N. L.; Ralph, D. C.; Abruña, H. D. Reactivity of Monolayer Chemical Vapor Deposited Graphene Imperfections Studied Using Scanning Electrochemical Microscopy. *ACS Nano* **2012**, *6*, 3070–3079.
4. Bard, A. J.; Mirkin, M. V. *Scanning Electrochemical Microscopy*; Marcel Dekker: New York, 2001.
5. Kiya, Y.; Henderson, J. C.; Abruña, H. D. 4-Amino-4H-1,2,4-triazole-3,5-dithiol. *J. Electrochem. Soc.* **2007**, *154*, A844.
6. Armstrong, N. R.; Wang, W.; Alloway, D. M.; Placencia, D.; Ratcliff, E.; Brumbach, M. Organic/Organic′ Heterojunctions: Organic Light Emitting Diodes and Organic Photovoltaic Devices. *Macromol. Rapid Commun.* **2009**, *30*, 717–731.
7. Søndergaard, R.; Hösel, M.; Angmo, D.; Larsen-Olsen, T. T.; Krebs, F. C. Roll-to-roll Fabrication of Polymer Solar Cells. *Materials Today* **2012**, *15*, 36–49.

8. Kirchmeyer, S.; Reuter, K. Scientific Importance, Properties and Growing Applications of Poly(3,4-ethylenedioxythiophene). *J. Mater. Chem.* **2005**, *15*, 2077.
9. Groenendaal, L.; Jonas, F.; Freitag, D.; Pielartzik, H.; Reynolds, J. R. Poly(3,4-ethylenedioxythiophene) and Its Derivatives: Past, Present, and Future. *Adv. Mater.* **2000**, *12*, 481–494.
10. Argun, A. A.; Aubert, P.-H.; Thompson, B. C.; Schwendeman, I.; Gaupp, C. L.; Hwang, J.; Pinto, N. J.; Tanner, D. B.; MacDiarmid, A. G.; Reynolds, J. R. Multicolored Electrochromism in Polymers: Structures and Devices. *Chem. Mat.* **2004**, *16*, 4401–4412.
11. Pariente, F.; Tobalina, F.; Moreno, G.; Hernandez, L.; Lorenzo, E.; Abruna, H. D. Mechanistic Studies of the Electrocatalytic Oxidation of NADH and Ascorbate at Glassy Carbon Electrodes Modified with Electrodeposited Films Derived from 3, 4-dihydroxybenzaldehyde. *Anal. Chem.* **1997**, *69*, 4065–4075.
12. Huang, P. Y.; Ruiz-Vargas, C. S.; Zande, A. M. van der; Whitney, W. S.; Levendorf, M. P.; Kevek, J. W.; Garg, S.; Alden, J. S.; Hustedt, C. J.; Zhu, Y. *et al.* Grains and Grain Boundaries in Single-layer Graphene Atomic Patchwork Quilts. *Nature* **2011**, *469*, 389–392.
13. Wang, Q. H.; Jin, Z.; Kim, K. K.; Hilmer, A. J.; Paulus, G. L. C.; Shih, C.-J.; Ham, M.-H.; Sanchez-Yamagishi, J. D.; Watanabe, K.; Taniguchi, T. *et al.* Understanding and Controlling the Substrate Effect on Graphene Electron-transfer Chemistry via Reactivity Imprint Lithography. *Nat. Chem.* **2012**, *4*, 724–732.